Decelerating Dust Grains Using Pulsed Plasma Thrusters

Wesley Jackson

A thesis
submitted in partial fulfillment of the
requirements for the degree of

Master of Science in Aeronautics and Astronautics

University of Washington

2021

Committee:

Justin Little, Chair

Uri Shumlak

Program Authorized to Offer Degree:
Aeronautics and Astronautics

University of Washington

Abstract

Decelerating Dust Grains Using Pulsed Plasma Thrusters

Wesley Jackson

Chair of the Supervisory Committee:
Assistant Professor Justin Little
Aeronautics and Astronautics

This thesis seeks to examine the feasibility of a system that uses Pulsed Plasma Thrusters (PPTs) to slow down hypervelocity, micron-size ice grains in order to preserve potential organic material contained within. The motivation for this research comes from a NASA call for technologies that enable novel mission profiles to capture grains from flybys of icy ocean worlds like Enceladus and Europa. A mathematical model for analyzing the plasma drag on a dust grain is developed using Sheath Limited and Orbital Motion Limited theories of dusty plasma physics. This model is then used to create time- and length-dependent plots along with contour plots dependent on grain radius and velocity. These plots are used to develop the plasma parameters necessary for adequately decelerating incoming ice grains. A first order approximation of the system feasibility is conducted by analyzing collected mass, energy per pulse, and rate of incoming grains and comparing this to other PPTs and collection mechanisms. The proposed system is technically achievable with an energy per pulse of 11.9 J, and may even increase the organic capture efficiency for missions that have to operate at flyby velocities above 3 km/s. However, matching the 14 kHz frequency of impinging particles during high plume activity is not practical, and tradeoffs must be made in the number of grains the plasma interacts with and the sensible power requirements of the system. Ultimately, this idea may be useful for higher velocity missions, but more work is needed to determine best use cases and develop such a system.

TABLE OF CONTENTS

LIST OF FIGURES

LIST OF TABLES

ACKNOWLEDGMENTS

I would like to thank the University of Washington and the US Department of the Air Force for enabling my desire to further my education and obtain my Master's Degree. I look forward to applying myself in the Space Force and the world at large.

I would also like to thank Professor Justin Little for his contributions to this work and my development at grad school. This thesis would not be what it is today without his assistance over the past couple of years.

I would also like to my parents, friends, and lab mates for supporting me along the way. I have lost track of how many times these people have put up with my complaints and put me back on course throughout my time at UW and especially during the struggles associated with the COVID-19 lockdowns and isolation. My life has been better because of all of you.

Finally, I would like to thank God for sending His Son and for being my source of peace and wisdom in all times.

DEDICATION

to our glorious leader, Goose

Proverbs 2:6

Chapter 1

INTRODUCTION

At the present moment, humanity's exploration of the solar system has revealed that water – a necessary element to life as we know it – is much more abundant throughout our planetary neighborhood than previously believed. It is found as ice on many of the numerous moons of the outer planets and can even be found under the deserts of Mars or at the far reaches of Pluto. Liquid water as it exists on Earth is much harder to come by, though mounting evidence suggests that it may be found underneath the icy surface of some of the Galilean moons, and Cassini has shown us that Enceladus has enough to produce frosty geyser plumes.

In the search for extraterrestrial life, the first step has always been "find the water", and now that we have, it is time to investigate these sources further. Recently, the National Aeronautics and Space Administration (NASA) has posted a call for technologies that will enable the collection and analysis of the water ice ejected from geysers in support of the Ocean Worlds Exploration Program [1]. Of particular interest are systems "capable of high-velocity sample collection with minimal sample alteration" that can withstand all the rigors associated with an interplanetary mission [1].

Considering that plasma propulsion devices are already made to withstand the hazards of space, it may be interesting to investigate if a plasma exhaust could be used to slow down incoming ice grains to a safe capture velocity for a high-speed flyby of a geyser plume. That is the question that this thesis seeks to answer.

In the following pages, we will develop a mathematical model to investigate the physics of plasma drag on small ice grains. This model will then be used to produce a number of outputs that will enable us to intelligently manipulate key plasma parameters in order to

slow grain impact velocity while minimizing ablation. Finally, we will analyze the results of this design to determine its feasibility and compare it to other proposed systems. We conclude by discussing the future work that would be needed to answer additional questions raised by this thesis and by explaining the possible use cases for such a system. Ultimately, this study finds that the proposed system is feasible within certain restrictions and may have uses for missions requiring flyby velocities greater than 3 km/s.

1.1 Icy Ocean Worlds

Likely the largest volume of water in the solar system outside Earth's oceans can be found on Europa. Though some other Galilean moons of Jupiter are also quite icy, Europa's relatively uncratered surface and unique features indicate that some sort of hydrological process is renewing the moon's outer crust. Ever since Cassini found evidence for icy geysers at Enceladus, scientists have searched for similar signs at Europa. Using data from the Hubble Space Telescope, some groups have observed evidence for water vapor plumes emanating from different surface locations at various points in Europa's orbit [42] [47], though some of these findings might not be statistically significant [15]. More recently, an investigation using the Keck Observatory found that Europa's geyser activity may be rare but powerful [35], and reanalysis of data from the Galileo mission revealed that spacecraft might have encountered a plume during a Europa flyby [20]. Ultimately, little of this work is definitive, and we will have to wait on the European Space Agency's Jupiter Icy Moons Explorer and NASA's Europa Clipper mission to get more direct information.

Thanks to Cassini, we know much more about the geyser plumes at Enceladus than we do about those from Europa. For that reason, this thesis primarily focuses its discussion around collecting material from the plumes of Enceladus. However, the model created within is general enough that it can be adapted to analyze a mission to Europa as new information about the structure of its plumes becomes available.

At this point, it is well known that Enceladus has an icy crust and likely has some form of subsurface ocean that is heated geothermally due to tidal effects between the moon

and Saturn. Results of this heating have been observed extensively by numerous Cassini instruments in the water ice geysers emanating from features colloquially known as the tiger stripes near the south pole of Enceladus. Since geothermal heating on Earth produces underwater islands of life on the deep ocean floor that do not rely on photosynthesis, it is often speculated as to whether or not similar processes might have enabled life to survive at Enceladus.

Cassini was a general purpose mission to Saturn and was thus ill-equipped to directly study the possible signs of life emanating from the polar plumes. The Ion and Neutral Mass Spectrometer (INMS) was unable to detect molecules larger than its designed mass-to-charge ratio limit, and the Cosmic Dust Analyzer (CDA) only detected ice grains down to the size of approximately 1.7 μm, and was unable to do much further analysis outside elementary detection [37] [23]. Thus any vaporized organic molecules that might be present were unable to be detected, and any such molecules trapped in ice grains went unnoticed. However, INMS detection of volatile compounds and small hydrocarbons as well as CDA data that suggests small concentrations of complex organic cations, among other findings, lend credence to the idea that something more complex than simple heating might be going on underneath the ice [24] [38]. If we were able to design a system that efficiently captures the particles ejected from the subsurface ocean with minimal degradation, analysis processes developed by others [29] could then be used to meticulously and accurately search for and examine the organic molecules within the sample, furthering humanity's knowledge about life in our solar system.

One major issue faced by mission planners and payload designers is that little to no complex organic molecules will survive the hypervelocity impacts experienced when colliding with a detector traveling at typical Cassini-Enceladus flyby speeds [21] [7] [33] [34]. This can be mitigated with precise design of the spacecraft orbit, but such considerations often incur an increase in fuel, mass, and mission cost, thereby decreasing scientific payload [48]. This thesis will study the possibility of altering the speed of an incoming ice grain with a method independent from the spacecraft velocity. Such a device would allow mission planners greater flexibility when designing the next probe to Saturn or Jupiter to study these icy ocean worlds.

1.2 Dusty Plasma Drag and Pulsed Plasma Thrusters

In the early 2000s, groups at the Los Alamos National Laboratory were working on developing new methods for analyzing fusion plasma experiments [51] [52]. One of the methods considered involved injecting micron-sized graphite and diamond grains into the center of the plasma and observing them as they were dragged about by the plasma and ablated away. The grains would only survive a few milliseconds, but that would be enough. In developing this diagnostic system, they first came up with a model for the force of plasma drag on these microparticles [51], and then they built an experiment that used a coaxial plasma gun to test their model [52]. This device was also designed as a potential method for injecting these dust grains into a fusion plasma, but this is where we will leave these researchers.

One of the most widely used and thoroughly developed types of plasma propulsion is that of the humble Pulsed Plasma Thruster (PPT). This relatively simple device produces thrust by ionizing a bit of propellant and rapidly accelerating the resulting plasma in a method reminiscent of a rail gun. These devices typically use otherwise inert solid propellants and are thus small, light, simple, and relatively easy to incorporate into the design of even small satellites. Due to these traits, a wide variety of PPTs have been used on numerous spacecraft over the years, and their ability to work in the space environment is well understood.

When these two concepts – plasma dragged microparticles and PPTs – are combined, they reveal a possible solution to NASA's need for high velocity sample collection systems. Enough is known about the properties of Enceladus' plume and safe impact speeds for ice grains containing organic molecules that developing a model designed to emulate these collisions should be straightforward. By adapting the physics for plasma drag utilized by Los Alamos, we could simulate the effects an exhausting plasma sheet would have on incoming high velocity ice grains. Adjusting the parameters for such a plasma sheet would then reveal the ideal system to use in order to slow these ice grains to acceptable capture speeds. As long as these parameters are achievable with a PPT, it would be possible to effectively incorporate this plasma buffer system into a dust collector and thus give mission planners the option

of higher velocity passes over a target with minimal degradation in collected material. The remainder of this thesis seeks to develop these hypotheticals into concrete results so that we can determine the feasibility of such a system.

Chapter 2

THE PHYSICS OF PLASMA DRAG ON DUST PARTICLES

There has been decades of research into dusty plasma physics whose purpose has been to further our understanding of the complex, multi-species plasmas that exist primarily in the cosmos, but also in certain situations here on Earth. When it comes to the interaction of high speed flowing plasmas and micron-sized dust particles, two theories of dusty plasma physics are very useful for analyzing this phenomenon: Sheath Limited (SL) theory and Orbital Motion Limited (OML) theory. Each of these theories have been built up over many years of theoretical research, and each were validated experimentally over the past few decades [56] [39] [27] [2] [53] [17] [18].

2.1 Introduction of Physical Theories

Whether SL theory or OML theory is employed depends on how the size of the dust grain in question relates to the Debye length of the surrounding plasma. If the size of the grain is relatively large, then SL applies, but if it is relatively small, OML applies. In both cases, the dust grain itself is assumed to be spherical. For the situation investigated in this thesis, there are typical dust grain radii of $r_d \approx 0.1 - 5$ μm and plasma densities and temperatures of $n_p \approx 10^{22}$ m^{-3} and $T_p \approx 10$ eV, respectively. These indicate that we will usually have Debye lengths near $\lambda_D \approx 0.17$ μm and will thus primarily use SL theory. Since full ablation of the grains will push the physics into OML theory, the model must include these physics as well in order to obtain the full picture.

According to teams at the Los Alamos National Laboratory, plasma drag becomes the dominant force in laboratory-based dusty plasma experiments when the ion flow speeds are high and the plasma density is at least 10^{19} m^{-3} [53] [51]. Otherwise, the gravitational and

electrostatic forces acting on the dust grain will be of comparable magnitude [28]. Provided we are in that plasma drag dominated regime, the motion of a grain is determined by collisional forces between the dust and ions as well as Coulomb interaction forces, though the latter are much weaker in SL theory. For both theories, the charging effects on the dust grains are the primary drivers of these forces [51]. These effects include the influx of ions and electrons into the sheath around the dust as well as the secondary electron emission and thermionic electron emission from the grain surface. Other charging effects such as impact ionization, radioactivity, field emission, photoemission, and tunnelling current are possible, but their contributions are assumed to be small and are thus ignored [43]. The heating effects incurred from interaction with the plasma are also important, since ablation of the dust grain will result in a reduction of both mass and size, thereby changing the force acting upon it [51].

Much of the physics presented here is based off of work done by Ticoş et al. in 2006 at the Los Alamos National Laboratory. Their work focused on a fully ionized hydrogen plasma with densities $n_e = n_i = 10^{19}$ m^{-3}, temperatures $T_e = T_i \leq 15$ eV, and plasma flow velocities of similar order as the ion thermal speed. For these assumptions, they found this model to have good agreement with separate particle-in-cell simulations [51]. The plasmas considered in this thesis will have different properties in many respects, but they will hold to the assumptions that $n_i = n_e$, $T_i = T_e \leq 15$ eV, and v_f will be within one order of magnitude of v_{ti} and much smaller than v_{te}.

Because the electron thermal speed is much greater than both the ion thermal speed and the overall plasma flow speed, the rapid accumulation of electrons will cause the dust grains to become negatively charged almost immediately [43]. For this reason, the equations in this section only apply when the relative potential between the dust grain and the plasma is negative, $V_d \leq 0$. While it is possible for influx of ions and emission of electrons to push this value above zero, this does not apply to most situations studied in this thesis. In the case that this relative potential becomes positive, the model changes all current and heat flux equations to equal zero and outputs a warning message to the user (see Appendix B).

Throughout this study, these warnings only appeared in certain situations in which the dust grain fully ablated. Therefore, the omission of the physics of the $V_d > 0$ regime has little to no impact on the results.

An important note is that this model does not account for any sort of chemical processes which may occur as a result of the interaction of the dust grain material and the plasma. It is likely that such reactions occur, especially in the case of multi-species plasmas like those within teflon PPT exhausts, but such analysis is outside the scope of this thesis. For simplicity's sake, this work mainly considers the use of noble gasses, though this is not a requirement.

2.2 Sheath Limited Charging and Heating

For dust grains that are larger than the Debye length of the plasma, it can be assumed that the grain behaves similar to a floating wall, and thus has a surrounding sheath which affects the flux of particles to and from the grain. In this sense, Sheath Limited theory uses much of the same physics as are used when analyzing a plasma sheath near a wall or probe [49]. Therefore, it is important to understand how the Bohm criterion applies to a flowing plasma.

In general terms, Bohm's criterion states that for a negative absorbing wall, ions are accelerated ahead of the wall such that their entrance into the sheath, a distance one Debye length in front of the wall, occurs at a velocity greater than or equal to the sound speed of the plasma. For this thesis, the sound speed is approximated as $c_s = \sqrt{k_B(T_i + T_e)/m_i}$ [49], where $k_B = 1.380649 \times 10^{-23}$ J/K is the Boltzmann constant, and m_i is the ion mass. In order for a sheath to form, Bohm's criterion must be met, and we must therefore always assume that our dust grains are negatively charged, an assumption that is already established for the model.

Typically, Bohm's criterion is conceptualized as applying to cold ions where $T_i = 0$. This has been generalized for non-cold ions using both distribution functions and fluid equations, but for this situation, we must account for the flow of the ions. In analyzing tokamak edge plasmas in 1984, Stangeby examined the stability of the sheath for subsonic, supersonic,

and hypersonic flow and found that for the majority of real-world cases, the Bohm criterion holds true [49]. Assuming that the ion distribution is well approximated by a Maxwellian distribution of temperature with an overall flow speed, v_f, then the equations for the ion and electron currents are [49] [51]:

$$I_i = 4\pi r_d^2 e n_{si} c_s \tag{2.1}$$

$$I_e = -\pi r_d^2 e n_{se} \sqrt{\frac{8k_B T_e}{\pi m_e}} \exp\left(\frac{eV_d}{k_B T_e}\right) \tag{2.2}$$

Where the charge of an electron is $-1e$, and n_{si} and n_{se} are ion and electron number densities at the sheath edge. These values differ from the plasma density far from the grain due to sheath and presheath effects. The presheath is usually complex, but this difficulty can be avoided by calculating the ion and electron currents on the basis of the sheath edge density, which can be approximated by the relation $n_{s(i,e)} = n_{(i,e)}(2 + v_f/c_s)^{-1}$ [49].

It is important to note that these equations assume that ions and electrons enter the sheath at an angle normal to the surface of the spherical grain. Plasma flow speed might contribute to a change in the shape of the sheath [52] but for our purposes, we assume a spherical sheath, with ions hitting our spherical dust grain normal to the surface.

When energetic electrons impact the dust grain, they can either tunnel through the grain and interact weakly with the material on the way through, or they become trapped within the grain and distribute all their energy into surrounding molecules [43]. The former case will not have much of a net effect on the current, but in the latter, the released energy can excite nearby electrons which then leave the grain. This is secondary electron emission. The amount of particles released through this process can be characterized by the widely used "Sternglass law" [26]:

$$\delta_{se}(E) = 7.4\delta_m \frac{E}{E_m} \exp\left(-2\sqrt{\frac{E}{E_m}}\right) \tag{2.3}$$

Where δ_{se} is the secondary electron emission yield for incident electrons of a given energy

(E), δ_m is the maximum possible yield, and E_m is the energy at which that maximum occurs. Both δ_m and E_m are determined by the material properties of the dust grain. Additionally, for SL theory, only the electron density at the sheath edge is considered, rather than the full plasma density. It should be noted that the Sternglass law was originally derived for a flat plate. Justification for the use of this function rather than other equations for δ_{se} is provided in Section 2.5.

The distribution function of the incident electrons' energies, f_{se}, is assumed to be Maxwellian and follows Equation 2.4, and the secondary electron current is therefore determined to follow Equation 2.5 [43].

$$f_{se}(E - eV_d) = n_{se}\left(\frac{m_e}{2\pi k_B T_e}\right)^{3/2} \exp\left[-\frac{E - eV_d}{k_B T_e}\right] \tag{2.4}$$

$$I_{se} = \frac{8\pi^2 r_d^2 e}{m_e^2}\int_0^\infty E\delta_{se}(E) f_{se}(E - eV_d)dE \tag{2.5}$$

The final charging process included in this model is the thermionic emission current. As the other current effects impart energy to the dust grain, the subsequent rapid heating will also cause electrons and ions to be thermionically emitted from the grain surface [43]. This is the primary processes by which the grain's relative potential will increase and therefore cannot be omitted. This current is calculated using the Richardson-Duschman formula, which accounts for the increase in the work function due to the charged dust surface [43] [51]:

$$I_{th} = \frac{16\pi^2 r_d^2 e m_e (k_B T_d)^2}{h^3} \exp\left(-\frac{W}{k_B T_d}\right) \tag{2.6}$$

Where W is the work function measured in eV and is dependent on the dust grain material, T_d is the dust temperature, and $h = 6.6261 \times 10^{-34}$ J s is Plank's constant.

While it is possible for external magnetic and electrical fields to produce a charging effect, these are relatively small compared to the other effects included here [51]. Also, even though

magnetic fields will obviously be present for any flowing plasma, they do not have an effect on dust grain motion [54]. Similarly, electric fields present in a flowing plasma can be neglected [51], and this model therefore ignores the effects of both fields for both SL and OML theories.

As one would expect, depositing an ice grain into a dense plasma will quickly cause it to melt or ablate. This is true for other situations as well, such as with injecting graphite dust into a tokamak edge plasma [51], though the time required for full ablation varies widely between these situations. The change in temperature directly corresponds to the heat flux to the dust grain from impacting particles, so this study accounts for heat fluxes of incident ions and electrons, emitted secondary electrons, and emitted thermionic electrons. Changes in temperature related to ion or molecular recombination energies are omitted in this thesis.

The primary influx of energy to the dust grain is through the kinetic energy carried by incident ions and electrons deposited as heat. Because we are using SL theory, the amount of incident particles is significantly less than for OML theory. However, since the sheath is assumed to be collisionless and perfectly absorbing, the ions accelerate in the presheath and sheath, changing the amount of energy imparted [51]. The equations use the current terms found above and are given by:

$$\Gamma_i = (2.5 k_B T_i - e V_d) \frac{I_i}{e} \tag{2.7}$$

$$\Gamma_e = 2 k_B T_e \frac{|I_e|}{e} \tag{2.8}$$

In a similar manner, it is assumed that electrons leaving the dust grain through secondary electron emission and thermionic emission convert heat to kinetic energy and then remove it from the grain. These heat fluxes are given by Equations 2.9 and 2.10 [51]:

$$\Gamma_{se} = 2 k_B T_{se} \frac{I_{se}}{e} \tag{2.9}$$

$$\Gamma_{th} = 2k_B T_d \frac{I_{th}}{e} \tag{2.10}$$

Where T_{se} is the energy of one escaping secondary electron and is assumed equal to $T_{se} = 3$ eV.

The final components that influence the change in temperature of the grain are the radiated heat flux, given in Equation 2.11, and heat lost due to sublimated material. Since the latter is dependent on the change in mass of the dust grain, it is discussed in the Differential Equations section.

$$\Gamma_{rad} = 4\pi r_d^2 \sigma (T_d^4 - T_{wall}^4) \tag{2.11}$$

Where $\sigma = 5.6705 \times 10^{-8}$ W/m^{2}K^4 is the Stefan-Boltzmann constant and T_{wall} is assumed to equal 290 K. While the surrounding environment in interplanetary space is not 290 K, changing this value has negligible impact on the output, and it is therefore unaltered.

2.3 Orbital Motion Limited Charging and Heating

When the radius of a dust particle is smaller than the Debye length, $r_d < \lambda_D$, the grain acts less as a wall with a sheath and more like a large plasma particle. Thus, the charging can be well approximated by Orbital Motion Limited theory. In this case, a travelling particle entering the Debye sphere of the grain will change its path due to the electrostatic force of the grain [43]. For negatively charged grains this force will curve the particle in towards the grain. Focusing on the ion current, we first need a distribution function, which is assumed to be a drifting Maxwellian and is given by Equation 2.12 [51]:

$$f_i(\boldsymbol{v_i}) = n_i \left(\frac{m_i}{2\pi k_B T_i} \right)^{3/2} \exp \left[-\frac{m_i (\boldsymbol{v_i} - \hat{z} v_f)^2}{2 k_B T_i} \right] \tag{2.12}$$

Then we define a collecting surface area πb_c^2 dependent on V_d, where $b_c = r_d \sqrt{1 - 2eV_d / m_i v_i^2}$ is an effective collection radius for ions impacting the grain, and v_i is the ion velocity far

from the grain. These equations can then be used to generate an ion current for the flowing plasma [51]:

$$I_i^{(f)} = e \int_{v_{min}}^{\infty} \pi b_c^2 v_i f_i(\boldsymbol{v_i}) d^3\boldsymbol{v_i} \tag{2.13}$$

Where v_{min} is the minimum speed required for an ion to overcome the potential barrier surrounding the dust grain. Since we only consider negatively charged grains, $v_{min} = 0$. This integral can then be arranged as a projection of the velocity on the z axis and evaluated according to Reference [51].

$$I_i^{(f)} = \pi r_d^2 e n_i \sqrt{\frac{8k_B T_i}{\pi m_i}} \left[\frac{\sqrt{\pi}}{4u} \left(1 + 2u^2 - \frac{2eV_d}{k_B T_i} \right) \mathrm{erf}(u) + \frac{1}{2} \exp(-u^2) \right] \tag{2.14}$$

Where $u = v_f / v_{ti}$ is the normalized ion flow speed, and $\mathrm{erf}\,(u) = 2/\sqrt{\pi} \int_0^u \exp(-x^2) dx$ is the error function.

For all cases considered in this study, the plasma flow speed v_f was always much less than the electron thermal speed v_{te}. Thus, the flow speed does not need to be accounted for when considering the electron current I_e, and we use a similar formula as Equation 2.2 [51]. For OML theory, we do not need to worry about sheath effects, so the electron density considered is that of the plasma, n_e, rather than n_{se}.

For secondary electron emission, the n_{se} term in the incident electron energy distribution function given by Equation 2.4 is also replaced by the full plasma electron density n_e. All other reasoning holds, and there are no other changes in the secondary electron current between SL theory and OML theory. Additionally, there are no terms to be changed for I_{th} in Equation 2.6, which is the same for both theoretical models.

Shifting to the heat flux in OML theory, the primary change from SL theory is again in the ion term. As with ion current, we must account for the collection radius b_c and the velocity distribution of incident ions as found in Equation 2.12 [51]. Thus, the formula for the flowing ion heat flux in OML theory is:

$$\Gamma_i^{(f)} = \int_{v_{min}}^{\infty} \pi b_c^2 v_i \left(\frac{m_i v_i^2}{2} - eV_d \right) f_i(\boldsymbol{v_i}) d^3\boldsymbol{v_i} \tag{2.15}$$

Where $v_{min} = 0$ again since only negatively charged grains are considered.

This can then be evaluated to get the computer-executable version of the flowing ion heat flux for the $V_d \leq 0$ regime [51]:

$$\begin{aligned} \Gamma_i^{(f)} =& \sqrt{\pi} r_d^2 n_i (k_B T_i) \frac{v_{ti}}{u} \left\{ u \left(\frac{5}{2} + u^2 - \frac{2eV_d}{k_B T_i} \right) \times \exp(-u^2) \right. \\ &\left. + \sqrt{\pi} \left[\frac{3}{4} + 3u^2 + u^4 - \frac{eV_d}{k_B T_i} \times \left(1 + 2u^2 - \frac{eV_d}{k_B T_i} \right) \right] \operatorname{erf}(u) \right\} \end{aligned} \tag{2.16}$$

The remainder of the heat flux terms – those for incident electrons, thermionic emission, secondary electron emission, and heat radiation – are the same as those in Equations 2.8, 2.9, 2.10, and 2.11, respectively. Though it is important to employ the modified equations for I_e and I_{se} that use the plasma electron density n_e rather than the sheath limited electron density n_{se} as outlined above [51].

2.4 Forces and Differential Equations

The drag forces acting on a dust grain are dependent on dust grain speed v_d, radius r_d, and potential relative to the plasma V_d. Each of these terms are dependent on each other as well as on other terms like mass m_d and temperature T_d, and they are all varying in time. Therefore, it is important to present the coupled ordinary differential equations (ODEs) that define these terms so that they can be properly solved.

The charging ODE given by Equation 2.17 provides the time rate of change for the relative potential V_d and is dependent on the current formulae found in the previous sections. For SL theory, I_i, I_e, I_{se}, and I_{th} are given by Equations 2.1, 2.2, 2.5, and 2.6, respectively. In OML theory, I_i is given by Equation 2.14, while I_e and I_{se} are the same as with SL theory with the appropriate change to n_e rather than n_{se}. The formula for I_{th} is the same for both

theoretical models. The capacitance of the grain, C_d, is given by the Debye-Hückel formula $C_d = 4\pi\epsilon_0 r_d(1 + r_d/\lambda_D)$, where $\epsilon_0 = 8.8542 \times 10^{-12}$ F/m is the permittivity of space.

$$C_d \frac{dV_d}{dt} = I_e + I_i + I_{se} + I_{th} \tag{2.17}$$

The mass ODE given by Equation 2.18 assumes that dust mass is lost evenly in all directions and can be determined by first integrating the Clausius-Clapeyron equation [45]. Here, n_0 is the vapors density of the dust material at a specific temperature T_0 [51]. In this study, these values were found using the ideal gas law, $n = P/k_B T$, choosing a temperature T_0 along the sublimation curve of the dust material's phase diagram, and using the corresponding pressure to calculate n_0. Additionally, m_0 is the dust material molecular weight in amu, Λ_s is the material sublimation heat in J/mol, and $R = 8.31$ J/mol K is the gas constant. This formula is used to help calculate the sublimation heat loss term in Equation 2.19 and the change in dust size in Equation 2.20.

$$|\dot{m}_d| = 4\pi r_d^2 m_0 \sqrt{\frac{2k_B T_d}{\pi m_0}} \frac{n_0 T_0}{T_d} \exp\left[\frac{\Lambda_s}{R}\left(\frac{1}{T_0} - \frac{1}{T_d}\right)\right] \tag{2.18}$$

The heating ODE given by Equation 2.19 assumes that the volume of the spherical dust grain is heated uniformly. In this formula, the mass of the grain is found with the equation $m_d = 4\pi r_d^3 \rho_d/3$ where ρ_d is the grain material density, and c_d is the material's specific heat. The final term provides the heat lost due to sublimation of the material away from the dust grain where Λ_s is the sublimation heat and μ is the molecular weight in kg/mol. The heat flux terms found in the previous subsections – heat flux from incident ions, incident electrons, secondary electron emission, thermionic emission, and heat radiation – are represented by the terms Γ_i, Γ_e, Γ_{se}, Γ_{th}, and Γ_{rad}, respectively. In SL theory, Γ_i is given by Equation 2.7, while in OML theory, it is given by Equation 2.16. The remainder of the heat flux terms are the same for both theories, though one still must use the proper current terms for the

respective theoretical model.

$$m_d c_d \frac{dT_d}{dt} = \Gamma_e + \Gamma_i - \Gamma_{se} - \Gamma_{th} - \Gamma_{rad} - \frac{\Lambda_s}{\mu}|\dot{m}_d| \tag{2.19}$$

The radius ODE given by Equation 2.20 relies on the assumption that mass, and therefore radius, is lost uniformly in all directions. This assumption is accounted for in $|\dot{m}_d|$ term given by Equation 2.18.

$$\frac{dr_d}{dt} = -\frac{\dot{m}_d}{4\pi r_d^2 \rho_d} \tag{2.20}$$

Before discussing the remainder of the ODEs, which all contribute various insights to the equations of motion of the dust grain, expressions for the forces on the grain must be presented. As previously discussed, the high speed and density of the plasmas studied in this thesis cause plasma drag to be orders of magnitude stronger than the force of gravity, electrostatic forces, or electrodynamic forces on the grain. The plasma drag force itself can be split into two separate effects that both assume a singly ionized plasma. The first is a direct impact force F_{col} given by Equation 2.22 that assumes collisions with the grain are completely inelastic. And the second is a long-distance Coulomb interaction force F_{Coul} given by Equation 2.22 that assumes the mean free path of the plasma particles is much larger than the grain radius [9] [51]. For SL theory, F_{Coul} can be neglected, and only F_{col} is accounted for, though this also assumes that any particle entering the sheath impacts the grain. For OML theory, F_{Coul} is of the same order of magnitude as F_{col} and is thus included.

$$F_{col(i,e)} = 2\pi r_d^2 k_B T_{i,e} n_{i,e} G_0(s_{i,e}) \tag{2.21}$$

$$F_{Coul(i,e)} = 2\pi r_d^2 k_B T_{i,e} n_{i,e} \phi_{i,e}^2 \ln(\Lambda_{i,e}) G_2(s_{i,e}) \tag{2.22}$$

In these equations, $s_{i,e}$, $\phi_{i,e}$, and $\Lambda_{i,e}$ are provided by the formulae in Equation 2.23.

$$s_{i,e} = \sqrt{\frac{m_{i,e}(v_f - v_d)^2}{2k_B T_{i,e}}}, \qquad \phi_{i,e} = \frac{eV_d}{k_B T_{i,e}}, \qquad \Lambda_{i,e} = \sqrt{\frac{\epsilon_0 k_B T_{i,e}}{n_{i,e}}} \frac{3}{e|\phi_{i,e}| r_d \left(1 + \frac{r_d}{\lambda_D}\right)} \tag{2.23}$$

Further, the equations for $G_0(s)$ and $G_2(s)$ are provided by Equations 2.24 and 2.25, respectively. These functions are actually approximations for the full formulae.[1] However, Draine and Salpeter found that the $G_0(s)$ function used in Equation 2.24 is accurate to within 1% of the precise value for $0 < s < \infty$, and $G_2(s)$ used in Equation 2.25 is accurate to within 10% for $0 < s < \infty$ [9]. These functions are much more computationally efficient than the full formulae, simpler to implement than other alternative expressions [3], and provide enough accuracy for this analysis.

$$G_0(s) = \frac{8s}{3\sqrt{\pi}} \left(1 + \frac{9\pi}{64} s^2\right)^{1/2} \tag{2.24}$$

$$G_2(s) = s \left(\frac{3}{4}\pi^{1/2} + s^3\right)^{-1} \tag{2.25}$$

When analyzing the effect of the forces on the dust grain with a hydrogen plasma, it has been found that drag forces contributed by electrons are much less than 10% the magnitude of the same forces contributed by ions [9] [51]. Since this is due in large part to the mass disparity between protons and electrons, it is safe to assume that eletron drag forces will contribute even less when dealing with heavier ions as done in this study. Electron drag forces are thus neglected.

---

[1] The precise formulae for $G_0(s)$ and $G_2(s)$ are provided by Draine and Salpeter [9], but are not used for this model for the sake of computational efficiency.

$$G_0(s) = \left(s^2 + 1 - \frac{1}{4s^2}\right) \operatorname{erf}(s) + \left(s + \frac{1}{2s}\right) \frac{\exp(-s^2)}{\sqrt{\pi}}$$

$$G_2(s) = \frac{\operatorname{erf}(s)}{s^2} - \frac{2\exp(-s^2)}{s\sqrt{\pi}}$$

Finally, we come to the equations of motion of the dust grain. Solving Equation 2.26 will provide the velocity profile of the dust grain over time, which can then be used in Equation 2.27 to solve for the displacement. As previously noted, SL theory only takes the collision force F_{col} into account, so for dust grains $r_d > \lambda_D$, only the first term of Equation 2.26 is used. Whereas both terms are used in OML theory.

$$m_d \frac{dv_d}{dt} = F_{col(i)}(r_d, v_d) + F_{Coul(i)}(V_d, r_d, v_d) \tag{2.26}$$

$$\frac{dx_d}{dt} = v_d \tag{2.27}$$

Solving Equation 2.28 gives us the position of the dust grain relative to the front of the plasma sheet. As presented here, this model does not directly account for a plasma sheet of finite length. Instead, the dust grain theoretically manifests into a cloud of plasma with the specified input characteristics, and it is flowing through this surrounding plasma throughout the entire duration of analysis. Therefore, this value stores the hypothetical length of the plasma sheet at any point in time. This relative position z_r is used to find the time at which the grain travels through a certain distance of plasma, which can then be used to find the relevant properties of the grain after travelling through a plasma sheet of that length. Consequently, this study assumes there are no forces before or after the plasma sheet and that grain ablation stops immediately after exiting the plasma.

$$\frac{dz_r}{dt} = v_d - v_f \tag{2.28}$$

All of these equations were incorporated into a MATLAB program (see Appendix B), and the six coupled ODEs were solved with MATLAB's ODE45 solver, which is investigated in another section. This model was initially validated by using the same graphite dust grain

properties and hydrogen plasma parameters as Ticoş et al. [51], and was found to have good agreement with their outputs.

2.5 Incorporating the Properties of Water Ice

Since this model was originally designed for studying carbon-based dust grains injected into either tokamak edge plasmas or coaxial plasma gun exhausts [51], it had to be adapted somewhat in order to fit the interests of this study. Namely, the physical properties of the dust grain and the timespan of analysis had to be altered so that this model could be applied to analyzing an interplanetary ice grain travelling through a sheet of plasma from a PPT. One addition to the code – the inclusion of the relative position ODE in Equation 2.28 – has already been discussed in the previous section. We now delve into other investigations required to adapt this model.

In shifting the focus to dust grains made of water ice rather than grains of carbon, many of the basic material properties are readily available and can be pulled from any convenient source. These common characteristics include the density, molecular weight, molecular density, specific heat, and sublimation heat. For water ice, the values for these attributes are $\rho_d = 916.8$ kg/m^3, $m_0 = 18.015$ amu, $\mu = 18.015 \times 10^{-3}$ kg/mol, $c_d = 2030$ J/kg K, and $\Lambda_s = 51100$ J/mol, respectively.

Some material-dependent properties were much less readily available. For example, it was difficult to find information for the work function of water ice – required for use in evaluating the thermionic emission current in Equation 2.6 – which is assumed to be $W = 4.2$ eV in this study [41]. Further, the mass ODE in Equation 2.18 calls for the vapors density of the dust material at a specific temperature, which is essentially the number density of the gaseous form of the dust material at sublimation pressures. The method used for finding these traits was discussed in the previous section and found that the relevant values of these properties for water ice are $n_0 = 2.897 \times 10^{22}$ m^{-3} at the temperature $T_0 = 250$ K.

Other major decisions about how to handle ice grains revolved around the secondary electron emission yield. Typically, the Sternglass law given in Equation 2.3 is used in ap-

plications where incoming electrons impinge upon relatively thick flat sheets of material. Other equations exist which would more accurately simulate the secondary electron yield δ_{se} for small spherical grains [9] [26] [41], but the Sternglass law is more widely used and thus offers better flexibility for adapting this model to simulate dust grains of differing material. Luckily, for lower energy incident electrons in the range of tens of electronvolts or less, such as those used in this study, secondary electron emission has much less of an effect on the overall net current between the dust grain and the plasma [41]. Furthermore, while there are obvious disparities in δ_{se} between planar sheets, larger grains on the order of 10 μm, and smaller grains on the order of 100 nm, these differences are negligible for the cooler electron temperatures studied in this thesis [41]. Therefore, it is reasonable to simply adapt the Sternglass law and use the appropriate δ_m and E_m values for the dust material.

An early comprehensive source for secondary electron emission data was Bruining's 1954 book *Physics and Applications of Secondary Electron Emission*, which provides relevant data for a wide range of elements and molecules, including carbon but not water [5]. The primary source for secondary electron emission from water ice is a 1960 paper from Soviet scientists Matskevich and Mikhailova [31] and can be found in many other papers studying this problem [4] [41] [26]. Richterová et al. used this data and an adapted model for δ_{se} to analyze the secondary electron yield for various grain sizes. They also present a model for backscattered electrons, but the production rate of these particles is much less than that of δ_{se}, and this effect is ignored in this study. The author of this thesis adapted the Sternglass law to fit the function found by Richterová et al. in the lower energy range as shown in Figure 2.1. Although all the reasoning in the previous paragraph remains true, our chosen values of $\delta_m = 2.8$ and $E_m = 600$ eV still incorporate some of the considerations for micron-sized ice grains for the sake of robustness.

Another adaptation of the original model provided by Ticoş et al. is the shortening of the timeframe of analysis. Because of the relative speeds between the dust grain and the plasma sheet as well as the theoretical length of that sheet, most dust grains will only have a few microseconds to interact with the plasma. Comparatively, the timescales of a few

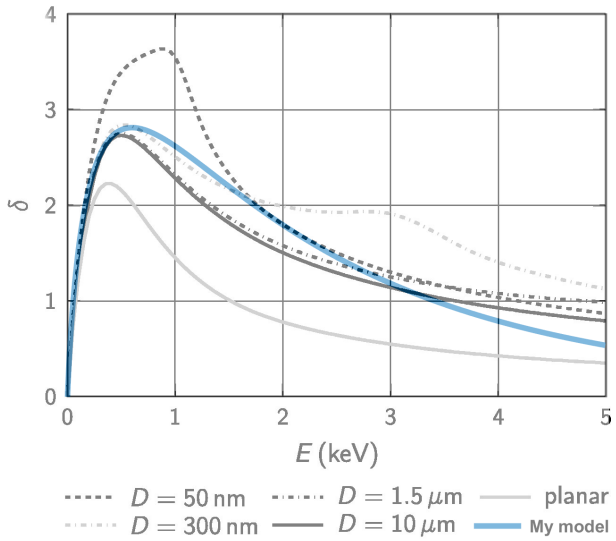

Figure 2.1: Secondary electron yield δ found by Richterová et al. [41] for various diameters D of dust grains overlayed with the formula used in this model as given by Equation 2.3.

milliseconds analyzed for graphite dust grains in coaxial plasma gun exhausts were three orders of magnitude greater.

One final note here is that ice in the laboratory setting will likely be different from ice grains collected near Enceladus or Europa. This is important for adapting this model for an experiment versus for a scientific instrument. It is well known that water ice has many different phases other than the garden variety found in most circumstances on Earth. For this study, all phases of ice are assumed to share the same material properties, but additional research would be needed to verify this assumption. Additionally, lab ice and interplanetary ice are likely to be at different temperatures, exist at disparate initial charge states, and have dissimilar molecules or impurities dissolved into them. For ice grains at Saturn, Jurac et al. found that the potential V_d varies from -5 V at four Saturn radii (which is approximately where Enceladus orbits) to +5 V at greater than eight Saturn radii [26] [41]. Ultimately, initial potential should not matter since rapid accumulation of fast moving electrons should force the grain voltage to a negative equilibrium value almost immediately. Further, dissolved

molecules should have little affect because ions in solution are repelled from the edge of liquid water droplets and are expected to remain that way when frozen, thus keeping several atomic layers of pure ice at the surface [41].

2.6 Energy and Dust Collection Considerations

Having outlined the theoretical model used to analyze the transit of a single ice grain through a plasma sheet, an algorithm must now be developed in order to determine the feasibility and practicality of such a system. This can be split into two separate but connected calculations: the energy required to generate the plasma within the PPT, and the mass of ice collected in one pass.

The required energy calculations are straightforward. We first determine the energy per unit volume, or energy density, for the chosen plasma, then multiply it by the desired volume of that plasma for one shot. The energy density ϵ_p is found by taking the kinetic energy and internal energy – dependent on the ion mass, plasma flow speed, and plasma temperature – for one ion and multiplying by the number density of the plasma as shown in Equation 2.29. This is then multiplied by the area of the collector and desired length of the plasma sheet to get the total energy E_p for one cycle of the PPT as shown in Equation 2.30. This value will help determine if the designed PPT is even plausible.

$$\epsilon_p = \left(\frac{1}{2} m_i v_f^2 + \frac{5}{2} k_B T_p\right) n_p \tag{2.29}$$

$$E_p = \epsilon_p \pi r_p^2 L_p \tag{2.30}$$

We must also find the mass collected by the system to determine how this study compares to other dust collection proposals, but we must first understand the size distribution of particles a collector is likely to encounter in a pass. To this end, this thesis focuses on a spacecraft flying through the plumes at Enceladus, in part because the Cassini mission has

enabled a more thorough understanding of the Enceladus plumes than is presently known about the geyser plumes at Europa. Presumably, these plumes have similar enough characteristics that the equations given here can be adapted once a detailed mathematical model of Europa's plumes becomes available.

According to recent analysis by Porco et al. [37], there are a number of factors at play that influence the geyser activity at Enceladus. Primarily, a diurnal cycle exists that is dependent on the moon's mean anomaly in its orbit around Saturn. The number density of particles inside the plume can vary by more than an order of magnitude between the maximum and minimum of this cycle. It is likely that longer scale cycles exist that are caused by harmonics between the orbital periods of various Saturnian moons as well as the location of Saturn in its orbit of the sun [37]. This study will examine a best-case and worst-case pass in order to get a theoretical range of possible mass collected.

No matter the overall plume output, the particles are expected to follow a differential size distribution $dN/dr \propto r^{-q}$ where $q = 3$ for a 50 km altitude pass and $q = 4$ for a 100 km pass [37]. In both cases, the radius of the ice grains is considered to range from $r_d = 0.01$ μm, below which point particles are considered to be vapor, up to $r_d = 10$ μm. Porco et al. then provide a table, which has been modified and reproduced in Table 2.1, that gives the gives the number density for particles over a specified size for a pass at a given altitude while Enceladus was at a certain mean anomaly. This table also provides the full-width half-maximum (FWHM) for the plume at a given altitude, which is used as the length of the flyby in this study.

In order to calculate the size distribution, one must use the information in Table 2.1 to solve Equation 2.31 for the relevant constant C:

$$\int_{r_d=r_{min}}^{r_d=10\mu m} dN = \int_{r_{min}}^{10\mu m} C r_d^{-q}\, dr_d = n_{table} \tag{2.31}$$

Where n_{table} is the is number density above a certain minimum dust grain radius r_{min} for the pass you want to analyze, as found in Table 2.1, and q is dependent on your flyby altitude as discussed previously.

Instrument	*Alt* (km)	*FWHM* (km)	*MA* (deg)	n_d (#/m^3) for $r_d > 0.5$ μm	n_d (#/m^3) for $r_d > 1.5$ μm
CDA - E7	100	232	265	-	9
ISS - 'E7'	100	285	269	134-125	15-5
CDA - E21	50	46	103	-	65
ISS - 'E21'	50	100	100	867-782	94.4-29
ISS - Early min	50	172	344	187-182	20-7
ISS - Early max	50	92	208	3540-3340	385-124
ISS - Late min	50	258	320	107-96.8	12-3.6
ISS - Late max	50	91	209	1990-1780	216-66

Table 2.1: Modified version of Porco et al.'s Table 2 [37]. CDA is the Cosmic Dust Analyzer, which detected grains larger than 1.7 μm in plume passes (distinction between 1.5 and 1.7 ignored here). ISS is the Imaging Science Subsystem used for photometric modeling of the plume (range of values provided is for $q = 3$ to $q = 4$ size distributions). E7 and E21 are individual Enceladus flybys; "min" and "max" values depend on mean anomaly (MA); "early" and "late" account for longer term variations.

Stepping back a bit, it is relevant to discuss what happens to these dust particle distributions when they interact with the plasma. Prior to passing through the plasma sheet, the size of the particles is assumed to adhere to the differential size distribution outlined above, and the velocity of the particles is assumed to be low relative to the velocity of the spacecraft such that all particles practically share the same initial velocity. As will be discussed in more detail in a later section, interaction with the plasma will have different results for differing sizes of ice grain. Ice smaller than a certain radius will completely ablate, smaller grains that do not fully ablate will have their velocities reversed, and the remainder of the ice grains will have some final velocity between zero and the initial velocity. Of the ice in the final group, only those grains below a certain radius will have slowed enough to efficiently preserve the possible organic material or molecules inside. Figure 2.2 further demonstrates the size and velocity distributions of incoming dust grains and how they are affected by the plasma sheet.

We will use r^*_{d1} to indicate the final radius of dust grains with zero velocity after passing through the plasma, and r^*_{d2} to indicate the final radius for grains whose final velocity is the maximum allowable speed at which significant organic material can be recovered (assumed 3 km/s in this study). The model outlined in this thesis can easily be used to determine these values. Since ablation of the grains behaves approximately linearly, interaction with the plasma will shift the original differential size distribution to the left by a certain amount Δr_d, which can be found by subtracting the final size of a grain from its initial size.

The relevant mass collected in a pass m_c can then be found according to Equation 2.32:

$$m_c = \int_{r^*_{d1}}^{r^*_{d2}} \frac{4}{3}\pi r_d^3 \rho_d (\pi r_p^2) FWHM \left(\frac{dN}{dr_d}(r_d + \Delta r_d) \right) dr_d \tag{2.32}$$

Where $dN/dr_d(r_d) = Cr_d^{-q}$ with C being the value calculated in Equation 2.31 and $q = 3$ (for 50 km passes) or $q = 4$ (for 100 km passes). This collected mass can be used to compare this method with other collector proposals in order to discuss benefits and drawbacks.

One other relevant term to evaluating the feasibility of this system is the rate at which dust particles impact the collector, R_d. This value is given by Equation 2.33 and improves

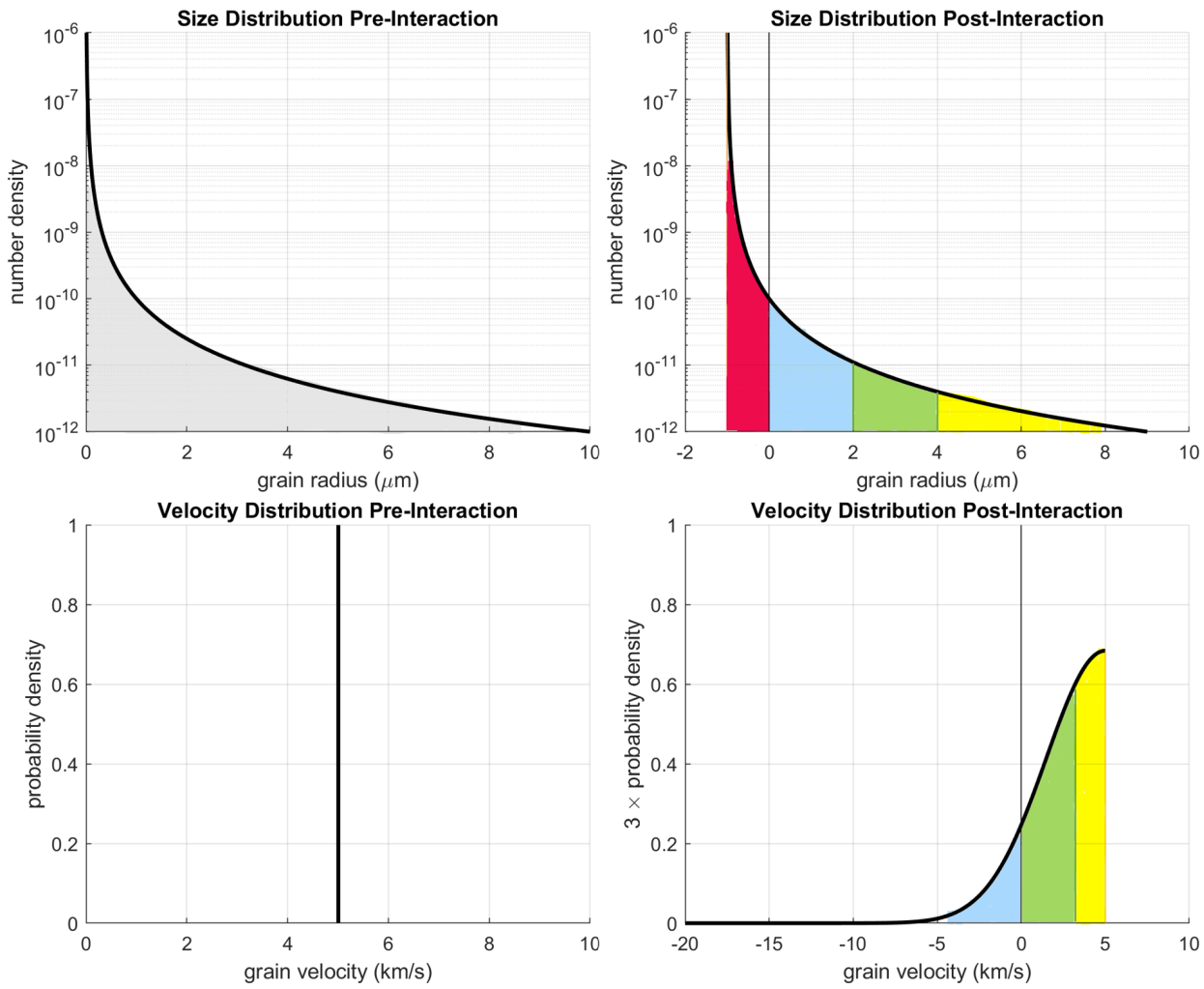

Figure 2.2: The graphs on the left show the initial distributions of grain size and velocity, and thos on the right show the final distributions after interacting with the plasma. The differential size distributions dN/dr use $C = 10^{-10}$ and $q = 3$ as example values and give al number density. The velocity graphs simply give a probability density, with the post-interaction values boosted for clarity. Red represents fully ablated grains, blue - rejected grains, green - grains able to be captured, and yellow - grains with excess velocity.

understanding for the feasibility of this project.

$$R_d = \frac{n_d FWHM(\pi r_p^2)}{FWHM/v_{d0}} \tag{2.33}$$

Where n_d is the number density of particles larger than a certain radius, which can easily be found in Table 2.1 or by integrating $dN/dr(r_d)$ used in Equation 2.32 for the relevant radii; and v_{d0} is the initial relative velocity between the grain and the spacecraft. $FWHM$ technically cancels itself out, but is left in the equation for clarity.

Chapter 3

DISCUSSION OF THE PLASMA DRAG MODEL AND OUTPUTS

Now that all the relevant math and physics has been established, it is time to shift focus to the intricacies of the model itself. In this Chapter, we will discuss the inner workings and limitations of the model as well as go into detail on the information and types of plots it produces along with how these can be used for further analysis.

3.1 Method and Limitations

The backbone of the model is the numerical ODE solver used to compute the six coupled differential equations outlined in the Forces and Differential Equations section. MATLAB's ODE45 was used for this purpose. This function uses an explicit Runge-Kutta (4,5) method known as the Dormand-Prince pair to solve nonstiff differential equations with medium accuracy [30], and it was chosen because it fit the mathematical requirements well, is commonly used, and the author has good knowledge of its operation in solving complicated numerical problems from previous work [25]. The relative error tolerance and absolute error tolerance values were kept at the default values of 1×10^{-3} and 1×10^{-6}, respectively, since extreme numerical accuracy was not needed in this initial study. ODE45 has the ability to choose its own timesteps, but this capability was not utilized in this study. Instead, a maximum time was chosen based upon the desired length of the plasma sheet and the relative velocity between the plasma and the grain; then the timestep was arranged to be at least three orders of magnitude lower than that maximum time. This decision may reduce the precision of the final output, but this was seen to only affect dust grains that fully ablated. Explicitly defining timesteps also ensured that a precise time could be cross-referenced in other outputs if

needed.

Some of the limitations of this model have already been mentioned, such as the decision to not include chemical effects on the grain, but it seems prudent to mention the majority of these constraints explicitly in one location. The most obvious restriction of this model is the exclusion of physics phenomenon in the positive relative potential regime, $V_d > 0$. Implementation of these physics, even while using the same assumptions, would complete this model, but this was not a priority for this paper since it rarely occurs. When it does, it is usually for dust grains that will fully ablate anyway. Another constraint is that, as the code is currently written, the initial grain velocity relative to the spacecraft v_{d0} must be negative, and the plasma flow velocity v_f must be positive, otherwise the results might show the grain accelerating instead of decelerating. This bug was not able to be resolved, but it has no effect on the accuracy of the results presented here.

Most other model limitations are related to assumptions made and terms neglected due to their small effects. This study assumes the plasma is a singly ionized noble gas of uniform density with distinct borders. We know from studies of teflon PPTs that non-elemental fuels will likely break down into various elements and compounds upon ionization, and it is unlikely for all of these constituent molecules to only be singly ionized [44]. Enabling the analysis of multi-species plasmas, including neutrals, would enhance the accuracy of this model for a wider range of propellants. Further, implementing a finite plasma sheet into the model and enabling it to have diffuse edges and nonuniform density would reveal greater insight into the physics of this interaction, such as varying deceleration rates due to density fluctuations and the possibility for continued ablation after a dust grain leaves a plasma.

Many assumptions were made around the physics of the dust grain as well, though most have been justified in other parts of the thesis. Physics such as possible shattering of small ice grains was completely ignored, and several dust-plasma interaction effects like photoemission of electrons, electron tunnelling, backscattered electrons, field emission, and impact ionization are unaccounted for in this model due to their weak effects relative to the interactions that were included. On that note, weaker forces such as electrostatic forces, gravitational

forces, drag from electrons, long distance Coulomb interactions for grains in the SL regime, and any possible neutral drag are ignored in favor of their stronger counterparts as well.

Lastly, the two approaches used to understand the physics of this interaction, SL theory and OML theory, work best when the grain radius is far from the Debye length. Though this is the case for the larger grains analyzed in this study, there are also many instances where r_d approaches or crosses the discontinuity that exists at $r_d = \lambda_D$. While this is not a major issue, it is obvious that a smoother transition phase is needed to fully grasp the physics in this regime.

Ultimately, all of these effects were considered insubstantial or outside the scope of this study. Perhaps an accumulation of all of these individually negligible processes would make a difference to the outcome, or perhaps not. Instead of spending the time needed to incorporate all these effects, it would likely be better to devise an experiment to test the assumptions outlined in this model. Unfortunately, logistical challenges imposed by the COVID-19 pandemic prohibited the author from devising or testing such an experiment.

3.2 Time Dependent Plots

The most straightforward way to use this model is to simply observe how a few key outputs change with respect to time and how changes to various initial parameters affect these outputs. For our purposes, we are most concerned with the change in velocity of a dust grain over time and the survivability of that grain. Since all of the differential equations are coupled, it is also of interest to examine how temperature and relative voltage of the dust grain change as well. To this end, the key outputs to be examined with respect to time are the dust potential relative to the plasma V_d, the dust temperature T_d, the dust ablation r_d/r_{d0} where 1 is no ablation and 0 is full ablation, and the dust speed relative to the spacecraft v_d.

Before producing and examining these plots, it is important to establish a common baseline of input values as a type of control to compare against. For these time dependent plots, we want to ensure we are looking at the relevant timescale for the interaction of a grain with

a PPT exhaust plasma. For this analysis, we will primarily be looking at a 2 - 5 cm plasma sheet with a speed of around 20 - 30 km/s, so a maximum time of $t = 3 \times 10^{-6}$ seconds should capture the data we are looking for as a first approximation. At this speed, it was found that a plasma density of around $n_p = n_{i,e} = 10^{22}$ m^{-3} had enough influence on the grain to demonstrate the effects of changing input parameters.

Other baseline input parameters included a plasma temperature $T_p = T_{i,e} = 10$ eV, a plasma ion mass of $m_i = 131.29$ amu (that of Xenon), a plasma flow speed of $v_f = 30$ km/s, an initial dust grain radius of $r_{d0} = 1$ μm, an initial dust speed of $v_{d0} = -7000$ m/s, an initial dust temperature of $T_{d0} = 100$ K, and an initial relative potential of $V_{d0} = -5$ V. For all plots, we are using the material properties of water ice for the dust grain. The plots included here demonstrate how changing these parameters affects the key outputs mentioned above.

Our examination begins by looking into the effects of changing the initial properties of the dust grain itself. To this end, changing the grain's initial temperature, radius, potential relative to the plasma, and speed relative to the spacecraft were all examined. Differences in potential V_{d0} had no noticeable effect on any of the plots, and variations in the dust's speed v_{d0} vertically shifted the speed plots and had no other effect. Those plots can be found in Appendix A. The potential change had no significance due to the fact that fast moving electrons will always bring the initial relative potential to an equilibrium state almost instantly, and the charging, heating, and force effects rely heavily on that equilibrium value. Similarly, changing the initial dust speed does not affect any of the charging or heating equations, and the first three graphs are therefore unaltered by changing this value. Changing the value of T_{wall}, which would influence the radiated heat term, also had no effect.

Looking now at Figure 3.1, we see our first glimpse at a variable influencing multiple output parameters. This figure shows that changing the initial dust grain temperature, in isolation of other changes, will delay the time at which the grain reaches an equilibrium temperature, but it does not change the rate at which this heating occurs. The more rapidly the grain reaches the equilibrium temperature, the more it will ablate in a given timeframe. Although this effect is minor here, examination of other outputs revealed that a cooler initial

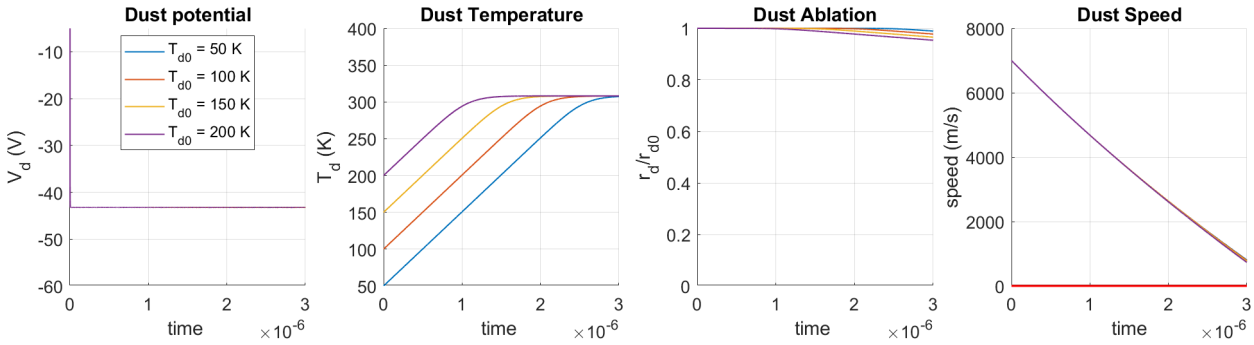

Figure 3.1: Changing the initial temperature of the dust grain does not change equilibrium values for dust potential or temperature. It affects how soon a grain will reach equilibrium T_d, which somewhat alters ablation and barely influences speed.

temperature will effectively delay the onset of ablation, which in turn delays deceleration as well since the drag force is linked to the grain size. Therefore, for a given time within the plasma, the final Δv_d will be smaller for colder grains, everything else being equal. This outcome is much more prevalent in OML theory and longer time frames of analysis.

Examining Figure 3.2 lends insight into how a detector flying through a field of various grain sizes will treat populations of differing radii. As expected, they all share the same equilibrium potential and temperature, though they take differing amounts of time to reach the latter. Smaller grains reach this temperature first and experience larger amounts of ablation, but the most interesting graph in this figure is the Dust Speed. Here, we observe the rejection of surviving grains in a reversal of their velocity. Some smaller grains are thus being rejected by the collector and are headed the opposite direction of the spacecraft. This is not ideal since this represents potential mass that was unable to be collected. Luckily, the system only rejects smaller particles, but this indicates that there is a tradeoff associated with slowing larger grains and rejecting smaller ones.

We now move on to examining the effects of changing various plasma parameters, including plasma temperature, ion mass, plasma density, and flow speed of the plasma. These

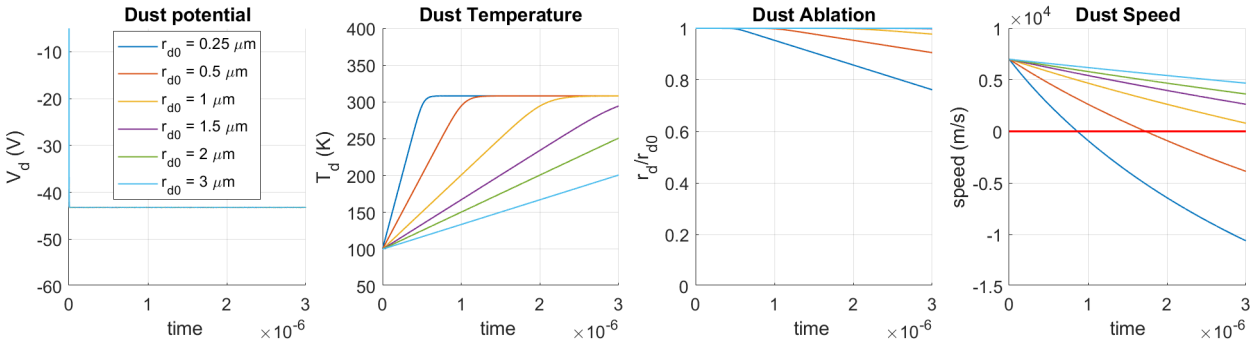

Figure 3.2: Changing the grain's initial radius does not affect its equilibrium potential or temperature. It does alter the time to reach equilibrium T_d, which changes ablation rates. Dust size has a large impact on velocity.

characteristics have more to do with the design of the collector plasma sheet itself rather than the various environments it may encounter in a flyby. Changes in these properties also produce more interesting and dynamic variations than seen in the previous figures.

First, consider Figure 3.3, in which we examine the effects that occur from changing the plasma temperature. Variations in this parameter alter the equilibrium potential and equilibrium temperature of the dust grain. As one would expect, larger plasma temperatures will translate to higher dust temperatures which are reached more quickly and thus result in increased ablation rates. Higher equilibrium temperatures also correspond to a greater absolute value for the equilibrium potential. Interestingly, these changes do not seem to significantly influence the final speed of the grain.

Since lower plasma temperatures seem to lessen ablation without greatly affecting speed, a lesser plasma temperature might be less likely to reject smaller dust grains, though for our parameters, rejection is more of a product of drag force than ablation. This would also decrease the energy density of the plasma as given in Equation 2.29, but is probably less realistic in the sense that getting a cooler plasma to the same speed might not be practical. Additionally, lowering temperature in isolation will cause the value of v_f/v_{ti} to increase, which

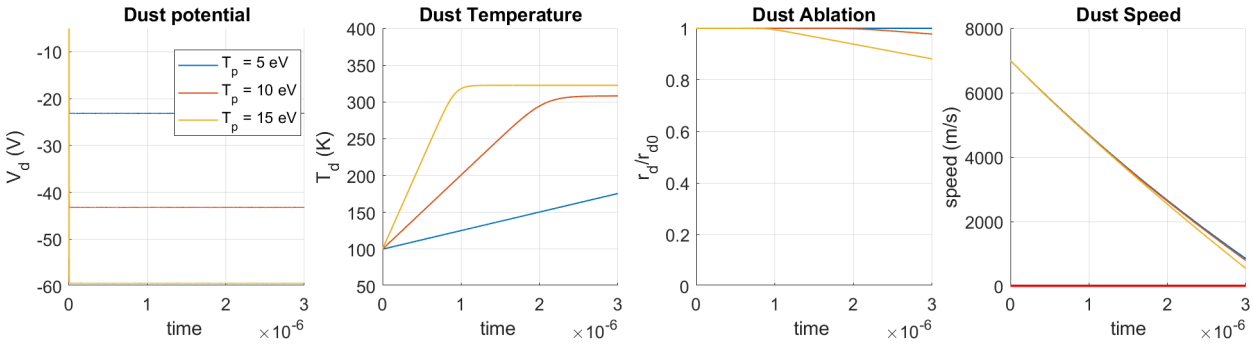

Figure 3.3: Changing the plasma temperature modifies the equilibrium potential, which alters the equilibrium temperature and heating rates, which then influences ablation. These changes do not have much effect on the dust grain speed.

might worsen the assumptions made for SL theory. This could be mitigated by decreasing flow speed or reducing ion mass in tandem with lowering the plasma temperature.

Another plasma parameter to consider is the ion mass, as demonstrated in Figure 3.4. This is dependent on the type of propellant used in the PPT, and changing its value can have unintuitive results. Working from right to left, we see that heavier ions generally produce larger changes in speed due to their more forceful collisions with the grain in SL theory. Curiously, the same heavier ions result in less ablation and lower equilibrium temperatures than their lighter counterparts. Further, contrary to changes in plasma temperature in Figure 3.3, higher equilibrium temperature corresponds to lesser magnitudes of equilibrium temperature.

One other note in Figure 3.4 is that hydrogen ions appear to have a discontinuity in potential and temperature that results in an asymptote in speed. This is an instance in which the dust grain ablated away enough to switch from SL theory to OML theory before fully ablating away. Further analysis of the discontinuity between SL and OML theoretical regimes is provided in Appendix A. The important note here is that this transition often happens when grains get very small, usually due to ablation. Further, the ablation rate

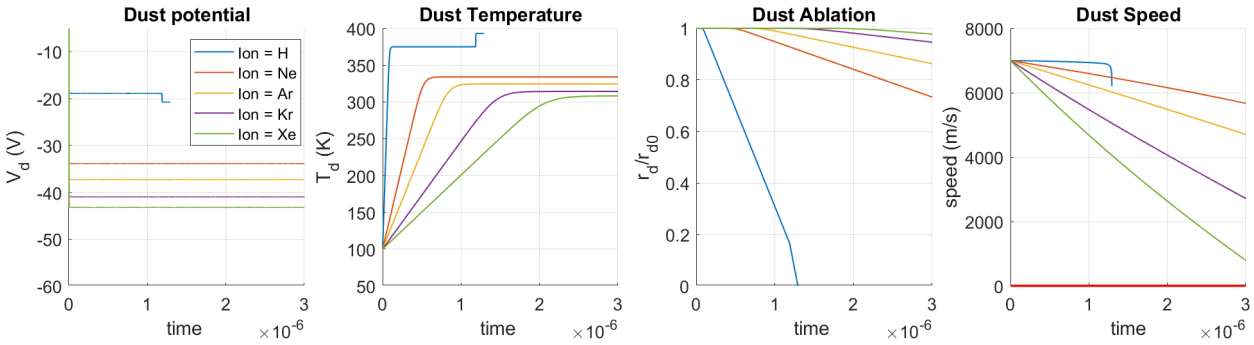

Figure 3.4: Changing the ion mass of the plasma affects the equilibrium values for V_d and T_d. Lighter ions result in higher T_d and more ablation, but less Δv_d. The discontinuity is from transitioning between SL and OML theories.

typically increases in the OML regime.

One of the most influential plasma parameters we can change is the plasma density, as shown in Figure 3.5. Interestingly, the density is low enough in the first two terms that the baseline grain radius is within the OML regime, while the SL regime is used for densities of 10^{21} m^{-3} and above. As we can see, the two theoretical regimes produce different equilibrium potentials, and changes within each regime have varying effects on the other plots. While the less dense plasmas certainly have the lowest influence on dust speed, the denser of the OML regime plasmas, $n_p = 10^{20}$ m^{-3}, gives a larger equilibrium temperature and thus results in more ablation than plasmas with two orders of magnitude more density. Following the math and other results in this thesis, this outcome makes sense, but it seems counterintuitive. Perhaps this is a result of the assumptions breaking down in each model when r_d is near λ_D, as previously discussed.

Aside from the differences resulting from the different theories, the results follow what one would expect. The plasma density influences the heating rate and the equilibrium temperature for a grain, which in turn affects the ablation rate and the drag force. Denser plasmas result in higher temperatures, faster ablation, and greater changes in dust grain

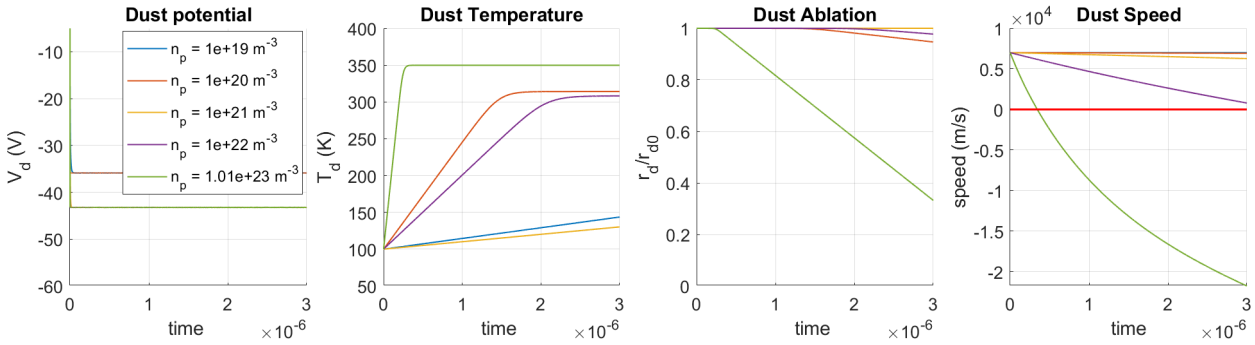

Figure 3.5: Changing the plasma density only affects the equilibrium potential depending on its effect on λ_D and thus the theoretical regime. Generally, denser plasmas have higher temperatures, greater ablation and larger Δv_d.

speed. This parameter has such an effect on the final speed that it is the primary factor used for changing the desired sheet length of the plasma since grains will spend less time in a shorter plasma sheet. Also of note in the Dust Speed graph is that the densest plasma has not only rejected the grain, but is trying to propel the grain to the same speed as the exhausting plasma.

Speaking of plasma speed, Figure 3.6 shows the results of changing the plasma flow speed. Changing this parameter does not influence the equilibrium potential or temperature of the grain, and thus has little affect on the ablation. However, it does have an influence on the final speed of the grains. This indicates that this condition could be changed to either help slow down large particles or reject fewer small particles, and this would also have a sizable effect on the energy needed to produce the plasma.

Closer examination of some additional plasma density and flow velocity plots reveals that in order to obtain approximately the same Δv_d, one could either double the plasma density n_p or multiply the flow speed v_f by about 1.5. Looking back at Equation 2.29, it is obvious that doubling the plasma density would cause much less of an energy increase than increasing the flow speed by 50%. However, as we can see from Figures 3.5 and 3.6, it appears that

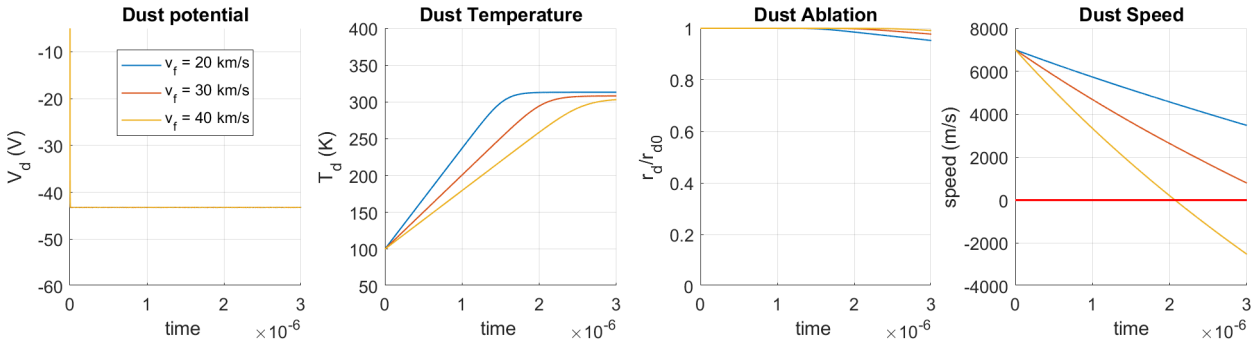

Figure 3.6: Changing the plasma flow speed does not alter equilibrium potential, and has little effect on equilibrium temperature and ablation. It has a much more substantial effect on the overall grain velocity.

increasing flow speed will have little effect on the ablation of the dust grains, while increasing plasma density will certainly have negative impacts on how many grains survive the transit through the plasma sheet.

Overall, these plots indicate that one could use this information to help tune the desired collector for a particular size and velocity of incoming dust grains. Later plots are able to do this more broadly, but these time dependent plots allow for a more detailed look into the physics of the process. For instance, if we were examining $r_{d0} = 1$ μm sized grains for the same length of plasma sheet but at slower initial velocities, we may want to decrease the ion mass, flow speed, or density of the plasma. However, since all these terms are connected, a change in one for the purpose of decreasing velocity may influence another that causes increased ablation. As with all things in engineering, one must choose between different tradeoffs.

3.3 Sheet Length Dependent Plots

Having investigated the physics through the time dependent plots, it is now time to shift focus to looking at this information with respect to the plasma sheet length. These plots take

advantage of the relative position ODE calculated in Equation 2.28 to focus on the effects these parameters have compared to the sheet length, allowing us to account for effects of dust grain deceleration through a finite plasma sheet.

When initially examining these types of graphs, it was found that changes in the plasma density were actually self-similar. (Demonstration of this self-similarity can be seen in Figure 3.7(a).) Thus, to expand the capabilities of these plots, the x-axis is essentially the sheet length multiplied by the plasma density. This allows us to examine fundamentally the effects of changing sheet length, plasma density, and the parameter in question for each graph. Additionally, since we are now shifting focus to designing the plasma for an actual collector, we are more interested in the final velocity of a grain, so we are only looking at dust velocity on the y-axis and ignoring potential, heating, and ablation.

As with the time dependent figures, it is important to establish a common baseline of input values to act as our constant from which we will vary individual parameters. For these plots, the baseline characteristics used are plasma density $n_p = 10^{22}\text{m}^{-3}$, plasma temperature $T_p = 10$ eV, ion mass $m_i = 131.29$ amu (that of Xenon), flow speed $v_f = 30km/s$, initial dust size $r_{d0} = 1$ μm, initial dust velocity $v_{d0} = -7000$ m/s, initial dust temperature $T_{d0} = 100$ K, and initial dust potential $V_{d0} = -5$ V.

Likewise, as discussed in the previous section, changing the initial dust potential relative to the plasma has no effect on the outcome and thus examination of this plot is omitted. Similarly, changing the initial dust temperature has little effect, and this plot is included in Appendix A.

As previously mentioned, the Plasma Density Dependence, as shown in Figure 3.7(a), shows the self-similarity between changes in plasma density n_p with respect to sheet length. Though it is difficult to see in this plot, examination reveals that these outputs are not exactly the same and do exhibit some minor but insignificant fluctuations. Since there is no adjustment to the time scale or full ablation of the grain, the plotted outputs do not end at the same point. However, by dividing by the respective density values, we observe that most of the plotted lines end a bit over the 5 cm sheet length value. Therefore, this graph indicates

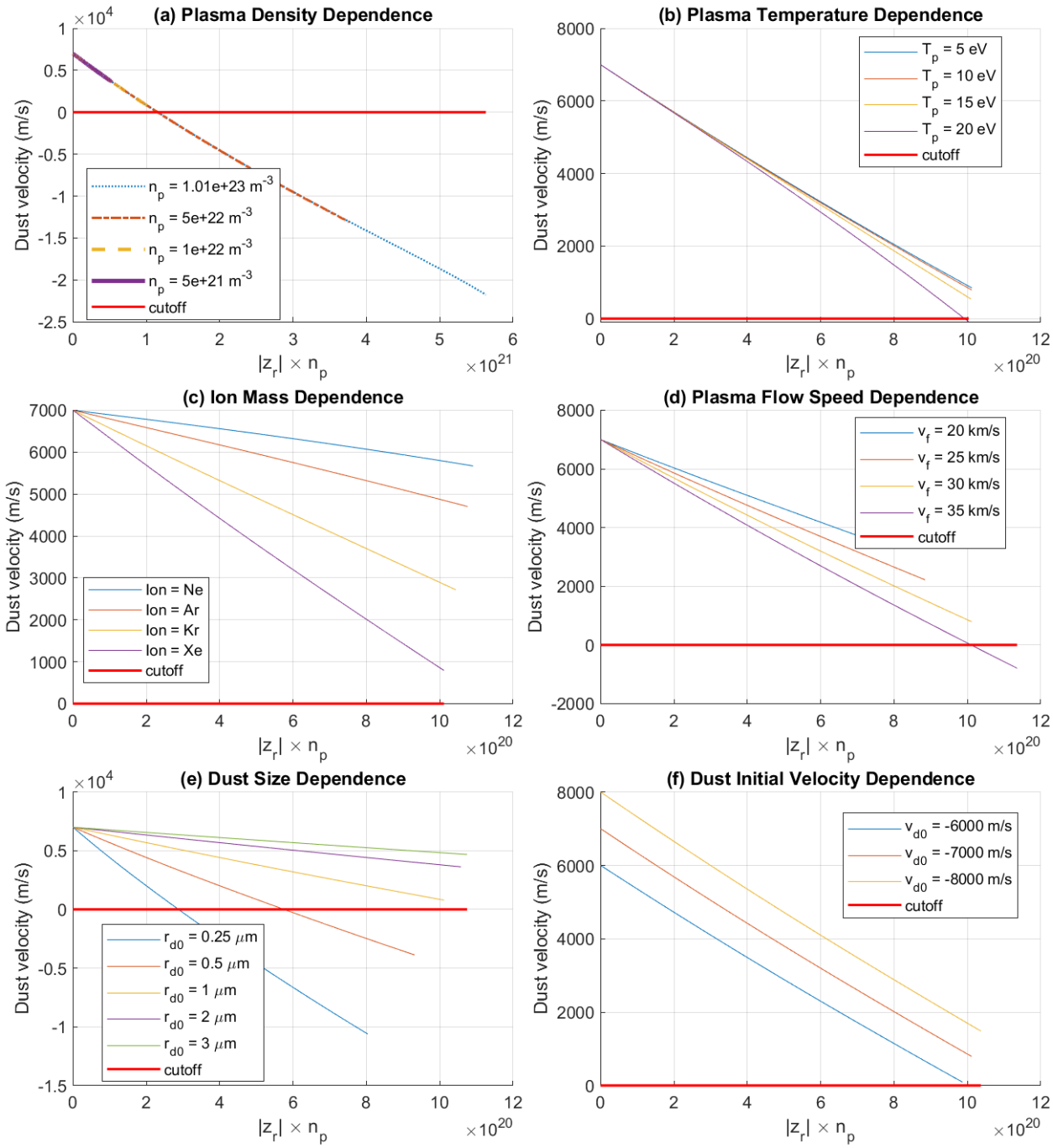

Figure 3.7: Effects on dust grain velocity from changing various plasma and grain parameters. The x-axis gives the sheet length times the plasma density, enabling examination of both factors to some extent. The magnitude of z_r is used due to quirks in the model described elsewhere. Note that (a) has a different x-axis magnitude than the other plots.

that for approximately the same time period, a dust grain will pass through similar lengths of plasma no matter the density, but the final velocity of that grain will change drastically with varying plasma densities. this graph in particular is useful in selecting a relevant plasma density for the desired length of a plasma sheet, though it can only account for one grain radius.

The Plasma Temperature Dependence, as presented in Figure 3.7(b), is reminiscent of the Dust Speed graph in Figure 3.3, which is unsurprising. Because of this similarity, it is inferred that the dust equilibrium temperatures and ablation rates follow similar patterns as before. Therefore, we know that there is very little ablation when T_p = 5 - 10 eV, and greater ablation rates at T_p increases. Notably, the output for $T_p = 20$ eV is slightly concaved downward, indicating that the dust grain is ablating at a more rapid rate. If these trends were to continue, the $T_p = 20$ eV line would soon hit an asymptote as the grain fully ablates. Due to the layout of the axes, we can also say that this behavior will not change for incremental combined changes of density and sheet length.

The Ion Mass Dependence, given in Figure 3.7(c), also shows a similar story to the time dependent plots in that we observe greater velocity changes for increasing ion mass, all else being equal. Since the time span of analysis does not change, a plot line with a larger final sheet length indicates that the dust grain traveled faster relative to the plasma through the same length of plasma sheet. In this case, this faster relative speed can be explained by the fact that collisional drag force is weaker for lighter plasmas, which corresponds to previous observations.

Moving to the Plasma Flow Speed Dependence graph in Figure 3.7(d), we observe an even greater difference in the final length value for each of the outputs. In the previous graph, this indicated a weaker force, but that cannot be the case here since the longer output lines also experience greater deceleration. Rather, because length of these lines correspond to the relative speed of the dust grain and the plasma, it is obvious that this relative speed will be greater as the flow speed of the plasma itself is increased, resulting in longer interaction lengths for a given time. As before, the nature of the x-axis also indicates that this behaviour

will be extremely similar for joint changes in sheet length and plasma density.

Observing the Dust Size Dependence plot in Figure 3.7(e) provides greater insight as to what will happen to differing population sizes of grains in a flyby. As before, we observe that dust grains under a certain size will be rejected, but we can now see how that changes with varying length and density of the plasma sheet. Intuitively, a shorter sheet length will reject fewer small particles, but will not provide much Δv_d to larger ones. Looking again at the values for final sheet length for a constant time span, we recognize that the larger, heavier grains pass through the plasma sheet more quickly than the smaller grains, which are affected more by the drag force due to their high surface area to volume ratio.

Figure 3.7(f), the Dust Initial Velocity Dependence plot, also gives an indication for various flyby conditions the spacecraft might encounter, though these can be manipulated based on overall mission design for the plume encounters. As expected, changing these values simply shifts the velocity curve vertically, with initially faster relative speeds passing through the plasma sheet more quickly than initially slower grains.

Overall, these plots are a great stepping stone for examining many effects at once. They enable us to see how one could change the plasma parameters to design a collector targeted for a particular grain size and speed, and provide incredible insight into the relation of plasma density and sheet width. The next step would ideally allow a mission planner to easily and practically design a system based on a variety of initial speeds and sizes as well as desired final states. To this end, we now examine contour plots for final dust grain radius and velocity based on initial size and speed that can be used for this purpose.

3.4 Contour Plots

In order to build useful radius and velocity contour plots, it is important to first understand the initial range of sizes and speeds the collector will encounter as well as the desired final states for these properties. It was mentioned previously that complex molecules cannot survive hypervelocity impacts on the scale of Cassini flyby speeds, but at what speed does molecular survival become likely, and does the size of the ice grain affect this value?

As we have previously established, we assume the population of the ice grain sizes and their relative densities to follow a differential size distribution $dN/dr \propto r^{-q}$ where q changes depending on the altitude [37]. This model was primarily based on data from Cassini's Imaging Science Subsystem, but is bolstered by in situ measurements from instruments such as the Cassini Plasma Spectrometer and the Radio and Plasma Wave Spectrometer Langmuir Probe [8]. Such a relationship was even expected to be the case after early analysis of initial passes [46]. For the purposes of this study, we will examine an initial range of sizes between a minimum of $r_d = 0.01$ μm (with smaller particles regarded as vaporous) and a maximum of $r_d = 3$ μm (with larger particles being rare at or above 50 km) [37] [33].

To obtain an initial idea of our possible range of flyby velocities, we first consider the general pass speeds for moon-centric orbital missions and for planet-centric flyby missions. Europa has an escape velocity of 2.0 km/s, so slower passes over the target will likely need to be orbital, and faster passes will be flybys in a Jovian-centric orbit [55]. Trajectory design for the Europa Clipper mission indicates that the latter type of pass would occur at velocities near 4.5 km/s [6]. Theoretically, this could likely be lowered further, but radiation considerations around Jupiter, among other factors, limit these options. At Enceladus, escape velocity is only 0.24 km/s, so orbital missions would be very slow [11], and Cassini flyby speeds ranged from $\approx$ 7 km/s up to $\approx$ 18 km/s [36] [13]. These flyby speeds can easily be reduced to $\approx$ 4 - 5 km/s for a more dedicated mission, and have the potential to be reduced to $\approx$ 2 km/s using flybys of other moons or additional fuel, but these increase mission complexity or fuel mass, respectively, and both incur cost penalties [48]. In this study, we examine a range of flyby speeds from $v_{d0} = 1.0$ to 10.0 km/s in order to get a broader idea of the concept's capabilities. Slower velocities would not require such a system, and faster ones would require unrealistic plasma parameters.

Having set limits for the initial radius and velocity ranges, we must also consider desired final states. In 2001, laboratory analysis revealed that it was possible for bacteria and fungal spores to survive impacts of 5.1 ± 0.1 km/s, but at a very low survival rate [21]. NASA's Stardust mission also recovered some small organic molecules at a speed of 6.1 km/s, though

at unknown organic capture efficiencies [16] [10]. For similar sample return missions, studies indicate that 2 km/s impacts into aerogels is ideal, though aerogel capture prohibits extensive on-board analysis by the spacecraft [48]. More recent experiments have shown survival rates up to 44% for organic molecules in ice impacting natural barriers such as sand, water, and crushed ice at speeds near 2 km/s [7].

In early 2020, New et al. used micron-size polymethylmethacrylate (PMMA) particles as an ice grain stand-in (due to its similar material properties and complex molecular makeup) and tested radii of $r_d = 2$, 3, and 5 μm at velocities of about $v_{d0} = 0.5$, 1, 2, and 3 km/s against various metallic targets. They found that the optimal target material was a soft metal such as gold or indium, and the optimal speed for capture of $r_d = 2$ - 3 μm grains was about 1 km/s [33]. At that speed and below, particles deformed but did not deteriorate detrimentally, and capture efficiency was still high; however, at speeds around 2 - 3 km/s the organic molecules remained intact, but the particles themselves experienced extreme deterioration and only left a small residue on the capture plate [33]. A similar group then conducted a complementary analysis using actual water ice grains with dissolved fluorescent complex molecules launched into indium foil and studied impacts of 1.3, 1.7, and 3.1 km/s [34]. They found average organic capture efficiency rates in the range of $\approx$ 10% for impact speeds less than 2 km/s for grains of size $r_d < 5$ μm (with some craters organic capture efficiency as high at 50%). However, efficiency rates were not much higher than background measurements for 3 km/s impacts [34]. A model derived from this data expects capture efficiency rates to be higher for smaller grains, and optimal capture velocity to be slightly larger for smaller sized grains. This later study also observed decreased collection for impacts slower than $\approx$1 km/s and noted that capture efficiencies may be higher for grains at Enceladus, depending on how their formation affects density [34].

From these studies, we see that the organic capture efficiency is different for differently sized ice grains, and there is likely an ideal capture velocity for a grain of a particular size and density [33] [34]. For the purposes of this study, we ignore these complexities and assume capture efficiency is the same for grains with different radii, and we are thus equally interested

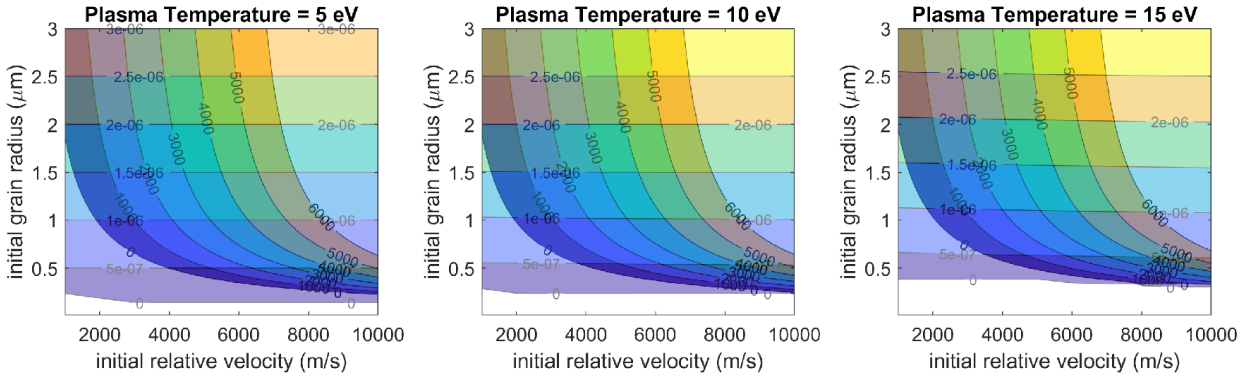

Figure 3.8: Contour plots showing the effects of altering plasma temperature on the final radius and speed of dust grains with the displayed initial conditions. Raising T_p increases ablation.

in anything that does not fully ablate. We also observe that a minimum capture speed may exist as well, though this may change in microgravity environments [34]. Importantly, we note that organic material can survive hypervelocity impacts of up to ≈ 6 km/s, though capture efficiencies are likely extremely low at these speeds. All this considered, we will examine final velocities in the contour plots in the range of $v_d = 0$ to 6.0 km/s to understand when organic material may survive, but we will only consider final grain speeds up to 3.0 km/s in the later feasibility analysis.

Now that the limits of the contour plots are established, we can examine how changes to the plasma parameters influence the plots and what that means for the system as a whole. As in the previous sections, it is useful to establish a baseline of parameters as a control that we can then alter one parameter at a time. In this section, our baseline parameters are $n_p = 10^{22}$ m^{-3}, $T_p = 10$ eV, $v_f = 20$ km/s, $T_{d0} = 100$ K, $V_{d0} = -5$ V, and a desired plasma sheet length $L_p = 5$ cm. The initial radii and velocities follow what was just established in previous paragraphs.

We begin by investigating the effects of changing the plasma temperature T_p as shown in Figure 3.8. The main contribution of increasing T_p is somewhat increasing ablation.

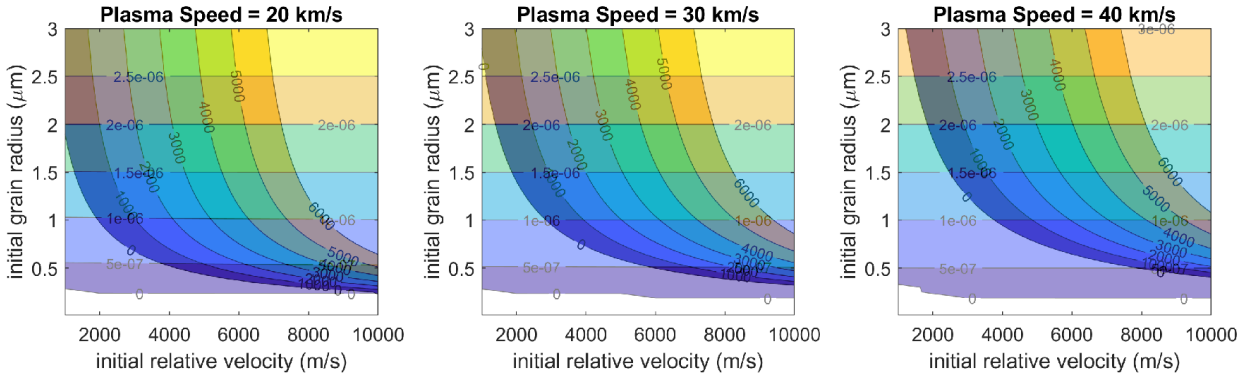

Figure 3.9: Contour plots showing the effects of changing plasma flow speed on the final radius and speed of dust grains with the displayed initial conditions. Dust grains feel larger forces for faster plasmas.

Since the plotted values are much more dependent on the length of the plasma sheet, one way to determine ablation severity is by looking at the slope and placement of the radius contours. More rapid ablation of the ice grains is symbolized by an increased slope and higher placement of these contours in the graph. Searching for these changes in the radius contours, we can see that ablation slightly intensifies for higher temperature plasmas.

Decreasing temperature would be good for the energy considerations of the plasma, and we see in Figure 3.8 that this will slightly help with ablation as well. However, as previously mentioned, this would also decrease the ion thermal speed, which would strain the assumptions of SL theory unless other parameters are also changed.

Figure 3.9 examines the effects of altering the plasma flow speed v_f. Increasing v_f does not appear to significantly alter ablation rates for this plasma baseline, but it does shift the velocity contours up and to the right while decreasing the knee in those curves. These graphical changes indicate a greater drag force felt by the dust grain for faster flowing plasmas. Since the zero velocity contour is shifting but the radius contours are not, we can conclude that a larger portion of smaller grains are being rejected by faster plasma sheets. That is, their velocity is reversed, and they are not being collected even though they do not

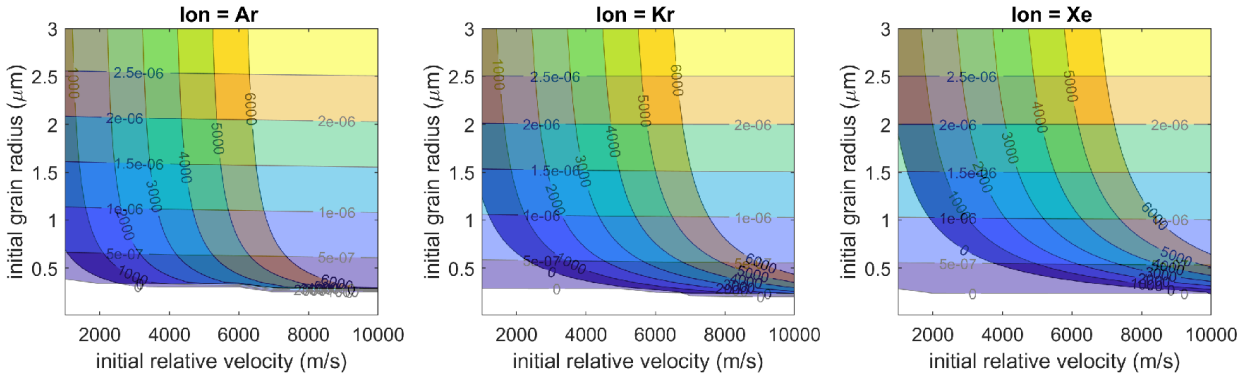

Figure 3.10: Contour plots showing the effects of adjusting ion mass on the final radius and speed of dust grains with the displayed initial conditions. Lighter plasmas have increased ablation yet lower drag forces.

fully ablate. As seen previously, this can be used for targeting certain grain sizes if desired. Due to the nature of kinetic energy, plasma flow velocity is a squared term, and altering it will drastically influence the energy of the plasma.

Examining the effects of changing the ion mass of the plasma, as seen in Figure 3.10, we observe a similar graphical trend as in Figure 3.9. The velocity contours are shifted up and right and the knee in the curves decreases in severity as ion mass increases. We therefore know that heavier ions generally result in greater drag force on the grains, at least for SL theory, and this supports findings in previous sections. Here the compressing of the tail of the velocity contours is much more pronounced. If we were to examine the final velocity distribution for all the grains at one initial velocity, we would see that as ion mass decreases and the tail compresses, the range of sizes within the ideal capture speed bounds also shrinks. This is undesirable since we want to capture more grains in a wider distribution. However, heavier plasmas also reject more of the smaller grains, so this is yet another tradeoff. We can also see from the slope of the radius contours that lighter plasmas have more aggressive ablation rates. Though this is counterintuitive, it is supported by the previous sections.

Investigating Figure 3.11, we can see that many of the effects observed in the other

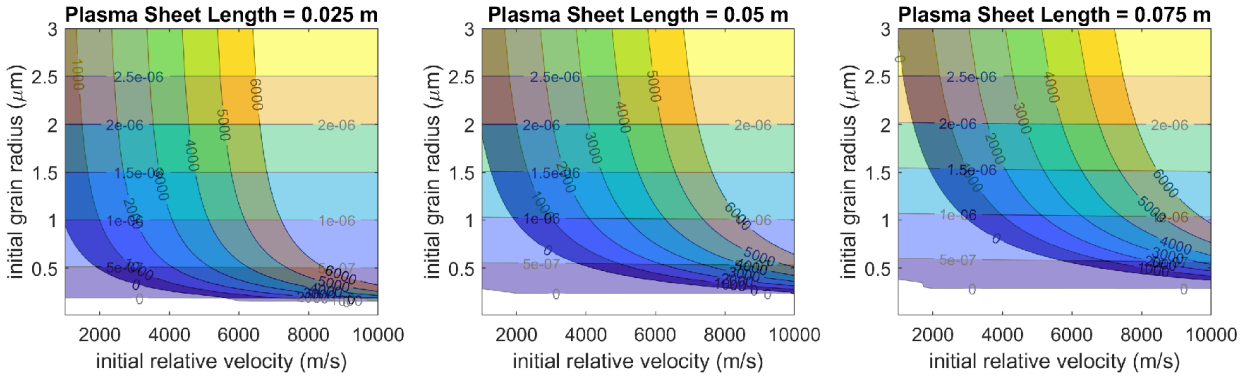

Figure 3.11: Contour plots showing the effects of enlarging plasma sheet length on the final radius and speed of dust grains with the displayed initial conditions. Thicker sheets result in increased ablation and larger drag forces.

contour plots are also present here. One would expect that a longer plasma sheet would result in more drag force felt by the grain as well as greater overall ablation. Examining Figure 3.11 reveals that the velocity contours shift precisely as expected and the lower limit for fully ablated grains increases as well. The slopes of the radius contours also increase with greater sheet length, though this is more difficult to discern, suggesting that the change in ablation is less drastic than the change in drag force.

The final three contour plots given by Figure 3.12 demonstrate the effects of changing the plasma density. Suspiciously, these plots look very similar to Figure 3.11, but rest assured there is no mistake. This resemblance is due in part to the fact that the smaller and larger values in each figure vary by 50% of the center baseline value. Aside from that, the parallels between these plots indicate that either value could be changed to achieve a similarly desired result. For instance, a long, lower density plasma sheet might be easier to create than a short, dense sheet, or vice versa, and there would be little difference in outcome as long as the two parameters were changed by the same percentages.

An important note is that in all these figures, we find ablation to be approximately linear across the range of dust sizes. Though this is less true for smaller grains, the assumption is

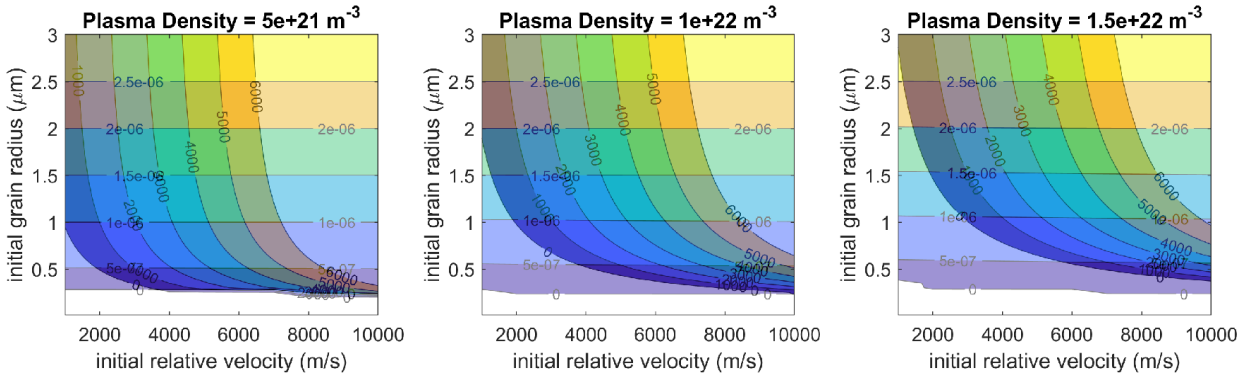

Figure 3.12: Contour plots showing how changing plasma density alters the final radius and speed of dust grains with the displayed initial conditions. Raising n_p increases both ablation and the effective drag force.

still held to adequately enough to be able to say that the overall size distribution simply shifts to the left after passing through the plasma sheet. This assumption allows the simplification of the dust collection analysis that must be done to obtain the mass collected in one pass m_c as in Equation 2.32.

Chapter 4

DISCUSSION OF MERITS AND FEASIBILITY

After analyzing all the figures presented in the last chapter and conducting additional analysis of the required energy and collected mass, the final design will use a plasma density $n_p = 10^{22}$ m^{-3}, plasma temperature $T_p = 10$ eV, a Xenon propellant with ion mass $m_i = 131.29$ amu, flow velocity $v_f = 20$ km/s, and a plasma sheet length $L_p = 2.5$ cm. This assumes the initial temperature of the dust grains is $T_{d0} = 100$ K and the initial potential relative to the plasma is $V_{d0} = -5$ V. In order to more easily compare this design to other proposals, the area of the collector is 10 cm^2.

4.1 Feasibility

The most important first order assessment of the feasibility of this system is the energy required to generate the proposed plasma. As seen in Equations 2.29 and 2.30, the overall energy of the plasma sheet is proportional to the ion mass, plasma density, plasma temperature, and plasma sheet length as well as the square of the flow velocity and the square of the radius of the plasma. These squared terms have great influence over the energy, so it was important to keep them as low as possible.

Since the collected mass is also dependent on the square of the plasma radius, lowering this dimension of the collector is detrimental for collected mass, but great for lowering the required energy. A radius of approximately $r_p \approx 1.78$ cm gives a collector area of 10 cm^2, which allows us to easily compare our proposal to other Enceladus collector concepts [29]. The decided lower limit for plasma flow velocity was governed by the output of the model itself. Lowering the flow speed just a few km/s less than 20 resulted in erroneous outputs for higher initial velocities in the contour plots using the baseline values, so 20 km/s was

therefore accepted as a reasonable value.

Having lowered these more influential properties to reasonable levels, selecting the other parameters was then a balance between their influence on the outputs and the resulting increase in energy. The most important of these was choosing the heaviest reasonable ion mass in order to spread out the final velocity distribution and collect as many grains as possible in our velocity window. Since this study primarily considers noble gases, Xenon was the obvious choice. With flow speed and ion mass thus decided, we chose a plasma temperature of 10 eV in order to keep the assumptions for SL theory as accurate as possible, even though lowering this value would have been energetically beneficial without many other discernible changes in the output. From here, we decided upon a shorter sheet length of 2.5 cm and a plasma density of 10^{22} m^{-3}. It was reasoned that a shorter, denser plasma sheet may be easier to engineer than a longer, less dense one.

These parameters result in an energy per pulse of 11.9 J, which aligns nicely with many PPTs that have been designed over the years. Global reviews of PPT development show that these thrusters typically have energies in the range of 2 - 100 J per pulse, with many in the 10s of J range [40] [32], so this design's energy requirements per pulse seem perfectly reasonable. Another consideration for the viability of this proposed system is the type of propellant. Fortunately, some investigations into low energy (2 - 6 J) gas-fed PPTs have used Xenon and Argon propellants, though these had issues with the fast-acting valves required to operate at high efficiencies [40]. Since the desired effects depend on ion mass specifically, a noble gas propellant is not strictly required. In fact, the heaviest ion mass used in an experiment was in a liquid-fed PPT developed by the Royal Aerospace Establishment in the early 1970s that used liquid mercury as the propellant and operated at 13.1 J per pulse [40]. This method also took advantage of electrostatic forces in their pump design which allowed them to have fewer moving parts, increasing reliability. Development of such a system would likely be key for achieving ideal results for the system proposed in this thesis.

One final design consideration is the frequency at which the PPT will need to operate in order to keep up with the incoming dust particles. These calculations are later discussed in

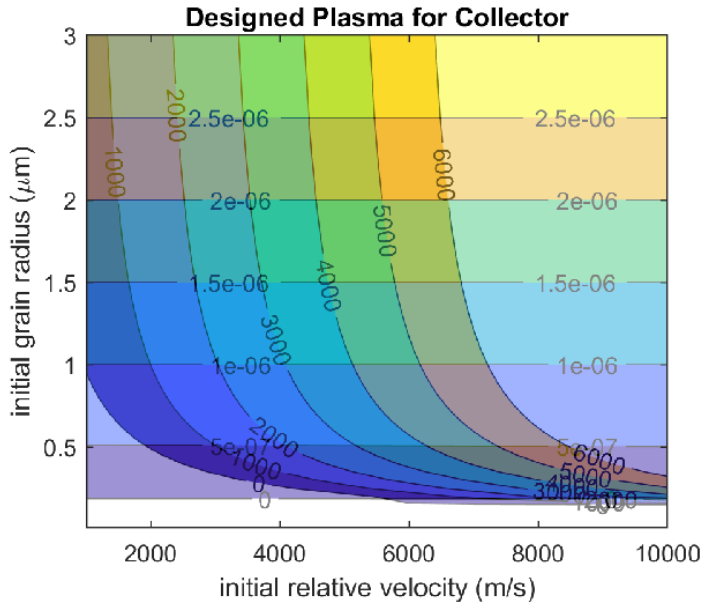

Figure 4.1: Contour plots showing the final radius and speed of dust grains of various initial radii and speeds for the final design plasma parameters.

more detail, but for a 50 km pass altitude, the rate of incoming dust particles larger than 1.5 μm ranges from 50 Hz to 1.5 kHz. This metric is not totally unreasonable, as the gas-fed PPTs mentioned previously operated at frequencies up to 4 kHz [40]. However, this would indicate that the power required for such a system would need to be much higher than for typical PPTs, which usually operate at just a few Hz. Other feasibility considerations are the density, temperature, and length of the plasma sheet. We will omit these considerations for now and assume that this energy calculation of 11.9 J per pulse accounts for these other parameters as a first approximation. Additional work is needed to determine if a system with such parameters could actually be designed.

To better understand how these chosen plasma parameters affect the dust grains and influence the amount of mass collected by the system, a final contour plot was generated and is presented in Figure 4.1. From the radius contours, it is obvious that our chosen parameters result in practically no ablation effects, except for the smallest grains. Although

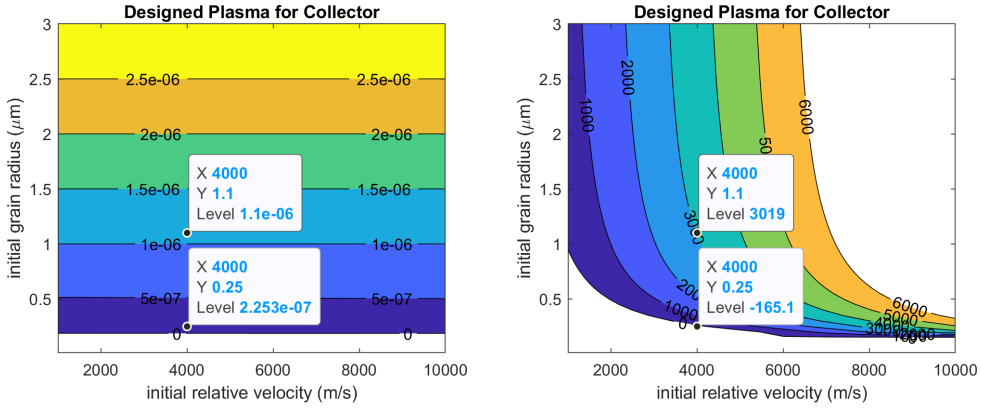

Figure 4.2: The same contours from Figure 4.1 on separate plots with marked points used to estimate Δr_d as well as r^*_{d1} and r^*_{d2}.

this is expected based on our findings in the previous chapter, it is still notable that these ice grains experience virtually negligible amounts of vaporization while interacting with the plasma. We also note that the knee in the velocity contours is slightly sharper than desired, but there is still sufficient spread in the velocity distribution to collect a good amount of material.

In order to properly account for the collected mass as discussed in Section 2.6, we must first choose an initial velocity for the grains. Mission designers have established that about 4 km/s is a reasonably attainable flyby velocity for both Enceladus and Europa missions [48] [6], and we have shown that organic capture efficiency is negatively impacted at collision speeds of 3 km/s and above [33] [34]. Therefore, we will use an initial velocity of 4000 m/s to investigate the mass collected by our proposed system for grains whose final speeds fall between 0 and 3000 m/s.

First, we establish the value for Δr_d, which tells us how much the initial size distribution shifts due to ablation effects from the plasma interaction. With the exception of the absolutely smallest grains, ablation effects were negligible for the chosen parameters, so $\Delta r_d = 0$ for this case.

Next, we establish values for r^*_{d1} and r^*_{d2}, which are governed by the final values for the radius at the maximum and minimum capture velocities. Since we established that there are negligible ablation effects, we can assume that the final radius is equivalent to the initial radius in this case. Here, we find that $r^*_{d1} \approx 0.25$ μm when the final velocity equals zero and $r^*_{d2} \approx 1.1$ μm when final velocity is 3000 m/s, as seen in Figure 4.2.

These values can then be input into Equation 2.32 along with the value for C determined in Equation 2.31 to determine the mass collected in a single pass. Because the output of the plume varies over time [37], and the value for C is dependent on that variable state, these equations can be run multiple times in order to obtain maximum and minimum mass collection values. Accounting for our assumptions and parameters as well as a flyby altitude of 50 km, the maximum collected mass per pass was $m_c = 0.53$ μg and the minimum was $m_c = 0.045$ μg when the plasma sheet was present. For comparison, the same techniques were used to calculate the total mass available for collection in a single pass, and these values ranged from a maximum of $m_c = 6.2$ μg to a minimum $m_c = 0.5$ μg. This indicates that if every grain interacts with the plasma sheet, we will only collect about 10% of the available mass in a pass. However, we will also slow these incoming grains to much more reasonable impact velocities, increasing the organic capture efficiency of those grains. Therefore, while this system would hinder ice collection at lower flyby speeds, it may increase the overall organic capture efficiency for faster passes.

It should be noted here that we assume the plume is symmetric with circular cross sections [37], an idea supported by studying vaporous molecule plume measurements [36], but this is likely not completely accurate due to the complexities of numerous vents along the tiger stripes and electrodynamic forces on the charged grains within the plume [22] [8]. We also assume that the probe is flying directly through the center of this circular plume, which would give the maximum yield for all conditions. Achieving this will be more difficult for planet-centric missions than it will be for moon-centric missions, so the maximum and minimum values for m_c presented here will likely be lower on average.

Another calculation to consider here is that of the rate at which dust grains impact the

sensor. The rates of 50 - 1500 particles per second mentioned previously were for particles larger than $r_d = 1.5$ μm, but we now see that the incoming particle size we are concerned with is around $r_d = 0.25$ μm and larger. As one would expect, the impact frequency increases as smaller particles are considered. In fact, this frequency increases by approximately an order of magnitude to between 400 Hz and 14 kHz. At the high end, this is far greater than the 4 kHz frequencies utilized by previous gas-fed PPT experiments and indicates that a pulsed system might not be practical for this application. In fact, PPTs that rely on capacitive discharge – which is the majority of PPTs – are limited in their maximum frequency by the discharge delay time of the capacitors and the plasma discharge time of the PPT itself. These times are typically on the order of 50 μs or less, thus high operation rates of 10 kHz or greater will require specifically designed power processing units [19].

That being said, for the particle densities we expect to encounter for a 50 km flyby, it is quite possible that one pulse will interact with several incoming ice grains, depending on the total length of travel and survival time of the plasma sheet itself. Thus, while operating at a lower frequency obviously will not slow all the incoming grains, it will likely slow more than one grain per pulse on average. Therefore this issue is not quite as terrible as it first seems. It may also be beneficial to redesign the plasma parameters to target only larger grains, which impact much less frequently. Further, for high velocity flybys, a system that slows at least some particles to reasonable impact speeds will likely collect more organic material overall than a system without the plasma buffer. Additional research is needed to determine in which cases it would be better to have the plasma system as compared to a plain collector, but pulse rates do not totally prohibit this system from being useful.

Another consideration dependent on the pulse rate of the system is the required power and power storage necessary for the system to operate. If we assume a maximum rate of 4 kHz – that of the gas-fed PPT from earlier – our 11.9 J per pulse would result in a power output of 47.6 kW. At 4 km/s and a pass length of 92 km for the maximum plume output (as found in Table 2.1), a flyby would take 23 seconds, and the powerbank required for this system would thereby have to be 300 Wh in order to full accomplish one pass. Further, PPTs

rarely achieve greater than 20% power efficiency, further increasing power requirements. This system would thus require a massive power processing unit just to operate the plasma buffer for our collector, and this factor would likely constrain its use on an actual spacecraft [32]. Because of this factor, the thruster frequency would need to be decreased further. This would increase the practicality of including this system on a mission, but would also reduce the number of incoming grains slowed to capture velocities. Again, we leave further analysis of practical use cases to future investigations.

Overall, it appears that the system as designed in this chapter might be physically possible, but designing such a system would be technically challenging, and it may have specific and limited use cases even then. Further investigation is needed to determine the degree to which this system would actually increase the organic capture efficiency in those cases, as this would determine whether or not this idea should be pursued further.

4.2 Design Comparison

One promising proposal that also seeks to search for life in the plumes of Enceladus is the Enceladus Organic Analyzer (EOA) proposed by the Berkeley Space Science Laboratory [29]. Their detector also uses a 10 cm^2 capture system composed of a tilted louver front plate and solid back plate made of a soft aluminum alloy and is designed to capture ice grains with radii between $r_d = 0.5$ to 3.0 μm at speeds ranging from $v_{d0} = 0.2$ to 5.0 km/s. As previously discussed, collision speeds at or above 3.0 km/s drastically reduce the organic capture efficiency of a system [33] [34] [7]. While some organic material may still be recovered at higher velocities, it will take much more material to have a chance of reaching detectable concentration levels.

EOA also uses a state of the art concentration-based detection method rather than a mass-based method, which enables detection of molecules of interest at the part per billion concentration range for micro-to-nanogram samples, though they admit that a detection level of one part per million is more reasonable for feasibility studies [29]. Unfortunately, the use of plain water will not allow the direct detection of captured bacteria or other microbes since

these microorganisms have adapted for a salty environment and will experience cell lysis in the solution. All things considered, this method is still very likely to be used in future ice plume investigation missions.

A full design of the system proposed in this thesis will likely incorporate most of the components used by EOA, especially the concentration-based detection method. Our design would likely swap the soft aluminum alloy with indium, since it was the most effective material found by New et al. in capturing a range of grain sizes at various speeds [33]. The major difference between our system and EOA would be the addition of the PPT in front of the collector and its associated power processing equipment. This study is not concerned with the exact implementation of this design and leaves that factor to future researchers.

The EOA design also assumes an average column density of 3 μL/m^2 at a 50 km altitude and expects to collect 3 μg of ice with a 10 cm^2 collection area [29] [37]. Our calculations are derived from the same source, so we should see similar numbers if we assume no plasma effects. Indeed, we calculate the total column density to be between 0.58 and 6.8 μL/m^2 depending on the output level from the plume, and the corresponding total available mass is between about 0.5 and 6.2 μg. Hence, our values generally agree with the EOA study on both the average column density and the average available mass, though as previously discussed, plasma effects can have a large impact on the values seen by the collector after the plasma sheet.

The amount of organic material present in the ice grains may vary wildly, not only on whether life exists within that ocean to varying capacities, but also on the physics of how water is ejected to produce the plume [37]. Many of the estimates made here are for a less than optimistic average of the possibilities, and we cannot know much more about the practicality of these collectors without knowing more about the creation of the plume itself. That being said, EOA is designed to detect amino acids at the one part per million concentration range, but this is less likely to occur if less than one microgram of ice is captured [29]. If this concentration level is accurate, the system will collect approximately 1 pg of organic molecules for every 1 μg of ice, as long as enough material is collected. The

study presenting EOA also looked at temperature change for dust grains when they impact the collector, but we ignore this here in part because the final speeds and temperatures of our grains after the plasma sheet will be different than their assumptions [29].

Comparing the system designed in this chapter to the EOA, we observe several advantages and disadvantages for each system. The biggest benefit to using the PPT system is the expansion of the operating velocities for the mission. Though EOA claims to be able to operate up to 5.0 km/s, we have repeatedly stated that this will drastically decrease collected organic material to the point where several passes would be required to obtain enough material for a detection [33] [34] [7].

While the PPT system may enable more efficient organic molecule collection within these higher velocity regimes, it is difficult to say how much of an advantage this would offer. As explained in the previous section, mass and power considerations would limit the maximum frequency at which the PPT could operate, but properties not considered here such as the survival time and length of travel of the plasma sheet may mitigate the effects of lower pulse frequency. It may be that the system is easily able to handle the particle influx for an average plume density but unable to interact with all particles when the Enceladus plume is near its maximum output. Even then, at least some of the incoming ice grains will be slowed. For the most optimistic cases where all incoming particles interact with the plasma, the collected mass is roughly 10% of the available mass for the case considered here. This range of $m_c = 0.045 - 0.53$ μg would require multiple passes to achieve the 1 μg of ice required for organic molecule detection. This is not ideal, though it may be possible to improve the collected mass percentage by using different plasma parameters. Further, this small amount of ice still likely represents an increase in collected organic material when compared to non-plasma-decelerated grains impacting the detector at high velocities. The PPT system could also be designed to adjust the plasma parameters and pulse frequency for each pass in order to maximize the collected mass based on the expected state of the plume.

The EOA also has a number of advantages over the PPT system. First, the entire EOA system has been thoroughly designed, and a prototype has already been tested in some trial

cases. The proposed instrument is only about $16 \times 16 \times 12$ cm with a mass of just 2.5 kg and doesn't require much more power than the 2-3 watts needed to keep it from freezing and the 64 W/hr required during analysis [29]. The PPT system would utilize the majority of these components and would only increase these baseline dimensions. The simplicity, size, mass, and technological readiness level of the EOA make it the obvious choice for any dedicated mission to study Enceladus, though impact velocity considerations may force mission designers to spend time or fuel in reducing flyby speeds.

Chapter 5

CONCLUSION

Now nearing the end, it is important to include a brief review of everything in the last 60 or so pages. At the beginning of this thesis, we established that NASA is seeking new technologies that will enable new forms of sample collection from the plumes of icy ocean worlds across the solar system [1]. While there are potentially several moons to choose from, we have detailed data about Enceladus, so this study has primarily focused its attention there. Since PPTs are typically easy to implement and have extensive flight heritage, they were chosen as our desired method for accomplishing NASA's goal.

A model based on work from Ticoş et al. was then adapted and presented along with all of its assumptions and flaws. This model was used to produce time-dependent plots, length-dependent plots, and contour plots which were explained and examined along the way. These plots allowed us to design a set of parameters for our plasma sheet that would enable collection of a reasonable amount of ice at high speeds and low ablation rates. Examining this design further, we found that it seemed feasible and practical to implement until we accounted for the rate of impinging dust grains. Somewhat ironically, the icy plume has too many particles for our designed system to keep up.

These final sections go into more detail as to the considerations and uses of the proposed system as well as the work that still needs to be done to answer some of the questions brought up throughout the thesis. Contemplating once more the question we set out to answer, it is safe to say that a PPT could certainly be used to slow incoming ice grains to reasonable speeds, though designing such a system will not be as simple as adapting an available PPT design to operate in front of a collection plate. Work still needs to be done to satisfactorily answer this question, but these results have some promise.

5.1 Proposal Conclusions

Considering again the feasibility and practicality of the PPT-integrated ice grain collection system as proposed in Chapter 4, it appears obvious to this author that this idea is, at best, over-engineered for a mission to Enceladus. If NASA were to design a dedicated Enceladus flyby or orbital mission within the next several years, a system such as the EOA is the obvious choice. Such a mission could easily be designed, and much work has already been done on how to adequately decrease the velocity of the spacecraft and how this would affect the payload mass, mission cost, and other considerations [48].

However, a major factor that was ignored for most of this paper is that NASA may also want to design a similar mission for Europa or other icy worlds. Since Europa is much more massive than Enceladus, flyby velocities are inherently faster [11] [6]. Therefore, the PPT system could be extremely useful for plume investigation at Europa since such a system may be more effective at collecting organic material at higher velocities. In fact, it may be necessary to slow incoming particles to mitigate the detrimental effects of ultra hypervelocity impacts, though more research is needed to determine the comparative organic capture efficiencies for each method. Greater understanding of the plume characteristics at Europa would also be necessary for that investigation.

Overall, the greatest advantage that the proposed PPT system offers is flexibility in mission design, and its greatest disadvantage lies in the power, system mass, and technological readiness of a high frequency PPT. If a space agency ever wants to design a successor to Cassini at Saturn or Jupiter – a generalist spacecraft that could conduct analysis of the planet itself and all of the surrounding moons – this system could enable easier collection of geyser plume particles without having to design the mission around the flyby velocity requirements. Maybe the plasma buffer device could even be used as a propulsion mechanism when not collecting ice grains. Without more research, it is difficult to know if such a system could be designed in a way that did not make it the primary payload of the spacecraft rather than one scientific instrument of many.

5.2 Future Work

Throughout this thesis, there have been a number of branching paths proffered for future investigators to explore. To give some structure, we will start by looking at the broader work that needs to be done to enable development of this PPT system. We will then narrow in on some more specific items that will enhance fundamental understanding.

As discussed in recent sections, investigation is needed to determine what pulse frequencies would enable reasonable power levels and power storage for such a mission. Perhaps such research will find that an altogether different type of plasma engine is more suitable for the job. In any case, this will enable more accurate comparisons to cases where a plasma buffer is unavailable. On that note, greater understanding of the plume characteristics at Europa is essential. Ideally, this branch of future work includes mass considerations of this system to compare to the extra fuel mass needed to slow the spacecraft. Other considerations like time required to slow the craft via gravity assists at other moons make this analysis more complicated, but of greater use to mission designers.

At a more focused level, designing and testing a low-frequency version of this PPT would reveal whether or not the physics developed and assumptions used for this model are accurate. Since the energy per pulse is well within the realm of previously designed PPTs it should be straightforward to develop an experimental setup to examine the plasma drag effects from PPT exhaust on microparticles. Such a setup could use micron sized PMMA particles like those used in Reference [33] as a stand-in for ice grains and observe the particle motion with high speed imagery similar to Reference [52].

Getting to the core of this research, much future work could be done to enhance the accuracy of this model which might possibly alter the results. The most fundamental research to be done in this area is development of the physics that would connect the SL and OML theories and prevent the discontinuity between the two. Investigation into this problem would likely yield a much greater understanding of dusty plasma physics. At a more basic level, it would be relatively straightforward to fill gaps in this model such as incorporating

the equations for the positive voltage regime.

Other possibilities include incorporating a finite plasma sheet or sheet with diffuse edges, including additional forces and charging effects that were assumed to be insignificant, and investigating the chemical reactions that might occur between the grain material and the plasma. Looking into these assumptions and simplifications would certainly produce a more accurate model, but time will likely be better spent on other paths in the forest of knowledge. As with many things in life, the road goes on forever, and the party never ends.

BIBLIOGRAPHY

[1] National Aeronautics and Space Administration. Sample collection for life detection in outer solar system ocean world plumes. `https://www.sbir.gov/sbirsearch/detail/1547819`, February 2019.

[2] J. E. Allen. Probe theory - the orbital motion approach. *Physica Scripta*, 45(5):497, May 1992.

[3] M.J. Baines, I.P. Williams, A.S. Asebiomo, and R.L. Agacy. Resistance to the motion of a small sphere moving through a gas. *Monthly Notices of the Royal Astronomical Society*, 130(1):63–74, July 1965.

[4] Elise R. Boerwinkle. Measurements of the secondary electron emission from dielectric surfaces. Masters thesis, Texas Tech University, December 1988.

[5] H. Bruining. *Physics and Applications of Secondary Electron Emission*. McGraw-Hill, NY, 1954.

[6] Brent Buffington. Trajectory design for the europa clipper mission. In *AIAA/AAS Astrodynamics Specialist Conference*. American Institute of Aeronautics and Astronautics, August 2014.

[7] Mark J. Burchell, Stephen A. Bowden, Michael Cole, Mark C. Price, and John Parnell. Survival of organic materials in hypervelocity impacts of ice on sand, ice, and water in the laboratory. *Astrobiology*, 14(6):473–485, June 2014.

[8] Y. Dong, T. W. Hill, and S. Y. Ye. Characteristics of ice grains in the enceladus plume from cassini observations. *Journal of Geophysical Research: Space Physics*, 120(2):915–937, February 2015.

[9] B.T. Draine and E.E. Salpeter. On the physics of dust grains in hot gas. *The Astrophysical Journal*, 231:77–94, July 1979.

[10] Jamie E. Elsila, Daniel P. Glavin, and Jason P. Dworkin. Cometary glycine detected in samples returned by stardust. *Meteoritics and Planetary Science*, 44(9):1323–1330, September 2009.

[11] NASA Science Solar System Exploration. Enceladus in depth: By the numbers. `https://solarsystem.nasa.gov/moons/saturn-moons/enceladus/by-the-numbers/`, 2020.

[12] Cassini Imaging Central Laboratory for Operations. Enceladus rev 61 flyby: Mar 12 '08. `http://ciclops.org/view.php?id=4806&js=1`, 2008.

[13] Cassini Imaging Central Laboratory for Operations. Enceladus rev 80 flyby: Aug 11 '08. `http://ciclops.org/view.php?id=5156`, 2008.

[14] Cassini Imaging Central Laboratory for Operations. Enceladus rev 91 flyby: Oct 31 '08. `http://ciclops.org/view.php?id=5335`, 2008.

[15] Gabriel Giono, Lorenz Roth, Nickolay Ivchenko, Joachim Saur, Kurt Retherford, Stephan Schlegel, Marcus Ackland, and Darrell Strobel. An analysis of the statistics and systematics of limb anomaly detections in hst/stis transit images of europa. *The Astronomical Journal*, 159(4):155, March 2020.

[16] Daniel P. Glavin, Jason P. Dworkin, and Scott A. Sandford. Detection of cometary amines in samples returned by stardust. *Meteoritics and Planetary Science*, 43(1-2):399–413, February 2008.

[17] M. Hirt, D. Block, and A. Piel. Measurement of the ion drag force on free falling microspheres in a plasma. *Physics of Plasmas*, 11(12):5690, November 2004.

[18] M. Hirt, D. Block, and A. Piel. Measurements of the ion drag force on micrometer sized particles in the double plasma device dodo. *IEEE*, 32(2):582–585, June 2004.

[19] Tiankun Huang, Zhiwen Wu, Xiangyang Liu, Kan Xie, Ningfei Wang, and Yue Cheng. Study of breakdown in an ablative pulsed plasma thruster. *Physics of Plasmas*, 22(10):103511, October 2015.

[20] H. L. F. Huybrighs, E. Roussos, A. Blöcker, N. Krupp, Y. Futaana, S. Barabash, L. Z. Hadid, M. K. G. Holmberg, O. Lomax, and O. Witasse. An active plume eruption on europa during galileo flyby e26 as indicated by energetic proton depletions. *Geophysical Research Letters*, 47(10):e2020GL087806, May 2020.

[21] Mark J.Burchell, Jo Mann, Alan W.Bunch, and Pedro F.B.Brandão. Survivability of bacteria in hypervelocity impact. *Icarus*, 154(2):545–547, December 2001.

[22] G.H. Jones, C.S. Arridge, A.J. Coates, G.R. Lewis, S. Kanani, A. Wellbrock, D.T. Young, F.J. Crary, R.L. Tokar, R.J. Wilson, T.W. Hill, R.E. Johnson, D.G. Mitchell, J. Schmidt, S. Kempf, U. Beckmann, C.T. Russell, Y.D. Jia, M.K. Dougherty, J.H. Waite Jr., and B.A. Magee. Fine jet structure of electrically charged grains in enceladus' plume. *Geophysical Research Letters*, 36(16), August 2009.

[23] J. H. Waite Jr., W. S. Lewis, W. T. Kasprzak, V. G. Anicich, B. P. Block, T. E. Cravens, G. G. Fletcher, W.-H. Ip, J. G. Luhmann, R. L. Mcnutt, H. B. Niemann, J. K. Parejko, J. E. Richards, R. L. Thorpe, E. M. Walter, and R. V. Yelle. The cassini ion and neutral mass spectrometer (inms) investigation. *Space Science Reviews*, 114:113–231, September 2004.

[24] J. Hunter Waite Jr., Michael R. Combi, Wing-Huen Ip, Thomas E. Cravens, Ralph L. McNutt Jr., Wayne Kasprzak, Roger Yelle, Janet Luhmann, Hasso Niemann, David Gell, Brian Magee, Greg Fletcher, Jonathan Lunine, and Wei-Ling Tseng. Cassini ion and neutral mass spectrometer: Enceladus plume composition and structure. *Science*, 311(5766):1419–1422, March 2006.

[25] Paul W. Schumacher Jr., Wesley L. Jackson, and Ryan T. Olson. Exact keplerian relative motion: An elementary formulation of the initial-value problem. In *Advances in the Astronautical Sciences AAS/AIAA Spaceflight Mechanics Meeting 2019*. American Astronomical Society/American Institute of Aeronautics and Astronautics, January 2019.

[26] S. Jurac, R.A. Baragiola, R.E. Johnson, and E.C. Sittler Jr. Charging of ice grains by low-energy plasmas: Application to saturn's e ring. *Journal of Geophysical Research*, 100(A8):14821–14831, 1995.

[27] M. Kretschmer, S. A. Khrapak, S. K. Zhdanov, H. M. Thomas, G. E. Morfill, V. E. Fortov, A. M. Lipaev, V. I. Molotkov, A. I. Ivanov, and M. V. Turin. Force field inside the void in complex plasmas under microgravity conditions. *Physical Review E*, 71(5):056401, May 2005.

[28] D. A. Law, W. H. Steel, B. M. Annaratone, and J. E. Allen. Probe-induced particle circulation in a plasma crystal. *Physical Review Letters*, 80(19):4189, May 1998.

[29] Richard A. Mathies, Md Enayet Razu, Jungkyu Kim, Amanda M. Stockton, Paul Turin, and Anna Butterworth. Feasibility of detecting bioorganic compounds in enceladus plumes with the enceladus organic analyzer. *Astrobiology*, 17(9):902–912, September 2017.

[30] MathWorks. Help center - ode45. `https://www.mathworks.com/help/matlab/ref/ode45.html`, 2020.

[31] T.L. Matskevich and E.G. Mikhailova. Secondary electron emission in ice and anthracene films. *Soviet Physics - Solid State Physics*, 2:655–659, December 1960. Translated from Fizika Tverdogo Tela, Vol. 2, No. 4, pp. 709-715, April 1960.

[32] P. Molina-Cabrera, G. Herdrich, M. Lau, S. Fausolas, T. Schoenherr, and K. Komurasaki. Pulsed plasma thrusters: a worldwide review and long yearned classification. In *32nd International Electric Propulsion Conference*. Electric Rocket Propulsion Society, September 2011.

[33] J. S. New, R. A. Mathies, M. C. Price, M. J. Cole, M. Golozar, V. Spathis, M. J. Burchell, and A. L. Butterworth. Characterizing organic particle impacts on inert metal surfaces: Foundations for capturing organic molecules during hypervelocity transits of enceladus plumes. *Meteoritics and Planetary Science*, 55(3):465–479, February 2020.

[34] James S. New, Bahar Kazemi, Mark C. Price, Mike J. Cole, Vassi Spathis, Richard A. Mathies, and Anna L. Butterworth. Feasibility of enceladus plume biosignature analysis: Successful capture of organic ice particles in hypervelocity impacts. *Meteoritics and Planetary Science*, 55(8), September 2020.

[35] L. Paganini, G. L. Villanueva, L. Roth, A. M. Mandell, T. A. Hurford, K. D. Retherford, and M. J. Mumma. A measurement of water vapour amid a largely quiescent environment on europa. *Nature Astronomy*, 4:266–272, March 2020.

[36] M.E. Perry, B.D. Teolis, D.M. Hurley, B.A. Magee, J.J. Waite, T.G. Brockwell, R.S. Perryman, and R.L. McNutt Jr. Cassini inms measurements of enceladus plume density. *Icarus*, 257:139–162, September 2015.

[37] Carolyn C. Porco, Luke Dones, , and Colin Mitchell. Could it be snowing microbes on enceladus? assessing conditions in its plume and implications for future missions. *Astrobiology*, 17(9):876–901, September 2017.

[38] F. Postberg, N. Khawaja, S. Kempf, J.H. Waite, C. Glein, H.W. Hsu, and R. Srama. Complex organic macromolecular compounds in ice grains from enceladus. In *48th Lunar and Planetary Science Conference*. Lunar and Planetary Institute, March 2017.

[39] S. Ratynskaia, S. Khrapak, A. Zobnin, M. H. Thoma, M. Kretschmer, A. Usachev, V. Yaroshenko, R. A. Quinn, G. E. Morfill, O. Petrov, and V. Fortov. Experimental determination of dust-particle charge in a discharge plasma at elevated pressures. *Physical Review Letters*, 93(8):085001, August 2004.

[40] Abdolrahim Rezaeiha and Tony Schönherr. Review of worldwide activities in liquid-fed pulsed plasma thruster. *Journal of Propulsion and Power*, 30(2):253–264, March 2014.

[41] I. Richterová, Z. Němeček, J. Pavlu, M. Beránek, and J. Šafránková. Modeling the secondary emission yield of salty ice dust grains. *Icarus*, 212(1):367–372, March 2011.

[42] Lorenz Roth, Joachim Saur, Kurt D. Retherford, Darrell F. Strobel, Paul D. Feldman, Melissa A. McGrath, and Francis Nimmo. Transient water vapor at europa's south pole. *Science*, 343(6167):171–174, January 2014.

[43] P.K. Shukla and A.A. Mamun. *Introduction to Dusty Plasma Physics*. Institution of Physics Publishing, 2002.

[44] U. Shumlak and T. Maruo. Plasma plume mass characterization of a mini-pulsed plasma thruster. In *42nd AIAA/ASME/SAE/ASEE Joint Propulsion Conference and Exhibit*. American Institute of Aeronautics and Astronautics, July 2006.

[45] G. Sorasio, D.A. Mendis, and M. Rosenberg. The role of thermionic emission in meteor physics. *Planetary and Space Science*, 49(13):1257–1264, November 2001.

[46] Frank Spahn, Jürgen Schmidt, Nicole Albers, Marcel Hörning, Martin Makuch, Martin Seiß, Sascha Kempf, Ralf Srama, Valeri Dikarev, Stefan Helfert, Georg Moragas-Klostermeyer, Alexander V. Krivov, Miodrag Sremčević, Anthony J. Tuzzolino, Thanasis Economou, and Eberhard Grün. Cassini dust measurements at enceladus and implications for the origin of the e ring. *Science*, 311(5776):1416–1418, March 2006.

[47] W. B. Sparks, K. P. Hand, M. A. McGrath, E. Bergeron, M. Cracraft, and S. E. Deustua. Probing for evidence of plumes on europa with hst/stis. *The Astrophysical Journal*, 829(2):121, September 2016.

[48] John Spencer and Curt Niebur. Mission concept study: Planetary science decadal survey jpl rapid mission architecture enceladus study final report. `https://sites.nationalacademies.org/cs/groups/ssbsite/documents/webpage/ssb_059319.pdf`, April 2010.

[49] P.C. Stangeby. Plasma sheath transmission factors for tokamak edge plasmas. *Physics of Fluids*, 27(3):682–690, March 1984.

[50] Y. Tanaka, A.Yu. Pigarov, R.D Smirnov, S.I. Krasheninnikov, N. Ohno, and Y. Uesugi. Modeling of dust-particle behavior for different materials in plasmas. *Physics of Plasmas*, 14(5), March 2007.

[51] C.M. Ticoş, Z. Wang, G.L Delzanno, and G. Lapenta. Plasma dragged microparticles as a method to measure plasma flows. *Physics of Plasmas*, 13:103501, September 2006.

[52] C.M. Ticoş, Z. Wang, G.A. Wurden, J.L. Kline, D.S. Montgomery, L.A. Dorf, and P.K. Shukla. Experimental demonstration of plasma-drag acceleration of a dust cloud to hypervelocities. *Physical Review Letters*, 100(15):155002, April 2008.

[53] Zhehui Wang, Cătălin M. Ticoş, and Glen A. Wurden. Dust trajectories and diagnostic applications beyond strongly coupled dusty plasmas. *Physics of Plasmas*, 14(10):103701, October 2007.

[54] Zhehui Wang and G. A. Wurden. Hypervelocity dust beam injection for internal magnetic field mapping. *Review of Scientific Instruments*, 74(3):1887, March 2003.

[55] David R. Williams. Solar system small worlds fact sheet. `https://nssdc.gsfc.nasa.gov/planetary/factsheet/galileanfact_table.html`, April 2016.

[56] C. Zafiu, A. Melzer, and A. Piel. Measurement of the ion drag force on falling dust particles and its relation to the void formation in complex (dusty) plasmas. *Physics of Plasmas*, 10(5):1278, April 2003.

Appendix A
ADDITIONAL PLOTS

Figure A.1 shows the effects of changing the initial potential of the dust grain relative to the plasma. In these time-dependent plots, we can see that this change does not alter the results in any meaningful way. This is due to the fact that v_{te} is extremely fast, and electrons will force the potential to an equilibrium value almost instantly. This is true for both SL and OML regimes.

Figure A.2 shows how changing the initial dust speed relative to the detector alters the time-dependent outputs. There are no changes to the equilibrium potential or temperature values, and thus ablation is not altered. Since the dust grains are feeling the same drag force from the plasma, the only effect is shifting the speed plot vertically.

Figures A.3 and A.4 have been altered from the baseline to demonstrate the effects of shifting from the SL regime where $r_d > \lambda_D$ to the OML regime where $r_d < \lambda_D$. In these plots, the baseline values were $r_{d0} = 4$ μm, $n_p = 10^{21}$ m^{-3}, $T_p = 10$ eV, $m_i = 1.0079$ amu (hydrogen plasma), and $v_f = 30$ km/s. Also note the varying timespan for each figure.

Figure A.3 demonstrates slight variations in the SL-OML shift by changing the initial size of the grains. From these graphs, we can determine that the equilibrium potential and temperature values change when shifting from SL to OML regimes and are dependent on the plasma parameters. We can also see that the ablation rates are different for various sized grains, and that ablation is more aggressive in the OML regime. The speeds of these grains appear to approach an asymptote when they get close to fully ablating.

Figure A.4 shows variations in the SL-OML shift by changing the ion mass of the plasma. Because of the longer timespan, grains do not appear to stay in OML theory for very long, and OML regime ablation seems instant, but we know from Figure A.3 that this is not the

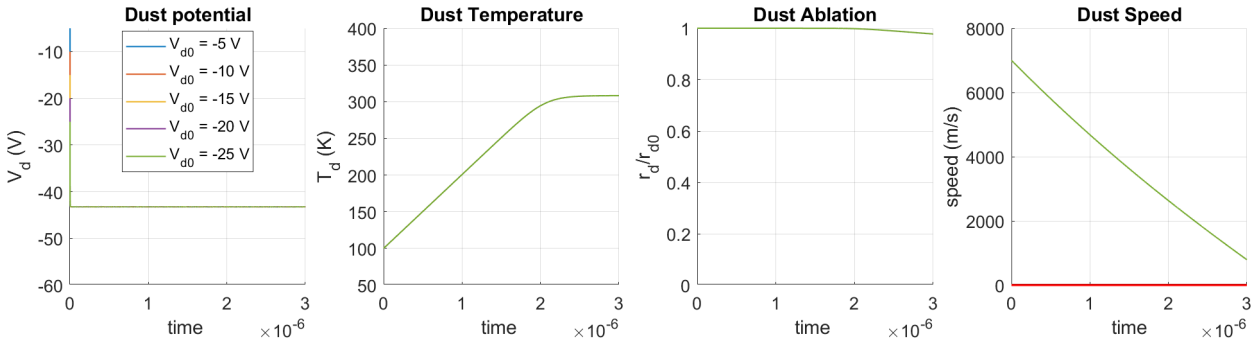

Figure A.1: Changing the initial dust potential relative to the plasma does not visibly alter any of the relevant outputs.

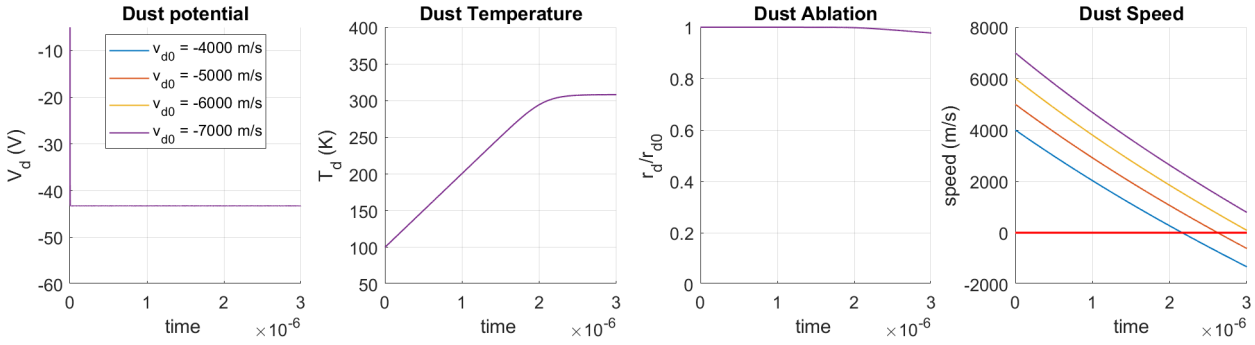

Figure A.2: Changing the initial dust velocity does not affect the potential, temperature, or ablation of the grain. The speed plot is translated vertically depending on initial velocity.

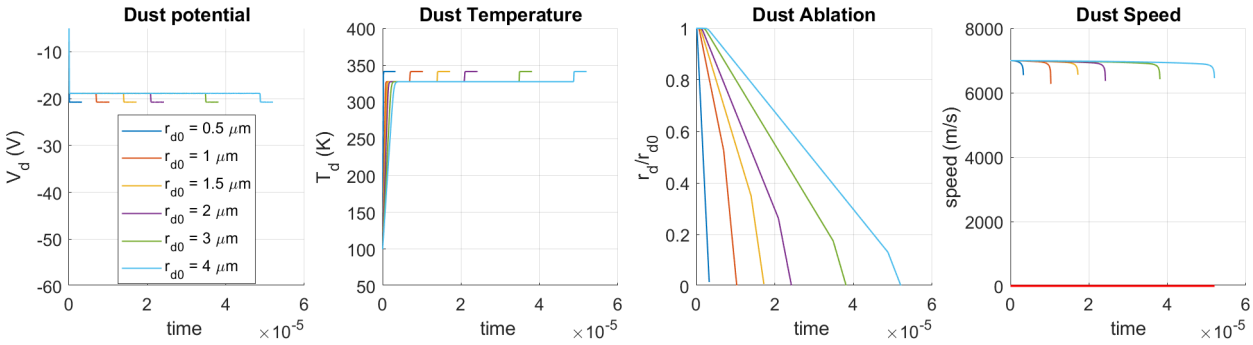

Figure A.3: Changing dust size does not change the equilibrium potential or temperature values, but there are different values for the SL and OML regimes. These regimes also influence ablation rates, and we see dust speed asymptotes when grains fully ablate.

case. In both regimes, the equilibrium potential and temperature changes with changing plasma parameters. Interestingly, the OML equilibrium potential is lower than the SL value for H plasma, but vice versa for heavier ion masses. We can also observe that the switch from SL to OML regimes occurs at the same dust size, which would be true unless λ_D were altered by adjusting T_p or n_p. Further, we see in the dust speed graph that all the grains have a small asymptote when they fully ablate in the OML regime. For a Xe plasma, we see the grain speed would approach the plasma flow speed given enough time and no ablation in the SL regime.

A reasonable explanation for the differences in SL and OML regimes is the differences in effective plasma densities used in each theory and the inclusion or exclusion of Coulomb forces. As established in Chapter 2, the sheath decreases the effective plasma density used for current and heat flux calculations to n_{sp} in SL theory. OML theory uses the full plasma density n_p. OML theory also incorporates long-distance Coulomb interaction forces into its force of drag while SL theory only includes collisional forces. These criteria may explain why equilibrium temperature is higher, ablation rates are greater, and velocities asymptote in OML theory. As discussed elsewhere, more study is needed to determine what physics to

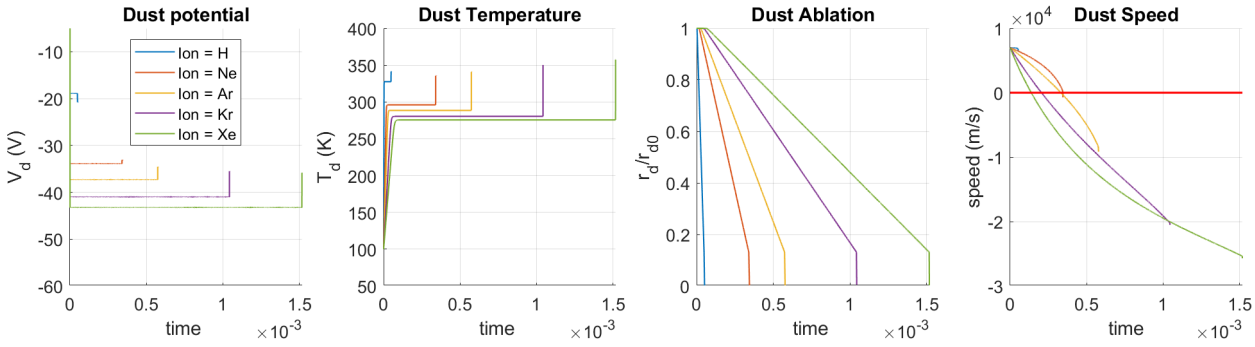

Figure A.4: Changing the plasma parameters will alter the equilibrium values for both SL and OML regimes. Ablation in the OML regime is much more aggressive than in the SL regime, and grain velocity almost instantly asymptotes as the grain rapidly ablates in the OML regime.

incorporate when $r_d \approx \lambda_D$.

Figure A.5 shows how changing the initial dust temperature affects the velocity of the grain with respect to the sheet length. Because of how the x-axis is constructed, this plot also provides insight on altering the plasma density n_p.

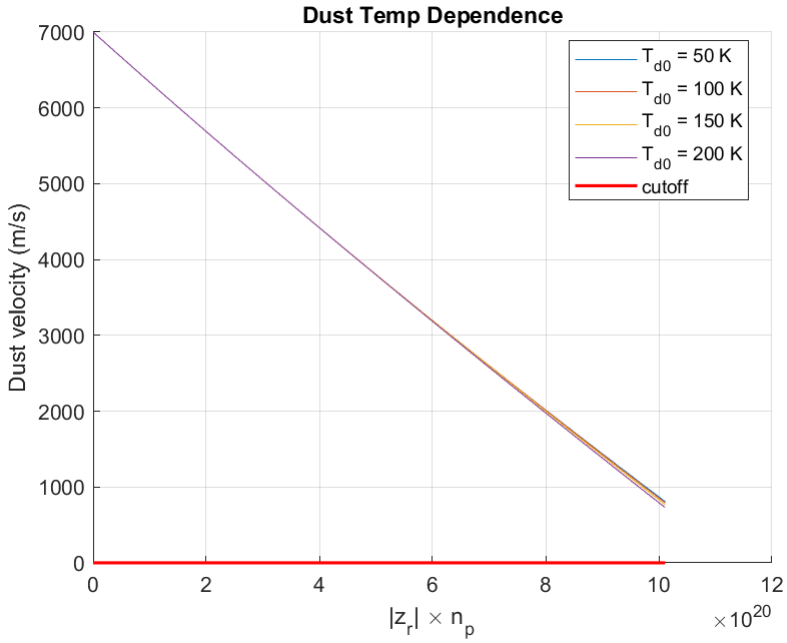

Figure A.5: Effects on dust grain velocity from changing the initial dust temperature. The x-axis is the same as in Figure 3.7. Altering this parameter has little effect.

Appendix B

MATLAB CODE

Since this thesis work is primarily theoretical and model-based, the majority of the code used to create it is included here so that others may verify methods and attempt to reproduce results. The first section includes the final version of the function used throughout the rest of the code, which was developed from the physics outlined in Chapter 2. The remaining sections include code for all of the time plots, length dependent plots, contour plots, and dust collection analysis that is included in the thesis. Code for the additional plots is not included. This code was written to run on MATLAB version R2019b.

B.1 Primary Function

```
function [t,rd1,Vd1,Td1,vd1,xd1,zr1]=DustPlasmaDynamics2(rd0,Vd0,Td0,...
    vd0,zr0,tspan,Te,Ti,ne,ni,mi,vf,Ls,rhod,cd,delm,Em,W,m0,Lams,n0,T0)
%%%%%%%%%%%%%%%%%%%%%%%%%%%%%%%%%%%%%%%%%%%%%%%%%%%%%%%%%%%%%%%%%%%%%%%%%%%%
%
%This function produces time-varying predictions for the radius, relative
%potential, temperature, velocity, distance, and position relative to a
%plasma sheet for a dust grain introduced into a plasma. This program
%is highly based off the work done in the reference material, and depends
%on a wide variety of inputs for plasma and dust parameters. This model
%uses both Orbital Motion Limited theory, which requires dust radius ≤
%Debye length, and Sheath Limited theory, which requires dust radius >
%Debye length. It also assumes spherical dust grains, flow velocity of
%similar magnitude as ion thermal velocity and much less than electron
%thermal velocity, and a plasma temperature ≤ 15 eV.
%
%Author: Wesley Jackson   UW SPACE Lab   806-559-9017  20 Feb 2021
%
%Inputs:
%   rd0         -  initial dust grain radius (um)
%   Vd0         -  initial dust potential relative to plasma (V)
%   Td0         -  initial dust temperature (K)
%   tspan       -  time span (sec) [start end]
```

```
23 %   Te,Ti       -  plasma electron/ion temperature (eV)
24 %   ne,ni       -  plasma electron/ion density (m^-3)
25 %   mi          -  ion mass (kg)
26 %   vf          -  plasma flow velocity (km/s)
27 %   Ls          -  length of plasma sheet (m) (not used in this version)
28 %   rhod        -  dust grain density (kg/m^3)
29 %   cd          -  dust material specific heat (J/kg K)
30 %   delm,Em     -  secondary emission properties of dust mat. (n/a),(eV)
31 %   W           -  work function for dust material (eV)
32 %   m0          -  dust mat. molecular weight (amu)
33 %   Lams        -  dust mat. sublimation heat (J/mol)
34 %   n0,T0       -  material vapors density (m^-3) @ specific temp(K)
35 %
36 %Outputs: (all [column vectors])
37 %   t           -  analysis time (sec)
38 %   rd1         -  dust grain radius (m)
39 %   Vd1         -  dust grain relative potential (V)
40 %   Td1         -  dust grain temperature (K)
41 %   vd1         -  dust grain velocity (m/s)
42 %   xd1         -  dust grain displacement (m)
43 %   zr1         -  relative position btwn grain and plasma sheet (m)
44 %
45 %Constants:
46 %   e           -  elementary charge (C)
47 %   kB          -  Boltzmann constant (J/K)
48 %   kBeV        -  Boltzmann constant (eV/K)
49 %   me          -  electron mass (kg)
50 %   eps0        -  permittivity of space (F/m)
51 %   mu0         -  permeability of space (H/m)
52 %   h           -  Plank's constant (J*s)
53 %   sigma       -  Stefan-Boltzmann constant (W/m^2 K^4)
54 %   R           -  gas constant (J/mol K)
55 %   Twall       -  environment temperatue (K)   **(???)**
56 %   Tse         -  energy of departing secondary electrons (eV)
57 %
58 %Coupling:
59 %   ode45       -  Matlab function for solving differential eqns
60 %   DustPlasmaDynamicsODEs - nested function to describe relevant charging
61 %                           and heating diff. eqns
62 %
63 %References:
64 %   Ticos, Wang, Delzanno, and Lapenta. "Plasma dragged microparticles as
65 %       a method to measure plasma flows." Physics of Plasmas, October
66 %       2006.
67 %   P.C. Stangeby. "Plasma sheath transmission factors for tokamak edge
68 %       plasmas." The Physics of Fluids, 1984.
69 %%%%%%%%%%%%%%%%%%%%%%%%%%%%%%%%%%%%%%%%%%%%%%%%%%%%%%%%%%%%%%%%%%%%%%%%%%%%
70
71 % Plasma Physics constants
72 e=1.6022*10^(-19); %elementary charge (C)
```

```
kB=1.380649*10^(-23); %Boltzmann constant (J/K)
 kBeV=1380649/16021766340; %Boltzmann constant (eV/K)
me=9.1094*10^(-31); %electron mass (kg)
eps0=8.8542*10^(-12); %permittivity of space (F/m)
mu0=4*pi*10^(-7); %permeability of space (H/m)
h=6.6261*10^(-34); %Plank constant (J*s)
sigma=5.6705*10^(-8); %Stefan-Boltzmann constant (W/m^2 K^4)
R=8.31; %gas constant (J/mol K)

Twall=290; %(K) [used in Gamrad]
Tse=3; %energy of secondary electron (eV)
  Tse=Tse/kBeV; %convert to (K)

% Input conversion
rd0=rd0*10^(-6); %convert to (m)
kBTeeV=Te; %(eV)
Te=Te/kBeV; Ti=Ti/kBeV; %convert to (K)
 vti=sqrt(2*kB*Ti/mi); %ion thermal speed (m/s)
vf=vf*1000; %convert to (m/s)
 lamDi=sqrt((eps0*kB*Ti)/(ni*e^2)); %ion Debye length (m)
 lamDe=sqrt((eps0*kB*Te)/(ne*e^2)); %electron Debye length (m)
  lams=(lamDe^(-2)+lamDi^(-2))^(-.5); %Debye shielding length (m)
EmeV=Em; %(eV)
Em=Em*1.602176634*10^(-19); %convert to (J)
W=W*1.602176634*10^(-19); %convert to (J)
mu=m0*10^(-3); %dust material molecular density (kg/mol)
m0=m0*(1.66053886*10^(-27)); %convert to (kg)

% Key values outside loop for optimization
u=vf/vti; %normalized ion flow speed (unitless)
erfu=erf(u); %define value for error funtion of u
%function for integration for use in Ise
energyfxn=@(E) E.^2.*exp(-E./(kBTeeV)-2.*sqrt(E./EmeV));
energyint=integral(energyfxn,0,Inf); %(eV^3)
energyint=energyint*(1.602176634*10^(-19))^3; %convert to (J^3)

% % Check Values of Key Parameters
% % **Not recommended for non-time-dependent plots**
% if rd0≤lams %% Orbital Motion Limited regime %%
%     fprintf('rd = %g ≤ lams = %g --- OML regime\n',rd0,lams);
%     checktxt=['vf = %g (should be same close to same order as) '...
%         'vti = %g (and much smaller than) vte = %g \n'];
%     fprintf(checktxt,vf,vti,sqrt(2*kB*Te/me));
%     fprintf('ion sound speed = %g \n',sqrt((kB*(Ti+Te))/mi));
% else %% if rd > lams %%  %% Sheath Limited regime %%
%     fprintf('rd = %g > lams = %g --- SL regime\n',rd0,lams);
%     checktxt=['vf = %g (should be same close to same order as) '...
%         'vti = %g (and much smaller than) vte = %g \n'];
%     fprintf(checktxt,vf,vti,sqrt(2*kB*Te/me));
%     fprintf('ion sound speed = %g \n',sqrt((kB*(Ti+Te))/mi));
```

```
% end


% Compute the differential eqns
y0=[rd0;Vd0;Td0;vd0;0;zr0]; %initial conditions
%coupled ODE solver (uses explicit Runge-Kutta (4,5) method)
[t,y]=ode45(@(t,x)DustPlasmaDynamicsODEs(t,x),tspan,y0);
%extract individual outputs from ode45 output
rd1=y(:,1); Vd1=y(:,2); Td1=y(:,3); vd1=y(:,4); xd1=y(:,5); zr1=y(:,6);



% Function that defines the ODEs
    function dxdt = DustPlasmaDynamicsODEs(¬,x)

        %define dependent variables
        rd= x(1); Vd= x(2); Td= x(3); vd= x(4); xd= x(5); zr=x(6);

        %(attempts at modifying density to simulate a finite plasma sheet)
        %np=ni.*heaviside(real(zr)).*heaviside(Ls-real(zr))+1;
        %np=ni.*gaussmf(zr,[2 zr0]);

    if rd≤lams %%%% Orbital Motion Limited regime %%%%

        if real(Vd)≤0 %%% if Vd < 0 (negative relative dust potential) %%%

            % Charging
            %eqn(4) ion current
            Ii= pi.*(rd.^2).*e.*ni.*sqrt((8*kB*Ti)/(pi*mi))*...
                ((sqrt(pi)/(4*u)).*(1+2*u^2-(2*e.*Vd)./(kB*Ti)).*erfu+...
                .5*exp(-u^2));
            %eqn(8) electron current
            Ie= -pi.*(rd.^2).*e.*ne.*sqrt((8*kB*Te)/(pi*me)).*...
                exp((e.*Vd)./(kB*Te));
            %eqn(11) secondary electron current
            Ise=(8*pi^2*e)/(me^2)*7.4*delm/Em.*ne.*(me/(2*pi*kB*Te))^1.5...
                .*rd.^2.*exp(e.*Vd/(kB*Te))*energyint;
            %eqn(13a) thermionic emission current (can change sign of Vd)*
            Ith= ((16*pi^2.*(rd.^2).*e*me.*(kB.*Td).^2)./(h^3)).*...
                exp(-W./(kB.*Td));

            % Heating
            %eqn(20) ion heat flux
            Gami= sqrt(pi).*rd.^2.*ni.*(kB*Ti)*(vti/u).*...
                (u.*(2.5+u^2-(2*e.*Vd)./(kB*Ti)).*exp(-u^2)+...
                sqrt(pi).*(.75+3*u^2+u^4-(e.*Vd)./(kB*Ti).*(1+2*u^2-...
                (e.*Vd)./(kB*Ti))).*erfu);
            %eqn(25) other heat flux terms
            Game= 2*kB*Te.*abs(Ie)./e; %electon heat flux
```

```
173             Gamth= 2*kB.*Td.*Ith./e; %thermionic electron heat flux
174             Gamse= 2*kB*Tse.*Ise./e; %secondary electron heat flux
175
176
177         else  %%% if Vd > 0 (positive relative dust potential) %%%
178             Ii=0; Ie=0; Ise=0; Ith=0; Gami=0; Game=0; Gamse=0; Gamth=0;
179             disp('WARNING: Positive Vd (OML), model incomplete');
180
181         end
182
183     else %% if rd > lams %%  %%%% Sheath Limited regime %%%%
184
185         if real(Vd)≤0 %%% if Vd < 0 (negative relative dust potential) %%%
186
187         % Charging
188         %calculate factor by which the sheath limits incident particles
189         nsi=(1/(2+u))*ni; nse=(1/(2+u))*ne;
190         %eqn(14) ion current
191         Ii= 4*pi.*(rd.^2).*e.*nsi.*sqrt(kB*(Te+Ti)/mi);
192         %eqn(8) electron current
193         Ie= -pi.*(rd.^2).*e.*nse.*sqrt((8*kB*Te)/(pi*me)).*...
194             exp((e.*Vd)./(kB*Te));
195         %eqn(11) secondary electron current
196         Ise=(8*pi^2*e)/(me^2)*7.4*delm/Em.*nse.*(me/(2*pi*kB*Te))^1.5...
197             .*rd.^2.*exp(e.*Vd/(kB*Te))*energyint;
198         %eqn(13a) thermionic emission current
199         Ith= ((16*pi^2.*(rd.^2).*e*me.*(kB.*Td).^2)./(h^3)).*...
200             exp(-W./(kB.*Td));
201
202         % Heating
203         %eqn(27b) ion heat flux
204         Gami= (2.5*kB*Ti-e.*Vd).*(Ii./e);
205         %eqn(27a) electron heat flux
206         Game= 2*kB*Te.*(abs(Ie)./e);
207         %eqn(25b) thermionic electron heat flux
208         Gamth= 2*kB.*Td.*Ith./e;
209         %eqn(25c) secondary electron heat flux
210         Gamse= 2*kB*Tse.*Ise./e;
211
212         else  %%% if Vd > 0 (positive relative dust potential) %%%
213             Ii=0; Ie=0; Ise=0; Ith=0; Gami=0; Game=0; Gamse=0; Gamth=0;
214             disp('WARNING: Positive Vd (SL), model incomplete');
215
216         end
217     end
218
219         %%%% Same for all regimes %%%%
220
221         % Charging
222         Cd= 4*pi*eps0.*rd.*(1+rd./lams); %dust grain capacitance (F)
```

```
223         %eqn(15) Overall Charging Eqn
224         dVd_dt= (Ie+Ii+Ise+Ith)./Cd; % (V/s)
225
226         % Heating
227         Gamrad= 4*pi.*rd.^2.*sigma.*(Td.^4-Twall^4); %radiated heat flux
228         md= (4/3)*pi.*(rd.^3).*rhod; %dust grain mass (kg)
229
230
231         %%% Drag Forces %%%
232
233         %additional equations necessary for force formulae
234         phi=e.*Vd./(kB*Ti);
235         s=sqrt((mi*(vf-vd).^2)./(2*kB*Ti));
236         Lami=sqrt(eps0*kB*Ti./ni).*3./(e*phi.*rd.*(1+rd./lams));
237         G0=8.*s./(3*sqrt(pi)).*sqrt(1+9/64*pi.*s.^2); %eqn(30)
238         G2=s.*(.75*sqrt(pi)+s.^3).^(-1); %eqn(31)
239
240         %eqn(29) drag forces
241         %collisional drag force
242         Fcol=2*pi.*rd.^2*kB*Ti.*ni.*G0;
243         %Coulomb interation drag force
244         Fcoul=2*pi.*rd.^2*kB*Ti.*ni.*phi.^2.*log(Lami).*G2;
245
246
247         %%%% Defining Final ODEs %%%%
248
249         %eqn(18) change in mass
250         mddot= 4*pi.*rd.^2.*m0.*sqrt((2*kB.*Td)./(pi*m0)).*(n0*T0./Td).*...
251             exp((Lams/R).*(1/T0-1./Td));
252         %eqn(17) change in radius
253         drd_dt= -mddot./(4*pi.*rd.^2.*rhod);
254         %eqn(16) Overall Heating Eqn
255         dTd_dt= (Game+Gami-Gamse...
256             -Gamth-Gamrad-(Lams/mu).*mddot)./(md.*cd);
257         %eqn(33) velocity equation
258         if rd≤lams %% OML %%
259             dvd_dt=(Fcol+Fcoul)./md;
260         else %rd>lams %% SL %%
261             dvd_dt=(Fcol)./md;
262         end
263         dxd_dt=vd; %eqn(32) distance equation (m)
264         dzr_dt=vd-vf; %grain, plasma sheet relative position (m)
265
266         dxdt=zeros(6,1);
267         %define set of ODEs
268         dxdt(1)=drd_dt;
269         dxdt(2)=dVd_dt;
270         dxdt(3)=dTd_dt;
271         dxdt(4)=dvd_dt;
272         dxdt(5)=dxd_dt;
```

```
273         dxdt(6)=dzr_dt;
274
275     end
276
277 end
```

B.2 Code for Time Dependent Plots

```
1  %% SPACE Lab Plasma Dust Analysis - Time Dependent Plots %%
2  %%%%%%%%%%%%%%%%%%%%%%%%%%%%%%%%%%%%%%%%%%%%%%%%%%%%%%%%%%%%%%%%%%%%%%%%%%%%
3  %
4  %This script seeks to analyze the time dependent effects of various plasma
5  %parameters on dust grains in a flowing plasma. Grain material is water
6  %ice, though properties of graphite are included (and commented out) as
7  %well. The function 'DustPlasmaDynamics2.m' is heavily relied on. See
8  %documentation of that code for more info.
9  %
10 %Author: Wesley Jackson   UW SPACE Lab   806-559-9017  October 2020
11 %
12 %Coupling:
13 %   DustPlasmaDynamics2 - produces time-varying predictions for dust grain
14 %                         properties based on dust and plasma parameter
15 %                         inputs
16 %%%%%%%%%%%%%%%%%%%%%%%%%%%%%%%%%%%%%%%%%%%%%%%%%%%%%%%%%%%%%%%%%%%%%%%%%%%%
17 clear all; close all; clc;
18
19 %% Initialize
20 rd0=1; %initial dust radius (um)
21 Vd0=-5; %initial dust potential relative to plasma (V)
22 Td0=100; %initial dust temp (K)
23 vd0=-7000; %initial dust velocity (m/s)
24 zr0=0; %initial relative position btwn grain and plasma sheet (m)
25
26 %plasma parameters
27 Te=10; Ti=10; %plasma temp (eV)
28 ne=10^22; ni=10^22; %plasma density (m^-3)
29 mi=(131.29)*1.66053906660e-27; %ion mass (kg) (Xe)
30 vf=30; %ion flow speed (km/s)
31 Ls=.05; %length of plasma sheet (m)
32 Ls_des=0.05; %desired length of plasma sheet (m)
33
34 %dust parameters
35
36 %   %for carbon**
37 % rhod=2230; %dust material density (kg/m^3)
38 % cd=750; %dust material specific heat (J/kg K)
39 % delm=1; Em=250; %secondary emission properties (n/a),(eV)
```

```
% W=4.7; %work function (eV)
%  m0=12; %molecular weight (amu)
%  Lams=7.15*10^5; %sublimation heat (J/mol)
%  mu=12*10^(-3); %molecular density (kg/mol)
% %material vapors density (m^-3) @ specific temp(K)
%  n0=1.83*10^24; T0=4000;

    %for water ice**
rhod=916.8; %dust material density (kg/m^3)
cd=2030; %dust material specific heat (J/kg K)
delm=2.8; Em=600; %secondary emission properties (n/a),(eV)
W=4.2; %work function (eV)
 m0=18.015; %molecular weight (amu)
 Lams=51100; %sublimation heat (J/mol)
 mu=m0*10^(-3); %molecular density (kg/mol)
%material vapors density (m^-3) @ specific temp(K)
 n0=2.897*10^22; T0=250;

%time span for analysis (sec)
tspan= 0 :1e-9: 3e-6;


%% Time Dependent Plots
close all
%specify colors for plot lines (needed for plotting consistency)
color = [    0    0.4470    0.7410
        0.8500    0.3250    0.0980
        0.9290    0.6940    0.1250
        0.4940    0.1840    0.5560
        0.4660    0.6740    0.1880
        0.3010    0.7450    0.9330
        0.6350    0.0780    0.1840];


%%% Dependence on initial dust temp %%%
Td0=[50 100 150 200];
%define tiled figure attributes (requires R2019b or later)
figure('Units','centimeters','Position',[.5 6 33 9]);
tfig = tiledlayout(1,4,'TileSpacing','none','Padding','none');
ax1=nexttile(1); hold on; grid on; legend show; legend('Location','best');
title('Dust potential'); xlabel('time '); ylabel('V_d (V)');ylim([-60 -5]);
ax2=nexttile(2); hold on; grid on; ylim([50 400]);
title('Dust Temperature'); xlabel('time '); ylabel('T_d (K)');
ax3=nexttile(3); hold on; grid on; ylim([0 1]);
title('Dust Ablation'); xlabel('time '); ylabel('r_d/r_d0');
ax4=nexttile(4); hold on; grid on;
title('Dust Speed'); xlabel('time'); ylabel('speed (m/s)');

for n=1:size(Td0,2)
    [t,rd1,Vd1,Td1,vd1,xd1,zr1]=DustPlasmaDynamics2(rd0,Vd0,Td0(n),vd0,...
```

```
90          zr0,tspan,Te,Ti,ne,ni,mi,vf,Ls,rhod,cd,delm,Em,W,m0,Lams,n0,T0);
91      legtxt=['T_d_0 = ',num2str(Td0(n)),' K']; %define legend
92
93      plot(ax1,t,Vd1,'DisplayName',legtxt);
94      plot(ax2,t,Td1);
95      plot(ax3,t,(rd1.*10^6)./rd0);
96      plot(ax4,t,-vd1,'Color',color(n,:));
97      plot(ax4,t,zeros(size(t)),'r','LineWidth',1.5); %cutoff value
98  end
99  hold off
100 saveas(gcf,'time plot - dust temp.png');
101 Td0=100;
102
103
104 %%% Dependence on initial dust size %%%
105 rd0=[0.25 0.5 1 1.5 2 3];
106 %define tiled figure attributes (requires R2019b or later)
107 figure('Units','centimeters','Position',[.5 6 33 9]);
108 tfig = tiledlayout(1,4,'TileSpacing','none','Padding','none');
109 ax1=nexttile(1); hold on; grid on; legend show; legend('Location','best');
110 title('Dust potential'); xlabel('time '); ylabel('V_d (V)');ylim([-60 -5]);
111 ax2=nexttile(2); hold on; grid on; ylim([50 400]);
112 title('Dust Temperature'); xlabel('time '); ylabel('T_d (K)');
113 ax3=nexttile(3); hold on; grid on; ylim([0 1]);
114 title('Dust Ablation'); xlabel('time '); ylabel('r_d/r_d0');
115 ax4=nexttile(4); hold on; grid on;
116 title('Dust Speed'); xlabel('time'); ylabel('speed (m/s)');
117
118 for n=1:size(rd0,2)
119     [t,rd1,Vd1,Td1,vd1,xd1,zr1]=DustPlasmaDynamics2(rd0(n),Vd0,Td0,vd0,...
120         zr0,tspan,Te,Ti,ne,ni,mi,vf,Ls,rhod,cd,delm,Em,W,m0,Lams,n0,T0);
121     legtxt=['r_d_0 = ',num2str(rd0(n)),' \mum']; %define legend
122
123     plot(ax1,t,Vd1,'DisplayName',legtxt);
124     plot(ax2,t,Td1);
125     plot(ax3,t,(rd1.*10^6)./rd0(n));
126     plot(ax4,t,-vd1,'Color',color(n,:));
127     plot(ax4,t,zeros(size(t)),'r','LineWidth',1.5); %cutoff value
128 end
129 hold off
130 saveas(gcf,'time plot - dust size.png');
131 rd0=1;
132
133
134 %%% Dependence on plasma temp %%%
135 Tp=[5 10 15];
136 Te=Tp; Ti=Tp;
137 %define tiled figure attributes (requires R2019b or later)
138 figure('Units','centimeters','Position',[.5 6 33 9]);
139 tfig = tiledlayout(1,4,'TileSpacing','none','Padding','none');
```

```
ax1=nexttile(1); hold on; grid on; legend show; legend('Location','best');
title('Dust potential'); xlabel('time '); ylabel('V_d (V)');ylim([-60 -5]);
ax2=nexttile(2); hold on; grid on; ylim([50 400]);
title('Dust Temperature'); xlabel('time '); ylabel('T_d (K)');
ax3=nexttile(3); hold on; grid on; ylim([0 1]);
title('Dust Ablation'); xlabel('time '); ylabel('r_d/r_d0');
ax4=nexttile(4); hold on; grid on;
title('Dust Speed'); xlabel('time'); ylabel('speed (m/s)');

for n=1:size(Tp,2)
    [t,rd1,Vd1,Td1,vd1,xd1,zr1]=DustPlasmaDynamics2(rd0,Vd0,Td0,vd0,...
        zr0,tspan,Te(n),Ti(n),ne,ni,mi,vf,Ls,rhod,cd,delm,Em,W,m0,...
        Lams,n0,T0);
    legtxt=['T_p = ',num2str(Tp(n)),' eV']; %define legend

    plot(ax1,t,Vd1,'DisplayName',legtxt);
    plot(ax2,t,Td1);
    plot(ax3,t,(rd1.*10^6)./rd0);
    plot(ax4,t,-vd1,'Color',color(n,:));
    plot(ax4,t,zeros(size(t)),'r','LineWidth',1.5); %cutoff value
end
hold off
saveas(gcf,'time plot - plasma temp.png');
Tp=10; Te=Tp; Ti=Tp;


%%% Dependence on plasma density %%%
np=[10^19 10^20 10^21 1e+22 1.01e+23];
ne=np; ni=np;
%define tiled figure attributes (requires R2019b or later)
figure('Units','centimeters','Position',[.5 6 33 9]);
tfig = tiledlayout(1,4,'TileSpacing','none','Padding','none');
ax1=nexttile(1); hold on; grid on; legend show; legend('Location','best');
title('Dust potential'); xlabel('time '); ylabel('V_d (V)');ylim([-60 -5]);
ax2=nexttile(2); hold on; grid on; ylim([50 400]);
title('Dust Temperature'); xlabel('time '); ylabel('T_d (K)');
ax3=nexttile(3); hold on; grid on; ylim([0 1]);
title('Dust Ablation'); xlabel('time '); ylabel('r_d/r_d0');
ax4=nexttile(4); hold on; grid on;
title('Dust Speed'); xlabel('time'); ylabel('speed (m/s)');

for n=1:size(np,2)
    [t,rd1,Vd1,Td1,vd1,xd1,zr1]=DustPlasmaDynamics2(rd0,Vd0,Td0,vd0,...
        zr0,tspan,Te,Ti,ne(n),ni(n),mi,vf,Ls,rhod,cd,delm,Em,W,m0,...
        Lams,n0,T0);
    legtxt=['n_p = ',num2str(np(n)),' m^-^3']; %define legend

    plot(ax1,t,Vd1,'DisplayName',legtxt);
    plot(ax2,t,Td1);
    plot(ax3,t,(rd1.*10^6)./rd0);
```

```
    plot(ax4,t,-vd1,'Color',color(n,:));
    plot(ax4,t,zeros(size(t)),'r','LineWidth',1.5); %cutoff value
end
hold off
saveas(gcf,'time plot - plasma density.png');
np=10^22; ni=np; ne=np;


%%% Dependence on plasma type (ion mass) %%%
element={'H' 'Ne' 'Ar' 'Kr' 'Xe'};
mi=[1.0079 20.180 39.948 83.798 131.29].*1.66053906660e-27; %ion mass (kg)
%define tiled figure attributes (requires R2019b or later)
figure('Units','centimeters','Position',[.5 6 33 9]);
tfig = tiledlayout(1,4,'TileSpacing','none','Padding','none');
ax1=nexttile(1); hold on; grid on; legend show; legend('Location','best');
title('Dust potential'); xlabel('time '); ylabel('V_d (V)');ylim([-60 -5]);
ax2=nexttile(2); hold on; grid on; ylim([50 400]);
title('Dust Temperature'); xlabel('time '); ylabel('T_d (K)');
ax3=nexttile(3); hold on; grid on; ylim([0 1]);
title('Dust Ablation'); xlabel('time '); ylabel('r_d/r_d0');
ax4=nexttile(4); hold on; grid on;
title('Dust Speed'); xlabel('time'); ylabel('speed (m/s)');

for n=1:size(mi,2)
    [t,rd1,Vd1,Td1,vd1,xd1,zr1]=DustPlasmaDynamics2(rd0,Vd0,Td0,vd0,...
        zr0,tspan,Te,Ti,ne,ni,mi(n),vf,Ls,rhod,cd,delm,Em,W,m0,Lams,n0,T0);
    legtxt=['Ion = ',element{n},''']; %define legend

    plot(ax1,t,Vd1,'DisplayName',legtxt);
    plot(ax2,t,Td1);
    plot(ax3,t,(rd1.*10^6)./rd0);
    plot(ax4,t,-vd1,'Color',color(n,:));
    plot(ax4,t,zeros(size(t)),'r','LineWidth',1.5); %cutoff value
end
hold off
saveas(gcf,'time plot - ion mass.png');
mi=(131.29)*1.66053906660e-27; %ion mass (kg) (Xe)


%%% Dependence on plasma flow speed %%%
vf=[20 30 40];
%define tiled figure attributes (requires R2019b or later)
figure('Units','centimeters','Position',[.5 6 33 9]);
tfig = tiledlayout(1,4,'TileSpacing','none','Padding','none');
ax1=nexttile(1); hold on; grid on; legend show; legend('Location','best');
title('Dust potential'); xlabel('time '); ylabel('V_d (V)');ylim([-60 -5]);
ax2=nexttile(2); hold on; grid on; ylim([50 400]);
title('Dust Temperature'); xlabel('time '); ylabel('T_d (K)');
ax3=nexttile(3); hold on; grid on; ylim([0 1]);
title('Dust Ablation'); xlabel('time '); ylabel('r_d/r_d0');
```

```
ax4=nexttile(4); hold on; grid on;
title('Dust Speed'); xlabel('time'); ylabel('speed (m/s)');

for n=1:size(vf,2)
    [t,rd1,Vd1,Td1,vd1,xd1,zr1]=DustPlasmaDynamics2(rd0,Vd0,Td0,vd0,...
        zr0,tspan,Te,Ti,ne,ni,mi,vf(n),Ls,rhod,cd,delm,Em,W,m0,Lams,n0,T0);
    legtxt=['v_f = ',num2str(vf(n)),' km/s']; %define legend

    plot(ax1,t,Vd1,'DisplayName',legtxt);
    plot(ax2,t,Td1);
    plot(ax3,t,(rd1.*10^6)./rd0);
    plot(ax4,t,-vd1,'Color',color(n,:));
    plot(ax4,t,zeros(size(t)),'r','LineWidth',1.5); %cutoff value
end
hold off
saveas(gcf,'time plot - flow speed.png');
vf=30;
```

B.3 Code for Length Dependent Plots

```
%% SPACE Lab Plasma Dust Analysis - Length Dependent Plots %%
%%%%%%%%%%%%%%%%%%%%%%%%%%%%%%%%%%%%%%%%%%%%%%%%%%%%%%%%%%%%%%%%%%%%%%%%%%%%%%%
%
%This script seeks to analyze the effects various plasma parameters have on
%the velocity of a dust grain travelling through a plasma. Each plot is
%designed to include possible variations in plasma density and sheet
%length. Dust grain material is water ice. The script heavily relies on
%'DustPlasmaDynamics2.m'. See documentation of that code for more info.
%
%Author: Wesley Jackson   UW SPACE Lab   806-559-9017  October 2020
%
%Coupling:
%   DustPlasmaDynamics2 - produces time-varying predictions for dust grain
%                         properties based on dust and plasma parameter
%                         inputs
%%%%%%%%%%%%%%%%%%%%%%%%%%%%%%%%%%%%%%%%%%%%%%%%%%%%%%%%%%%%%%%%%%%%%%%%%%%%%%%
clear all; close all; clc;

%% Initialize
rd0=1; %initial dust radius (um)
Vd0=-5; %initial dust potential relative to plasma (V)
Td0=100; %initial dust temp (K)
vd0=-7000; %initial dust velocity (m/s)
zr0=0; %initial relative position btwn grain and plasma sheet (m)

%plasma parameters
Te=10; Ti=10; %plasma temp (eV)
```

```
ne=10^22; ni=10^22; %plasma density (m^-3)
mi=(131.29)*1.66053906660e-27; %ion mass (kg) (Xe)
vf=30; %ion flow speed (km/s)
Ls=.05; %length of plasma sheet (m)
Ls_des=0.05; %desired length of plasma sheet (m)

%dust parameters for water ice
rhod=916.8; %dust material density (kg/m^3)
cd=2030; %dust material specific heat (J/kg K)
delm=2.8; Em=600; %secondary emission properties (n/a),(eV)
W=4.2; %work function (eV)
 m0=18.015; %molecular weight (amu)
 Lams=51100; %sublimation heat (J/mol)
 mu=m0*10^(-3); %molecular density (kg/mol)
%material vapors density (m^-3) @ specific temp(K)
 n0=2.897*10^22; T0=250;

%time span for analysis (sec)
tspan= 0 :1e-9: 3e-6;


%% Sheet Length Dependent Plots
close all;
%%% Analyzing Velocity vs. zr*np plot %%%

%define tiled figure attributes (requires R2019b or later)
figure('Units','centimeters','Position',[.5 2 33 18]);
tfig = tiledlayout(2,3,'TileSpacing','none','Padding','none');
ax1=nexttile(1); hold on; grid on; legend show;
legend('Location','best');title('(a) Plasma Density Dependence');
xlabel('|z_r| \times n_p'); ylabel('Dust velocity (m/s)');
ax2=nexttile(2); hold on; grid on; legend show;
legend('Location','best');title('(b) Plasma Temperature Dependence');
xlabel('|z_r| \times n_p'); ylabel('Dust velocity (m/s)');
ax3=nexttile(3); hold on; grid on; legend show;
legend('Location','best');title('(c) Ion Mass Dependence');
xlabel('|z_r| \times n_p'); ylabel('Dust velocity (m/s)');
ax4=nexttile(4); hold on; grid on; legend show;
legend('Location','best');title('(d) Plasma Flow Speed Dependence');
xlabel('|z_r| \times n_p'); ylabel('Dust velocity (m/s)');
ax5=nexttile(5); hold on; grid on; legend show;
legend('Location','best');title('(e) Dust Size Dependence');
xlabel('|z_r| \times n_p'); ylabel('Dust velocity (m/s)');
ax6=nexttile(6); hold on; grid on; legend show;
legend('Location','best');
title('(f) Dust Initial Velocity Dependence');
xlabel('|z_r| \times n_p'); ylabel('Dust velocity (m/s)');


%plasma density
```

```
np=[1.01e+23 5e+22 1e+22 0.5e+22];
ne=np; ni=np;
%for plotting clarity
sty={':' '-.' '--' '-'};
thic=[1 1.5 2 2.5];
for n=1:size(np,2)
    [t,rd1,Vd1,Td1,vd1,xd1,zr1]=DustPlasmaDynamics2(rd0,Vd0,Td0,vd0,zr0,...
        tspan,Te,Ti,ne(n),ni(n),mi,vf,Ls,rhod,cd,delm,Em,W,m0,Lams,n0,T0);
    legtxt=['n_p = ',num2str(np(n)),' m^-^3']; %define legend

    plot(ax1,abs(zr1)*np(n),-vd1,'LineStyle',sty{n},'LineWidth',thic(n),...
        'DisplayName',legtxt);
    if np(n) == max(np)
        npmaxzr1=abs(zr1);
    end
end
plot(ax1,npmaxzr1*max(np),zeros(size(zr1)),'r','LineWidth',1.5,...
    'DisplayName','cutoff');
np=1.0e+22; ne=np; ni=np;


%plasma temp
Tp=[5 10 15 20];
Te=Tp; Ti=Tp; %plasma temp (eV)
for n=1:size(Tp,2)
    [t,rd1,Vd1,Td1,vd1,xd1,zr1]=DustPlasmaDynamics2(rd0,Vd0,Td0,vd0,zr0,...
        tspan,Te(n),Ti(n),ne,ni,mi,vf,Ls,rhod,cd,delm,Em,W,m0,Lams,n0,T0);
    legtxt=['T_p = ',num2str(Tp(n)),' eV']; %define legend

    plot(ax2,abs(zr1)*np,-vd1,'DisplayName',legtxt);
end
plot(ax2,abs(zr1)*np,zeros(size(zr1)),'r','LineWidth',1.5,...
    'DisplayName','cutoff');
Tp=10; Te=Tp; Ti=Tp;


%ion mass
element={'Ne' 'Ar' 'Kr' 'Xe'};
mi=[20.180 39.948 83.798 131.29].*1.66053906660e-27; %ion mass (kg)
for n=1:size(mi,2)
    [t,rd1,Vd1,Td1,vd1,xd1,zr1]=DustPlasmaDynamics2(rd0,Vd0,Td0,vd0,...
        zr0,tspan,Te,Ti,ne,ni,mi(n),vf,Ls,rhod,cd,delm,Em,W,m0,Lams,n0,T0);
    legtxt=['Ion = ',element{n},'']; %define legend

    plot(ax3,abs(zr1)*np,-vd1,'DisplayName',legtxt);
end
plot(ax3,abs(zr1)*np,zeros(size(zr1)),'r','LineWidth',1.5,...
    'DisplayName','cutoff');
mi=131.29*1.66053906660e-27; %ion mass (kg)

```

```
128
129 %ion flow speed
130 vf=[20 25 30 35]; %ion flow speed (km/s)
131 for n=1:size(vf,2)
132     [t,rd1,Vd1,Td1,vd1,xd1,zr1]=DustPlasmaDynamics2(rd0,Vd0,Td0,vd0,...
133         zr0,tspan,Te,Ti,ne,ni,mi,vf(n),Ls,rhod,cd,delm,Em,W,m0,Lams,n0,T0);
134     legtxt=['v_f = ',num2str(vf(n)),' km/s']; %define legend
135
136     plot(ax4,abs(zr1)*np,-vd1,'DisplayName',legtxt);
137 end
138 plot(ax4,abs(zr1)*np,zeros(size(zr1)),'r','LineWidth',1.5,...
139     'DisplayName','cutoff');
140 vf=30; %ion flow speed (km/s)
141
142
143 %dust size
144 rd0=[0.25 0.5 1 2 3]; %um
145 for n=1:size(rd0,2)
146     [t,rd1,Vd1,Td1,vd1,xd1,zr1]=DustPlasmaDynamics2(rd0(n),Vd0,Td0,vd0,...
147         zr0,tspan,Te,Ti,ne,ni,mi,vf,Ls,rhod,cd,delm,Em,W,m0,Lams,n0,T0);
148     legtxt=['r_d_0 = ',num2str(rd0(n)),' \mum']; %define legend
149
150     plot(ax5,abs(zr1)*np,-vd1,'DisplayName',legtxt);
151 end
152 plot(ax5,abs(zr1)*np,zeros(size(zr1)),'r','LineWidth',1.5,...
153     'DisplayName','cutoff');
154 rd0=1; %um
155
156
157 %inital velocity
158 vd0=[-6000 -7000 -8000]; %initial dust velocity (m/s)
159 for n=1:size(vd0,2)
160     [t,rd1,Vd1,Td1,vd1,xd1,zr1]=DustPlasmaDynamics2(rd0,Vd0,Td0,vd0(n),...
161         zr0,tspan,Te,Ti,ne,ni,mi,vf,Ls,rhod,cd,delm,Em,W,m0,Lams,n0,T0);
162     legtxt=['v_d_0 = ',num2str(vd0(n)),' m/s']; %define legend
163
164     plot(ax6,abs(zr1)*np,-vd1,'DisplayName',legtxt);
165 end
166 plot(ax6,abs(zr1)*np,zeros(size(zr1)),'r','LineWidth',1.5,...
167     'DisplayName','cutoff');
168 vd0=-7000; %initial dust velocity (m/s)
169
170
171 %save the tiled figure
172 saveas(gcf,'length plots.png');
173
174
175 hold off
```

B.4 Code for Contour Plots

```
%% SPACE Lab Plasma Dust Analysis - Contour Plots %%
%%%%%%%%%%%%%%%%%%%%%%%%%%%%%%%%%%%%%%%%%%%%%%%%%%%%%%%%%%%%%%%%%%%%%%%%%%%%
%
%This script seeks to analyze the effects of changing various plasma
%parameters on the final size and velocity of dust particles with varying
%initial sizes and velocities subjected to a flowing plasma. Dust grain
%material is water ice. The script heavily relies on
%'DustPlasmaDynamics2.m'. See documentation of that code for more info.
%
%Author: Wesley Jackson   UW SPACE Lab   806-559-9017  January 2021
%
%Coupling:
%   DustPlasmaDynamics2 - produces time-varying predictions for dust grain
%                         properties based on dust and plasma parameter
%                         inputs
%%%%%%%%%%%%%%%%%%%%%%%%%%%%%%%%%%%%%%%%%%%%%%%%%%%%%%%%%%%%%%%%%%%%%%%%%%%%
clear all; close all; clc;

%% Initialize
Vd0=-5; %initial dust potential relative to plasma (V)
Td0=100; %initial dust temp (K)
zr0=0; %initial relative position btwn grain and plasma sheet (m)
vd0=[1 2 3 4 5 6 7 8 9 10]*(-1000); %range of relative speeds (m/s)
rd0=[.01 .05 .1 .15 .2 .25 .3 .35 .4 .45 .5 .55 .6 .65 .7 .75 .8 ...
    .85 .9 .95 1 1.05 1.1 1.15 1.2 1.25 1.3 1.35 1.4 1.45 1.5 1.55 1.6 ...
    1.65 1.7 1.75 1.8 1.85 1.9 2 2.25 2.5 3]; %range of grain size (um)
rd0=rd0'; %change to vertical vector

%plasma parameters
Te=10; Ti=10; %plasma temp (eV)
ne=10^22; ni=10^22; %plasma density (m^-3)
mi=(131.29)*1.66053906660e-27; %ion mass (kg) (Xe)
vf=20; %ion flow speed (km/s)
Ls=.05; %length of plasma sheet (m)
Ls_des=0.05; %desired length of plasma sheet (m)

%dust parameters for water ice
rhod=916.8; %dust material density (kg/m^3)
cd=2030; %dust material specific heat (J/kg K)
delm=2.8; Em=600; %secondary emission properties (n/a),(eV)
W=4.2; %work function (eV)
 m0=18.015; %molecular weight (amu)
 Lams=51100; %sublimation heat (J/mol)
 mu=m0*10^(-3); %molecular density (kg/mol)
%material vapors density (m^-3) @ specific temp(K)
 n0=2.897*10^22; T0=250;
```

```
47
48 %time span for analysis (sec)
49 tspan= 0 :1e-9: 3e-6;
50
51
52 %% Contour Plots - Varying Density
53 close all
54
55 np=[0.5e+22 1.0e+22 1.5e+22]; ne=np; ni=np; %plasma density (m^-3)
56
57 %pre-define figure for contour plot overlays
58 cfig = figure(5); cfig.Units='centimeters'; cfig.Position=[.5 6 33 9];
59 tcfig = tiledlayout(cfig,1,3,'TileSpacing','none','Padding','none');
60
61 for x=1:size(np,2)
62 rdf=zeros(size(rd0,1),size(vd0,2));
63 vdf=zeros(size(rd0,1),size(vd0,2));
64
65 for n=1:size(vd0,2)
66     tmax=1.1*Ls_des/(vd0(n)+vf*1000); %(sec)
67     tscale=10^(floor(log10(tmax))-3); %(sec)
68     tspan= 0 :tscale: tmax; %define time span for analysis
69
70     for m=1:size(rd0,1)
71         [t,rd1,Vd1,Td1,vd1,xd1,zr1]=DustPlasmaDynamics2(rd0(m),Vd0,Td0,...
72             vd0(n),zr0,tspan,Te,Ti,ne(x),ni(x),mi,vf,Ls,...
73             rhod,cd,delm,Em,W,m0,Lams,n0,T0);
74         %find output value closest to Ls_des
75         [val,idx]=min(abs(abs(real(zr1))-Ls_des));
76         %if more than 0.1% away from Ls_des, assume full ablation
77         if val>(.001*Ls_des)
78             rdf(m,n)=-.5e-06;
79             vdf(m,n)=100;
80         else
81             rdf(m,n)=rd1(idx);
82             vdf(m,n)=vd1(idx);
83         end
84     end
85 end
86
87 %define colormap with max value=white
88 parula2=colormap(parula); parula2(256,:)=1;
89
90 % Let Matlab draw the full contour plots
91 figure(1);
92 [C1,h1]=contourf(abs(vd0),rd0,real(rdf)); clabel(C1,h1);
93 title('Final Grain Radius'); xlabel('initial relative velocity (m/s)');
94 ylabel('initial grain radius (\mum)');
95 figure(2);
96 [C2,h2]=contourf(abs(vd0),rd0,-real(vdf)); clabel(C2,h2);
```

```
title('Final Velocity'); xlabel('initial relative velocity (m/s)');
ylabel('initial grain radius (\mum)');

% Define contours for final grain size
rmin=0; %min recoverable size (m)
rmax=max(rd0)*10^(-6);
rcont=rmin:0.5e-06:rmax; %size contours
% Define contours for final grain velocity
vmax=6000; %max allowable final speed (m/s)
vcont=0:1000:vmax; %velocity contours

% Draw specified contour plots and save for overlay
fig3= figure(3); %Final Grain Radius plot
fig3.Color=[1 1 1]; fig3.Units='centimeters'; fig3.Position=[10 6 11 9];
[C1,h1]=contourf(abs(vd0),rd0,real(rdf),rcont); clabel(C1,h1);
xlabel('initial relative velocity (m/s)');
ylabel('initial grain radius (\mum)');
title(sprintf('Plasma Density = %g m^{-3}',np(x)));
F1=getframe(gcf); RGB1=frame2im(F1); %save figure as image

fig4= figure(4); colormap(parula2); %Final Velocity plot
fig4.Color=[1 1 1]; fig4.Units='centimeters'; fig4.Position=[10 6 11 9];
[C2,h2]=contourf(abs(vd0),rd0,-real(vdf),vcont); clabel(C2,h2);
xlabel('initial relative velocity (m/s)');
ylabel('initial grain radius (\mum)');
title(sprintf('Plasma Density = %g m^{-3}',np(x)));
F2=getframe(gcf); RGB2=frame2im(F2); %save figure as image

% Put overlays on one figure
ax=nexttile(tcfig,x);
im1=image(RGB1); axis off; hold on;
im2=image(RGB2,'AlphaData',0.5);
set(ax,'XTick',[], 'YTick', []);
hold off

end

saveas(cfig,sprintf('ContDensitySL %gx%gx%g.png',...
    size(vd0,2),size(rd0,1),size(np,2)));
np=1.0e+22; ne=np; ni=np; %plasma density (m^-3)


%% Contour Plots - Varying Temperature
close all

Tp=[5 10 15];  Te=Tp; Ti=Tp; %plasma temp (eV)

%pre-define figure for contour plot overlays
cfig = figure(5); cfig.Units='centimeters'; cfig.Position=[.5 6 33 9];
tcfig = tiledlayout(cfig,1,3,'TileSpacing','none','Padding','none');
```

```
147
148 for x=1:size(Tp,2)
149 rdf=zeros(size(rd0,1),size(vd0,2));
150 vdf=zeros(size(rd0,1),size(vd0,2));
151
152 for n=1:size(vd0,2)
153     tmax=1.1*Ls_des/(vd0(n)+vf*1000); %(sec)
154     tscale=10^(floor(log10(tmax))-3); %(sec)
155     tspan= 0 :tscale: tmax; %define time span for analysis
156     for m=1:size(rd0,1)
157         [t,rd1,Vd1,Td1,vd1,xd1,zr1]=DustPlasmaDynamics2(rd0(m),Vd0,Td0,...
158             vd0(n),zr0,tspan,Te(x),Ti(x),ne,ni,mi,vf,Ls,...
159             rhod,cd,delm,Em,W,m0,Lams,n0,T0);
160         %find output value closest to Ls_des
161         [val,idx]=min(abs(abs(real(zr1))-Ls_des));
162         %if more than 0.1% away from Ls_des, assume full ablation
163         if val>(.001*Ls_des)
164             rdf(m,n)=-.5e-06;
165             vdf(m,n)=100;
166         else
167             rdf(m,n)=rd1(idx);
168             vdf(m,n)=vd1(idx);
169         end
170     end
171 end
172
173 %define colormap with max value=white
174 parula2=colormap(parula); parula2(256,:)=1;
175
176 % Let Matlab draw the full contour plots
177 figure(1);
178 [C1,h1]=contourf(abs(vd0),rd0,real(rdf)); clabel(C1,h1);
179 title('Final Grain Radius'); xlabel('initial relative velocity (m/s)');
180 ylabel('initial grain radius (\mum)');
181 figure(2);
182 [C2,h2]=contourf(abs(vd0),rd0,-real(vdf)); clabel(C2,h2);
183 title('Final Velocity'); xlabel('initial relative velocity (m/s)');
184 ylabel('initial grain radius (\mum)');
185
186 % Define contours for final grain size
187 rmin=0; %min recoverable size (m)
188 rmax=max(rd0)*10^(-6);
189 rcont=rmin:0.5e-06:rmax; %size contours
190 % Define contours for final grain velocity
191 vmax=6000; %max allowable final speed (m/s)
192 vcont=0:1000:vmax; %velocity contours
193
194 % Draw specified contour plots and save for overlay
195 fig3= figure(3); %Final Grain Radius plot
196 fig3.Color=[1 1 1]; fig3.Units='centimeters'; fig3.Position=[10 6 11 9];
```

```
[C1,h1]=contourf(abs(vd0),rd0,real(rdf),rcont); clabel(C1,h1);
xlabel('initial relative velocity (m/s)');
ylabel('initial grain radius (\mum)');
title(sprintf('Plasma Temperature = %g eV',Tp(x)));
F1=getframe(gcf); RGB1=frame2im(F1); %save figure as image

fig4= figure(4); colormap(parula2); %Final Velocity plot
fig4.Color=[1 1 1]; fig4.Units='centimeters'; fig4.Position=[10 6 11 9];
[C2,h2]=contourf(abs(vd0),rd0,-real(vdf),vcont); clabel(C2,h2);
xlabel('initial relative velocity (m/s)');
ylabel('initial grain radius (\mum)');
title(sprintf('Plasma Temperature = %g eV',Tp(x)));
F2=getframe(gcf); RGB2=frame2im(F2); %save figure as image

% Put overlays on one figure
ax=nexttile(tcfig,x);
im1=image(RGB1); axis off; hold on;
im2=image(RGB2,'AlphaData',0.5);
set(ax,'XTick',[], 'YTick', []);
hold off

end

saveas(cfig,sprintf('ContTempSL %gx%gx%g.png',...
    size(vd0,2),size(rd0,1),size(Tp,2)));
Tp=10;  Te=Tp; Ti=Tp; %plasma temp (eV)


%% Contour Plots - Varying Ion Mass
close all

element={'Ar' 'Kr' 'Xe'};
mi=[39.948 83.798 131.29].*1.66053906660e-27; %ion mass (kg)

%pre-define figure for contour plot overlays
cfig = figure(5); cfig.Units='centimeters'; cfig.Position=[.5 6 33 9];
tcfig = tiledlayout(cfig,1,3,'TileSpacing','none','Padding','none');

for x=1:size(mi,2)
rdf=zeros(size(rd0,1),size(vd0,2));
vdf=zeros(size(rd0,1),size(vd0,2));

for n=1:size(vd0,2)
    tmax=1.1*Ls_des/(vd0(n)+vf*1000); %(sec)
    tscale=10^(floor(log10(tmax))-3); %(sec)
    tspan= 0 :tscale: tmax; %define time span for analysis
    for m=1:size(rd0,1)
        [t,rd1,Vd1,Td1,vd1,xd1,zr1]=DustPlasmaDynamics2(rd0(m),Vd0,Td0,...
            vd0(n),zr0,tspan,Te,Ti,ne,ni,mi(x),vf,Ls,...
            rhod,cd,delm,Em,W,m0,Lams,n0,T0);
```

```
247         %find output value closest to Ls_des
248         [val,idx]=min(abs(abs(real(zr1))-Ls_des));
249         %if more than 0.1% away from Ls_des, assume full ablation
250         if val>(.001*Ls_des)
251             rdf(m,n)=-.5e-06;
252             vdf(m,n)=100;
253         else
254             rdf(m,n)=rd1(idx);
255             vdf(m,n)=vd1(idx);
256         end
257     end
258 end
259
260 %define colormap with max value=white
261 parula2=colormap(parula); parula2(256,:)=1;
262
263 % Let Matlab draw the full contour plots
264 figure(1);
265 [C1,h1]=contourf(abs(vd0),rd0,real(rdf)); clabel(C1,h1);
266 title('Final Grain Radius'); xlabel('initial relative velocity (m/s)');
267 ylabel('initial grain radius (\mum)');
268 figure(2);
269 [C2,h2]=contourf(abs(vd0),rd0,-real(vdf)); clabel(C2,h2);
270 title('Final Velocity'); xlabel('initial relative velocity (m/s)');
271 ylabel('initial grain radius (\mum)');
272
273 % Define contours for final grain size
274 rmin=0; %min recoverable size (m)
275 rmax=max(rd0)*10^(-6);
276 rcont=rmin:0.5e-06:rmax; %size contours
277 %define contours for final grain velocity
278 vmax=6000; %max allowable final speed (m/s)
279 vcont=0:1000:vmax; %velocity contours
280
281 % Draw specified contour plots and save for overlay
282 fig3= figure(3); %Final Grain Radius plot
283 fig3.Color=[1 1 1]; fig3.Units='centimeters'; fig3.Position=[10 6 11 9];
284 [C1,h1]=contourf(abs(vd0),rd0,real(rdf),rcont); clabel(C1,h1);
285 xlabel('initial relative velocity (m/s)');
286 ylabel('initial grain radius (\mum)');
287 title(sprintf('Ion = %s ',element{x}));
288 F1=getframe(gcf); RGB1=frame2im(F1); %save figure as image
289
290 fig4= figure(4); colormap(parula2); %Final Velocity plot
291 fig4.Color=[1 1 1]; fig4.Units='centimeters'; fig4.Position=[10 6 11 9];
292 [C2,h2]=contourf(abs(vd0),rd0,-real(vdf),vcont); clabel(C2,h2);
293 xlabel('initial relative velocity (m/s)');
294 ylabel('initial grain radius (\mum)');
295 title(sprintf('Ion = %s ',element{x}));
296 F2=getframe(gcf); RGB2=frame2im(F2); %save figure as image
```

```
297
298 % Put overlays on one figure
299 ax=nexttile(tcfig,x);
300 im1=image(RGB1); axis off; hold on;
301 im2=image(RGB2,'AlphaData',0.5);
302 set(ax,'XTick',[], 'YTick', []);
303 hold off
304
305 end
306
307 saveas(cfig,sprintf('ContMassSL %gx%gx%g.png',...
308     size(vd0,2),size(rd0,1),size(mi,2)));
309 mi=131.29.*1.66053906660e-27; %ion mass (kg) (Xe)
310
311
312 %% Contour Plots - Varying Plasma Speed
313 close all
314
315 vf=[20 30 40]; %ion flow speed (km/s)
316
317 %pre-define figure for contour plot overlays
318 cfig = figure(5); cfig.Units='centimeters'; cfig.Position=[.5 6 33 9];
319 tcfig = tiledlayout(cfig,1,3,'TileSpacing','none','Padding','none');
320
321 for x=1:size(vf,2)
322 rdf=zeros(size(rd0,1),size(vd0,2));
323 vdf=zeros(size(rd0,1),size(vd0,2));
324
325 for n=1:size(vd0,2)
326     tmax=1.1*Ls_des/(vd0(n)+vf(x)*1000); %(sec)
327     tscale=10^(floor(log10(tmax))-3); %(sec)
328     tspan= 0 :tscale: tmax; %define time span for analysis
329     for m=1:size(rd0,1)
330         [t,rd1,Vd1,Td1,vd1,xd1,zr1]=DustPlasmaDynamics2(rd0(m),Vd0,Td0,...
331             vd0(n),zr0,tspan,Te,Ti,ne,ni,mi,vf(x),Ls,...
332             rhod,cd,delm,Em,W,m0,Lams,n0,T0);
333         %find output value closest to Ls_des
334         [val,idx]=min(abs(abs(real(zr1))-Ls_des));
335         %if more than 0.1% away from Ls_des, assume full ablation
336         if val>(.001*Ls_des)
337             rdf(m,n)=-.5e-06;
338             vdf(m,n)=100;
339         else
340             rdf(m,n)=rd1(idx);
341             vdf(m,n)=vd1(idx);
342         end
343     end
344 end
345
346 %define colormap with max value=white
```

```
parula2=colormap(parula); parula2(256,:)=1;

% Let Matlab draw the full contour plots
figure(1);
[C1,h1]=contourf(abs(vd0),rd0,real(rdf)); clabel(C1,h1);
title('Final Grain Radius'); xlabel('initial relative velocity (m/s)');
ylabel('initial grain radius (\mum)');
figure(2);
[C2,h2]=contourf(abs(vd0),rd0,-real(vdf)); clabel(C2,h2);
title('Final Velocity'); xlabel('initial relative velocity (m/s)');
ylabel('initial grain radius (\mum)');

% Define contours for final grain size
rmin=0; %min recoverable size (m)
rmax=max(rd0)*10^(-6);
rcont=rmin:0.5e-06:rmax; %size contours
%define contours for final grain velocity
vmax=6000; %max allowable final speed (m/s)
vcont=0:1000:vmax; %velocity contours

% Draw specified contour plots and save for overlay
fig3= figure(3); %Final Grain Radius plot
fig3.Color=[1 1 1]; fig3.Units='centimeters'; fig3.Position=[10 6 11 9];
[C1,h1]=contourf(abs(vd0),rd0,real(rdf),rcont); clabel(C1,h1);
xlabel('initial relative velocity (m/s)');
ylabel('initial grain radius (\mum)');
title(sprintf('Plasma Speed = %g km/s',vf(x)));
F1=getframe(gcf); RGB1=frame2im(F1); %save figure as image

fig4= figure(4); colormap(parula2); %Final Velocity plot
fig4.Color=[1 1 1]; fig4.Units='centimeters'; fig4.Position=[10 6 11 9];
[C2,h2]=contourf(abs(vd0),rd0,-real(vdf),vcont); clabel(C2,h2);
xlabel('initial relative velocity (m/s)');
ylabel('initial grain radius (\mum)');
title(sprintf('Plasma Speed = %g km/s',vf(x)));
F2=getframe(gcf); RGB2=frame2im(F2); %save figure as image

% Put overlays on one figure
ax=nexttile(tcfig,x);
im1=image(RGB1); axis off; hold on;
im2=image(RGB2,'AlphaData',0.5);
set(ax,'XTick',[], 'YTick', []);
hold off

end

saveas(cfig,sprintf('ContSpeedSL %gx%gx%g.png',...
    size(vd0,2),size(rd0,1),size(vf,2)));
vf=20; %plasma flow velocity (km/s)

```

```
397
398 %% Contour Plots - Varying Sheet Length
399 close all
400
401 Ls_des=[0.025 0.05 0.075]; %desired length of plasma sheet (m)
402
403 %pre-define figure for contour plot overlays
404 cfig = figure(5); cfig.Units='centimeters'; cfig.Position=[.5 6 33 9];
405 tcfig = tiledlayout(cfig,1,3,'TileSpacing','none','Padding','none');
406
407 for x=1:size(Ls_des,2)
408 rdf=zeros(size(rd0,1),size(vd0,2));
409 vdf=zeros(size(rd0,1),size(vd0,2));
410
411 for n=1:size(vd0,2)
412     tmax=1.1*Ls_des(x)/(vd0(n)+vf*1000); %(sec)
413     tscale=10^(floor(log10(tmax))-3); %(sec)
414     tspan= 0 :tscale: tmax; %define time span for analysis
415     for m=1:size(rd0,1)
416         [t,rd1,Vd1,Td1,vd1,xd1,zr1]=DustPlasmaDynamics2(rd0(m),Vd0,Td0,...
417             vd0(n),zr0,tspan,Te,Ti,ne,ni,mi,vf,Ls,...
418             rhod,cd,delm,Em,W,m0,Lams,n0,T0);
419         %find output value closest to Ls_des
420         [val,idx]=min(abs(abs(real(zr1))-Ls_des(x)));
421         %if more than 0.1% away from Ls_des, assume full ablation
422         if val>(.001*Ls_des(x))
423             rdf(m,n)=-.5e-06;
424             vdf(m,n)=100;
425         else
426             rdf(m,n)=rd1(idx);
427             vdf(m,n)=vd1(idx);
428         end
429     end
430 end
431
432 %define colormap with max value=white
433 parula2=colormap(parula); parula2(256,:)=1;
434
435 % Let Matlab draw the full contour plots
436 figure(1);
437 [C1,h1]=contourf(abs(vd0),rd0,real(rdf)); clabel(C1,h1);
438 title('Final Grain Radius'); xlabel('initial relative velocity (m/s)');
439 ylabel('initial grain radius (\mum)');
440 figure(2);
441 [C2,h2]=contourf(abs(vd0),rd0,-real(vdf)); clabel(C2,h2);
442 title('Final Velocity'); xlabel('initial relative velocity (m/s)');
443 ylabel('initial grain radius (\mum)');
444
445 % Define contours for final grain size
446 rmin=0; %min recoverable size (m)
```

```
rmax=max(rd0)*10^(-6);
rcont=rmin:0.5e-06:rmax; %size contours
%define contours for final grain velocity
vmax=6000; %max allowable final speed (m/s)
vcont=0:1000:vmax; %velocity contours

% Draw specified contour plots and save for overlay
fig3= figure(3); %Final Grain Radius plot
fig3.Color=[1 1 1]; fig3.Units='centimeters'; fig3.Position=[10 6 11 9];
[C1,h1]=contourf(abs(vd0),rd0,real(rdf),rcont); clabel(C1,h1);
xlabel('initial relative velocity (m/s)');
ylabel('initial grain radius (\mum)');
title(sprintf('Plasma Sheet Length = %g m',Ls_des(x)));
F1=getframe(gcf); RGB1=frame2im(F1); %save figure as image

fig4= figure(4); colormap(parula2); %Final Velocity plot
fig4.Color=[1 1 1]; fig4.Units='centimeters'; fig4.Position=[10 6 11 9];
[C2,h2]=contourf(abs(vd0),rd0,-real(vdf),vcont); clabel(C2,h2);
xlabel('initial relative velocity (m/s)');
ylabel('initial grain radius (\mum)');
title(sprintf('Plasma Sheet Length = %g m',Ls_des(x)));
F2=getframe(gcf); RGB2=frame2im(F2); %save figure as image

% Put overlays on one figure
ax=nexttile(tcfig,x);
im1=image(RGB1); axis off; hold on;
im2=image(RGB2,'AlphaData',0.5);
set(ax,'XTick',[], 'YTick', []);
hold off

end

saveas(cfig,sprintf('ContLengthSL %gx%gx%g.png',...
    size(vd0,2),size(rd0,1),size(Ls_des,2)));
Ls_des=0.05; %desired length of plasma sheet (m)
```

B.5 Code for Feasibility Analysis

```
%% SPACE Lab Plasma Dust Analysis - Dust Collection %%
%%%%%%%%%%%%%%%%%%%%%%%%%%%%%%%%%%%%%%%%%%%%%%%%%%%%%%%%%%%%%%%%%%%%%%%%%%%%
%
%This script seeks to analyze the feasibility of a dust collection system
%that employs a plasma sheet to slow incoming dust grains by examining the
%necessary energy of the plasma, the rate of incoming dust grains, and the
%collected mass. Grain material is water ice. The script heavily relies on
%'DustPlasmaDynamics2.m'. See documentation of that code for more info.
%Some variables get their value from Table 2 of the reference.
```

```
%
%Author: Wesley Jackson   UW SPACE Lab   806-559-9017  February 2021
%
%Coupling:
%   DustPlasmaDynamics2 - produces time-varying predictions for dust grain
%                         properties based on dust and plasma parameter
%                         inputs
%
%Reference:
%   Porco, Dones, and Mitchell. "Could it be snowing microbes on Enceladus?
%       Assessing conditions in its plume and implications for future
%       missions." Astrobiology 17, Sep 2017.
%%%%%%%%%%%%%%%%%%%%%%%%%%%%%%%%%%%%%%%%%%%%%%%%%%%%%%%%%%%%%%%%%%%%%%%%%%%%
clear all; close all; clc;

%% Initialize
Vd0=-5; %initial dust potential relative to plasma (V)
Td0=100; %initial dust temp (K)
zr0=0; %initial relative position btwn grain and plasma sheet (m)
vd0=[1 2 3 4 5 6 7 8 9 10]*(-1000); %range of relative speeds (m/s)
rd0=[.01 .05 .1 .15 .2 .25 .3 .35 .4 .45 .5 .55 .6 .65 .7 .75 .8 ...
    .85 .9 .95 1 1.05 1.1 1.15 1.2 1.25 1.3 1.35 1.4 1.45 1.5 1.55 1.6 ...
    1.65 1.7 1.75 1.8 1.85 1.9 2 2.25 2.5 3]; %range of grain size (um)
rd0=rd0'; %change to vertical vector

%plasma parameters
Ls=.025; %length of plasma sheet (m)
np=1.0e+22; ne=np; ni=np; %plasma density (m^-3)
Tp=10;  Te=Tp; Ti=Tp; %plasma temp (eV)
mi=(131.29).*1.66053906660e-27; %ion mass (kg) (Xe)
vf=20; %plasma flow velocity (km/s)
Ls_des=0.025; %desired length of plasma sheet (m)

%dust parameters for water ice
rhod=916.8; %dust material density (kg/m^3)
cd=2030; %dust material specific heat (J/kg K)
delm=2.8; Em=600; %secondary emission properties (n/a),(eV)
W=4.2; %work function (eV)
 m0=18.015; %molecular weight (amu)
 Lams=51100; %sublimation heat (J/mol)
 mu=m0*10^(-3); %molecular density (kg/mol)
%material vapors density (m^-3) @ specific temp(K)
 n0=2.897*10^22; T0=250;

%time span for analysis (sec)
tspan= 0 :1e-9: 3e-6;


%% Contour Plot for Energy and Dust Collection Analysis
close all
```

```
60
61 %pre-define figure for contour plot overlays
62 cfig = figure(5);%,'units','centimeters','position',[3 6 20 12]);
63 cfig.Units='centimeters'; cfig.Position=[.5 6 11 9];
64 tcfig = tiledlayout(cfig,1,1,'TileSpacing','none','Padding','none');
65
66 %pre-define outputs matricies
67 rdf=zeros(size(rd0,1),size(vd0,2));
68 vdf=zeros(size(rd0,1),size(vd0,2));
69
70 for n=1:size(vd0,2)
71     tmax=1.1*Ls_des/(vd0(n)+vf*1000); %(sec)
72     tscale=10^(floor(log10(tmax))-3); %(sec)
73     tspan= 0 :tscale: tmax; %define time span for analysis
74     for m=1:size(rd0,1)
75         [t,rd1,Vd1,Td1,vd1,xd1,zr1]=DustPlasmaDynamics2(rd0(m),Vd0,Td0,...
76             vd0(n),zr0,tspan,Te,Ti,ne,ni,mi,vf,Ls,...
77             rhod,cd,delm,Em,W,m0,Lams,n0,T0);
78         %find output value closest to Ls_des
79         [val,idx]=min(abs(abs(real(zr1))-Ls_des));
80         %if more than 0.1% away from Ls_des, assume full ablation
81         if val>(.001*Ls_des)
82             rdf(m,n)=-.5e-06;
83             vdf(m,n)=100;
84         else
85             rdf(m,n)=rd1(idx);
86             vdf(m,n)=vd1(idx);
87         end
88     end
89 end
90
91 %define colormap with max value=white
92 parula2=colormap(parula); parula2(256,:)=1;
93
94 % Define contours for final grain size
95 rmin=0; %min recoverable size (m)
96 rmax=max(rd0)*10^(-6);
97 rcont=rmin:0.5e-06:rmax; %size contours
98 %define contours for final grain velocity
99 vmax=6000; %max allowable final speed (m/s)
100 vcont=0:1000:vmax; %velocity contours
101
102 % Draw specified contour plots and save for overlay
103 fig3= figure(3); %Final Grain Radius plot
104 fig3.Color=[1 1 1]; fig3.Units='centimeters'; fig3.Position=[10 6 11 9];
105 [C1,h1]=contourf(abs(vd0),rd0,real(rdf),rcont); clabel(C1,h1);
106 xlabel('initial relative velocity (m/s)');
107 ylabel('initial grain radius (\mum)');
108 title('Designed Plasma for Collector');
109 F1=getframe(gcf); RGB1=frame2im(F1); %save figure as image
```

```
110
111 fig4= figure(4); colormap(parula2); %Final Velocity plot
112 fig4.Color=[1 1 1]; fig4.Units='centimeters'; fig4.Position=[10 6 11 9];
113 [C2,h2]=contourf(abs(vd0),rd0,-real(vdf),vcont); clabel(C2,h2);
114 xlabel('initial relative velocity (m/s)');
115 ylabel('initial grain radius (\mum)');
116 title('Designed Plasma for Collector');
117 F2=getframe(gcf); RGB2=frame2im(F2); %save figure as image
118
119 % Put overlays on one figure
120 ax=nexttile(tcfig,1);
121 im1=image(RGB1); axis off; hold on;
122 im2=image(RGB2,'AlphaData',0.5);
123 set(ax,'XTick',[], 'YTick', []);
124 hold off
125
126 saveas(cfig,sprintf('ContAnalysis %gx%g.png',size(vd0,2),size(rd0,1)));
127
128
129 %% Energy and Dust Collection Analysis
130
131 % Necessary Constants %
132 kB=1.380649*10^(-23); %Boltzmann constant (J/K)
133  kBeV=1380649/16021766340; %Boltzmann constant (eV/K)
134
135 % Radius of Plasma/Collector (m) %
136 % rp=0.0178; %gives ¬10 cm^2 area
137 rp=sqrt(10/pi)/100; %gives 10 cm^2 area
138
139
140 % Energy Calculations %
141 %energy per unit volume (J/m^3)
142 epsp=.5*mi*np*(vf*1000)^2+2.5*kB*(Tp/kBeV)*np;
143 %energy of the plasma sheet (J)
144 Ep=epsp*pi*rp^2*Ls_des
145
146
147
148 %%% Values Determined From Contour Plot %%%
149 vsc = 4000; %chosen initial velocity (m/s)
150 Drd=(0)*10^(-6); %shift in dust distribution due to ablation (m)
151 rd1star=(.25)*10^(-6); %ablated radius at velocity = 0 (m)
152 rd2star=(1.1)*10^(-6); %ablated radius at velocity = 3 km/s (m)
153
154
155
156 %min values from Porco et. al. 2017
157 q=3; %exponent for dN/dr = (constant)*r^(-q) %q=3 for 50km altitude
158 %min values
159 FWHM=(258)*1000; %Full Width Half Max of plume (flyby distance) (m)
```

```
ndtable=107; %number density from table
rmintable=(0.5)*10^(-6); %min value of rd used to find ndtable (m)
% ndtable=12; %number density from table
% rmintable=(1.5)*10^(-6); %min value of rd used to find ndtable (m)
rmax=(10)*10^(-6); %max rd value of distribution (m)

% Minimum Collection Calculations %
%dN/dr coeff. (m^-1)
Cdist=(ndtable*2)/(1/(rmintable)^(q-1)-1/(rmax)^(q-1));
mcint=@(rd) (4/3)*pi^2.*rd.^3.*rhod*rp^2*FWHM*Cdist.*(rd+Drd).^(-3);
mcmin=integral(mcint,rd1star,rd2star) %collected mass for 1 pass (kg)
%influx rate of particles larger than rmintable (particles/sec)
Rdmin=ndtable*pi*rp^2*vsc



%max values from Porco et. al.
FWHM=(92)*1000; %Full Width Half Max of plume (flyby distance) (m)
ndtable=3540; %number density from table
rmintable=(0.5)*10^(-6); %min value of rd used to find ndtable (m)
% ndtable=385; %number density from table
% rmintable=(1.5)*10^(-6); %min value of rd used to find ndtable (m)
rmax=(10)*10^(-6); %max rd value of distribution (m)

% Maximum Collection Calculations %
%dN/dr coeff. (m^-1)
Cdist=(ndtable*2)/(1/(rmintable)^(q-1)-1/(rmax)^(q-1));
mcint=@(rd) (4/3)*pi^2.*rd.^3.*rhod*rp^2*FWHM*Cdist.*(rd+Drd).^(-3);
mcmax=integral(mcint,rd1star,rd2star) %collected mass for 1 pass (kg)
%influx rate of particles larger than rmintable (particles/sec)
Rdmax=ndtable*pi*rp^2*vsc
```